

Matteo Mazzanti

Trapped Ions in Optical Tweezers and their applications to quantum computing

**TRAPPED IONS IN OPTICAL TWEEZERS
AND THEIR APPLICATIONS TO
QUANTUM COMPUTING**

ACADEMISCH PROEFSCHRIFT

ter verkrijging van de graad van doctor
aan de Universiteit van Amsterdam
op gezag van de Rector Magnificus
prof. dr. ir. P.P.C.C. Verbeek

ten overstaan van een door het College voor Promoties ingestelde commissie,
in het openbaar te verdedigen in de Agnietenkapel
op donderdag 12 oktober 2023, te 10.00 uur

door Matteo Mazzanti
geboren te Ferrara

Promotiecommissie:

Promotor :	dr. R. Gerritsma	Universiteit van Amsterdam
Copromotor :	dr. A. Safavi-Naini	Universiteit van Amsterdam
Overige leden:	prof. dr. J. Home	ETH Zürich
	prof. Dr. F. E. Schreck	Universiteit van Amsterdam
	dr. B. Lanyon	Universität Innsbruck
	prof. Dr. H. M. Buhrman	Universiteit van Amsterdam
	dr. R. J. C. Spreeuw	Universiteit van Amsterdam

Faculteit der Natuurwetenschappen, Wiskunde en Informatica

The work described in this thesis was carried out in the group “Quantum Gases & Quantum Information”, at the Van der Waals-Zeeman Instituut of the University of Amsterdam, Science Park 904, 1098 XH Amsterdam, The Netherlands, where a limited number of copies of this thesis is available. A digital version of this thesis can be obtained from <http://dare.uva.nl>.

The work described in this thesis has been supported by the Netherlands Organisation for Scientific Research (NWO).

To my family

LIST OF PUBLICATIONS

Publications forming the content of this thesis:

1. **M. Mazzanti**, R. Gerritsma, R. Spreeuw & A. Safavi-Naini. *Trapped Ion Quantum Computing using Optical Tweezers and the Magnus Effect*. Phys. Rev. Res., accepted (2023).
2. **M. Mazzanti**, R. X. Schüssler, J. D. Arias Espinoza, Z. Wu, R. Gerritsma & A. Safavi-Naini. *Trapped ion quantum computing using optical tweezers and electric fields*. Phys. Rev. Lett. **127**, 260502 (2021).

Further publications:

3. J. D. Arias Espinoza, **M. Mazzanti**, K. Fouka, R. X. Schüssler, Z. Wu, P. Corboz, R. Gerritsma & A. Safavi-Naini. *Engineering spin-spin interactions with optical tweezers in trapped ions*. Phys. Rev. A **104**, 013302 (2021).
4. J. D. Arias Espinoza, K. Groenland, **M. Mazzanti**, K. Schoutens & R. Gerritsma. *High-fidelity method for a single-step N-bit Toffoli gate in trapped ions*. Phys. Rev. A **103**, 052437 (2021).
5. H. Hirzler, T. Feldker, H. Fürst, N. V. Ewald, E. Trimby, R. S. Lous, J. D. Arias Espinoza, **M. Mazzanti**, J. Joger & R. Gerritsma. *Experimental setup for studying an ultracold mixture of trapped $Yb^+ - ^6Li$* . Phys. Rev. A **102**, 033109 (2020).
6. T. Feldker, H. Fürst, H. Hirzler, N. V. Ewald, **M. Mazzanti**, D. Wiater, M. Tomza & R. Gerritsma. *Buffer gas cooling of a trapped ion to the quantum regime*. Nature Physics **16**, 413 (2020).

My contribution to these publications:

1. I did all the numerical simulations and took the lead in writing and the refereeing process.
2. I did all the numerical simulations and I helped writing the manuscript.
- 3–4. I helped with feedback on the manuscript and discussions.
- 5–6. I helped perform the experiment and in writing the manuscript.

CONTENTS

1	Introduction	1
1.1	Quantum computing and quantum simulations	1
1.2	Trapped ions for quantum computing and simulations	3
1.3	Optical tweezers	5
1.4	Scope of this thesis	6
1.5	Structure of this thesis	7
2	Theoretical background	9
2.1	Paul traps	9
2.1.1	Ideal linear Paul trap	9
2.1.2	Equations of motion	10
2.1.3	Types of micromotion and their implications	11
2.1.4	Two-dimensional crystals	12
2.1.5	Ion crystals	15
2.1.6	Quantum limit	17
2.1.7	Qubit states	17
2.2	Ions-laser interactions	18
2.2.1	Raman interactions	19
2.2.2	Spin-spin interactions	20
2.3	Optical tweezers	22
2.3.1	Stark shift	23
2.3.2	Optical tweezers potential	26
2.4	Engineering of vibrational modes using optical tweezers	27
2.4.1	Tuning spin-spin interactions	30
2.4.2	Optimizing tweezers patterns	32
2.4.3	Example: spin ladder	32
2.4.4	Experimental considerations	33
2.4.5	Spin-dependent optical tweezers	35
3	Electrical field gate with optical tweezers	37
3.1	A novel two-qubit gate	37
3.2	Realizing a geometric phase gate	39
3.2.1	Effective Hamiltonian	40
3.3	Gate fidelity and scalability	41
3.4	Experimental considerations	43
3.5	Conclusions	46
4	Magnus quantum gate	47
4.1	The Magnus effect for engineering a two-qubit gate	47
4.2	Setup	48

4.3	Tweezer Hamiltonian	50
4.3.1	Optical Magnus effect	51
4.4	Characterization of the gate	51
4.4.1	Phase-space dynamics	54
4.5	Clock state case	55
4.6	Conclusions	58
5	Experimental Setup	59
5.1	Ion trap	61
5.1.1	A flatter potential	62
5.1.2	Helical resonator and trap filtering	63
5.2	Gold plating	66
5.2.1	Etching of titanium	66
5.2.2	Gold electroplating	68
5.2.3	Surface analysis	69
5.3	Vacuum system	71
5.3.1	Magnetic field	72
5.4	Laser Systems	73
5.4.1	Laser addressing of ions	74
5.4.2	Photo-ionization laser	75
5.4.3	Detection and cooling laser	77
5.4.4	Raman Laser	78
5.4.5	Repumper lasers	79
5.5	Optical cavity	81
5.5.1	UV cavity	82
5.5.2	IR cavity	83
5.6	Detection System	83
5.7	Spatial Light Modulator	85
6	Setup characterization	87
6.1	Baking of vacuum setup	87
6.1.1	Vacuum characterization	88
6.2	Trap frequencies measurement	89
6.2.1	Axial trapping frequencies	91
6.2.2	Control of the radial confinement	91
6.3	Magnification of the optical system	92
6.4	Micromotion compensation	93
6.5	Spatial Light Modulator	94
6.5.1	Searching for optimal phase patterns	95
6.5.2	SLM efficiency	97
6.5.3	Correction of optical aberrations	98
6.6	Alignment of optical tweezers	101
6.7	Dark ions	102

7 Conclusions and outlook	107
7.1 Future upgrades	108
Summary	111
A Tensor calculus	113
A.1 Tensors operators	113
A.2 Irreducible tensors in second order perturbation theory	115
A.3 \vec{E} tensor representation	116
Bibliography	117

INTRODUCTION

1.1 QUANTUM COMPUTING AND QUANTUM SIMULATIONS

Quantum computing is a rapidly developing field of research that promises to revolutionize the way we solve complex problems. The field was born around 1980 when Richard Feynman first proposed the idea of studying complex quantum systems by simulating them using a more controllable one [1]. At around the same time, Paul Benioff described a first universal quantum computer or quantum Turing machine. In the following years, the first quantum algorithms were proposed, such as Deutsch's algorithm [2] and Simon's algorithm [3] which in turn served as inspiration for Shor's algorithm [4].

The basic principle of a quantum computer is to use the laws of quantum mechanics to perform calculations in a fundamentally different way than classical computers. In classical computers, the basic unit of information is the bit, which can exist in two states, 0 or 1. In quantum computing, instead, a qubit is the fundamental unit of information. It represents a two-level quantum system and can exist in a superposition of states, unlike classical bits. Qubits are mathematically described as a combination of basis states $|0\rangle$ and $|1\rangle$ with complex probability amplitudes. Quantum gates manipulate qubits through unitary transformations, enabling quantum computation

Quantum computers make use of phenomena such as superposition and entanglement to efficiently explore complex multidimensional computational spaces. Problems that are believed to be computationally difficult for classical computers to solve in a *reasonable* time ($\ll 3.14 \times 10^{16}$ s), can be mapped to such spaces where it is possible to exploit the speedup offered by quantum computers. The ability to solve such problems in a feasible amount of time is usually referred as quantum advantage.

Quantum computers can be separated in two main classes, *digital* quantum computers and *analog* quantum computers (or quantum simulators). The first type are analogous to modern computers. With the ability of writing computer code, digital quantum computers can be used to solve any kind of problem that can be translated into an algorithm. On the other hand, analog quantum computers can be compared to physical models that are used to simulate harder but specific problems [5]. For example, early mechanical models of the solar system to predict the motion of celestial bodies or crash tests related

to automobile safety. Digital quantum computers can be programmed to solve the same type of problems that analog quantum simulators are tailored to solve, in the same way as modern computer can be used to simulate systems that are too costly, or impossible, to construct and test (eg. buildings' stability, weather forecast etc.).

During the current era of noisy intermediate-scale quantum (NISQ) systems, the construction of a universal programmable quantum computer capable of solving all open problems in physics remains elusive. Consequently, analog quantum computers have garnered significant attention due to their ability to address specific quantum many-body physics problems, while offering enhanced reliability compared to modern digital quantum computers. State-of-the-art quantum simulators have proven invaluable in examining the extent to which our microscopic models accurately depict the many-body phenomena observed in materials and molecules, providing crucial insights into their behavior [6].

Furthermore, quantum simulations have the potential to revolutionize many other areas of science and technology. For example, they could be used to design new drugs [7], study phase-transitions in materials [8], catalysts [9–11], topological insulators [12, 13] as well as study the behavior of entanglement in quantum systems [14]. Furthermore, quantum simulations might also lead to a more profound understanding of the basic principles of quantum mechanics [15–19].

The development of a practical quantum computer is a major challenge due to the fragility of qubits and the difficulty of implementing error correction. Several physical systems are being investigated as potential platforms for a quantum computer, including superconducting circuits [16, 20, 21], trapped ions [22, 23], Rydberg atoms in optical tweezers [24–27] and quantum dots [28]. Each platform has its own advantages and challenges. Significant progress has been made in recent years in developing scalable architectures and improving the fidelity of quantum operations [29–32].

Overall, the field of quantum computing is a rapidly evolving and exciting area of research with the potential to transform computing and our understanding of the nature of computation. In this thesis, we will explore the use of trapped ions combined with optical tweezers as a platform for quantum computing. We will show how the trapped ion quantum computer can benefit from optical tweezers. Combining the two makes it possible to engineer novel multi-qubits gates that, while achieving state-of-the-art fidelities, might be easier to implement on present experimental setups. This can reduce the experimental complexity that limits modern quantum computers.

1.2 TRAPPED IONS FOR QUANTUM COMPUTING AND SIMULATIONS

The trapped ions system stands out as one of the most promising platforms for realizing quantum information processing. This field, much like quantum computing, traces its roots back to 1953 with the pioneering work of Wolfgang Paul [33, 34], who introduced the radio-frequency trap for ions. The first ions were trapped years later with the device having broad applications in the field of mass spectroscopy. The use of Paul traps for quantum computing began in 1995 when Cirac and Zoller [35] proposed an implementation of a trapped ion quantum computer that would satisfy the DiVincenzo criteria [36].

To perform quantum operations in trapped ions, the first requirement is good isolation from the environment. This is often realized in high-vacuum conditions where ion collisions with background gases are strongly reduced. In vacuum and with the aid of lasers, neutral atoms can be ionized and trapped making use of the combination of static with either oscillating electric fields (Paul trap) or strong magnetic fields (Penning trap) [37].

A schematic representation of a trapped ion quantum computer is depicted in Fig. 1.1. Each ion possesses at least two internal states that encode a two-level system where a qubit can be implemented. At low temperatures, the interplay between the Coulomb repulsion and the trapping confinement make the ions crystallize, usually in one- or two-dimensional configurations. The system can be imagined as N spin-1/2 interacting particles, each interconnected by springs to its neighbors (see Fig. 1.1 a)). Interactions between the particles' spins are mediated by the vibrational modes of the crystal (or phonons) and play a crucial role in the implementation of two-or-more qubit gates or for the realization of spin-1/2 models.

It is worth mentioning that, in this particular context, the term “spin-spin interactions” does not refer to direct interactions between the magnetic spins of the ions. Instead, we typically choose two specific states from the multitude of internal states in the ionic electron shell configuration. These selected states are isolated from the other internal states, allowing the system to effectively behave as a pseudo spin-1/2 system, hence the use of the term “spin” in this context.

An intuitive idea of how spin-spin interactions are realized is shown in Fig. 1.1 a). Using laser beam pulses \vec{k}_1 and \vec{k}_2 , it is possible to generate a state-dependent force F on the ions. This force can either be attractive or repulsive depending on the ion's internal state.

The spin-dependent force induces a small displacement in the ions, effectively changing the relative distance between the target ions and the rest of the ion chain (see Figure 1.1). This change in distance affects the Coulomb interaction experienced by the ions, leading to a state-dependent shift in

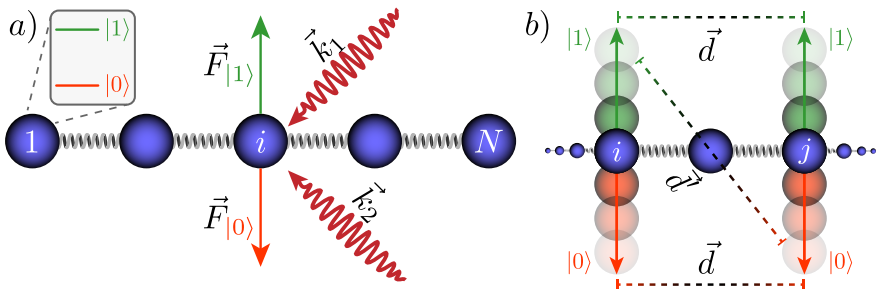


FIGURE 1.1: a) Linear chain of $N = 5$ ions. Each ion possesses two internal states denoted $|0\rangle$ and $|1\rangle$. Using laser beams \vec{k}_1 and \vec{k}_2 , it is possible to generate a force F that depends on the internal state of the ions. b) The ions experience a force in-phase or out-of-phase depending on their internal state. The in-phase force induces a displacement where the relative distance \vec{d} between ions i and j remains unaltered. In the case of out-of-phase displacement, their relative distance changes to \vec{d}' .

their internal energy levels. Figure 1.1 b) depicts the effect of spin-dependent displacement on two ions.

When both the target ions are in the same spin states ($|0,0\rangle$ or $|1,1\rangle$), their relative distance \vec{d} remains unchanged by the force displacement. Conversely, if the ions are in opposite spin states ($|0,1\rangle$ or $|1,0\rangle$), their relative distance becomes \vec{d}' .

The energy difference between the state $|0,0\rangle$ or $|1,1\rangle$ and $|0,1\rangle$ or $|1,0\rangle$ can be utilized to engineer phase gates for two qubits. A phase gate requires one of the two combinations of states to acquire a phase of $\pi/2$. This can be achieved by manipulating the motion of the ions in phase space. By appropriately adjusting the intensity and duration of the laser pulses, the ions can be displaced by approximately the size of the ground-state wavepacket of the ions (typically ~ 5 nm). Since the ions are trapped in a harmonic potential, their motion in phase space follows the dynamics of a harmonic oscillator. After an integer number of oscillations, the ions return to their initial motional state. For repeatability of the quantum gate needed for the execution of quantum algorithms, it is crucial to carefully control the system parameters to ensure that the final motional state closely resembles the initial one.

Because the quantum information is mediated by the crystal's phonons, precise control of the motional modes is required. For this reason modern

laser cooling techniques have to be implemented to efficiently cool the ions near their motional ground state to achieve high fidelity quantum gates.

Upon completion of quantum operations, the states of ion qubits can be measured using a method known as state-dependent fluorescence detection [38]. This measurement process involves projecting the ion qubit into either a bright state $|1\rangle$, which results in the emission of $\sim 10^8$ photons/s upon illumination by a detection laser, or a dark state $|0\rangle$, which scatters minimal photons. A few percent of the scattered photons are collected by an imaging system and detected by a photomultiplier tube (PMT) or a charge-coupled device (CCD).

Trapped ions have shown great potential in the field of quantum information processing due to their fully connected interactions and reliable quantum gates. They offer the possibility of developing scalable and dependable quantum processors. Therefore, further research into trapped ion systems is crucial for the realization of large-scale quantum information processing and the development of new technologies.

1.3 OPTICAL TWEEZERS

Optical tweezers were first introduced by Arthur Ashkin in the 1970s, pioneering a new era in manipulating and studying microscopic particles using focused laser beams [39]. The technique was based on the concept of gradient forces, where particles experience a net force towards the region of highest light intensity.

In neutral atom systems, optical tweezers have been widely used to investigate atom-atom interactions and collective behavior. Precise control over ultracold atoms systems can help in exploring fundamental aspects of quantum mechanics, such as entanglement and quantum correlations, in controlled environments [40]. Optical tweezers enable the creation of tailored trapping geometries and manipulation of atomic motion with high accuracy, leading to advancements in the study of quantum gases, including Bose-Einstein condensates and degenerate Fermi gases. This has facilitated investigations of phenomena such as quantum phase transitions, superfluidity, and quantum magnetism [41].

Moreover, the combination of optical tweezers and ultracold atoms holds significant promise for quantum computing applications. Optical tweezers offer precise manipulation and control of individual atoms allowing a scalable, modular and tunable platform. More specifically, optical tweezers can be used to generate various neutral atom configurations allowing precise control over the connectivity of the system [24, 25, 42–44]. Finally, they enable rearrangements of the atoms during normal operations. For example, It is in

fact possible to shuttle the atoms between computational, storage and error correction zones.

For all these reasons, optical tweezers have emerged as an invaluable tool for manipulating ultracold atoms, molecules, and microscopic particles with exceptional precision. This technological advancement has paved the way for precise investigations into the behavior of systems driven by quantum mechanical effects. Furthermore, the application of optical tweezers in the realm of ultracold atoms have already showcased significant advantages for quantum computing and simulations. Optical tweezers provide a versatile platform for constructing quantum registers and implementing quantum gates, thereby positioning themselves as a valuable asset in the quest for practical quantum computing technologies.

1.4 SCOPE OF THIS THESIS

This thesis focuses on the construction of a novel experimental apparatus designed for the creation and manipulation of two-dimensional ion crystals. Our objective is to alter the spectrum of sound-waves in the crystal by employing optical tweezers generated through a Spatial Light Modulator (SLM). This will allow us to control the strength of the interactions between the ions, with applications to quantum simulations.

Furthermore, we will investigate the integration of trapped ions and state-dependent optical tweezers, exploring their applications in quantum logic gates for quantum computing.

In this thesis we aim to answer the following questions:

- Can we use optical tweezers to program the spin-spin interactions between ions?

Trapped ion quantum simulators possess a distinct advantage over other systems due to their fully connected interactions, making them well-suited for simulating quantum systems in one and two dimensions. However, the ability to manipulate the range of interactions presents an opportunity to explore a broader range of theoretical models. By incorporating optical tweezers, it may be feasible to enhance the capabilities of existing trapped ion quantum simulators [45]. This expansion opens up possibilities for investigating the relationship between interaction ranges and the dynamics of quantum information [18, 46, 47]

- Can we use optical tweezers as an architecture for quantum computing?

The combination of trapped ions with optical tweezers can offer benefits beyond quantum simulations. Specifically, the use of state-dependent tweezers

can lead to innovative designs for achieving two-qubit quantum entangling gates. Optical tweezers have the ability to alter the phonon spectra of an ion crystal in a spin-dependent manner. As the phonons are the carrier of quantum information in trapped ions this effect can be used to control the flow of quantum information between two (or more) ions.

- Can we create a setup in which we can trap and manipulate 2-dimensional ion crystals?

Most of the current experimental setups use linear chains of trapped ions. We believe that much can be gained by moving to a two-dimensional geometry. As most of the models of interest in solid state physics are two-dimensional [48–50], two-dimensional structures would offer a natural platform for implementing quantum simulations of such systems. However, this leads to novel experimental challenges and considerations. As the radio-frequency null zone of a usual linear Paul trap lays on a line we will have to take in account the effects generated by electric fields on the ions laying at the borders of the two-dimensional crystal.

- Can we modify the soundwave spectrum of trapped ions using tweezers?

Optical tweezers can be used to generate local trapping or anti-trapping potentials depending on the chosen laser detuning. This leads to an interplay between the global trapping potential generated by the radio-frequency Paul trap and the strength of the site-dependent tweezers potential. Due to the fact that the interaction between ions is mediated by the global modes of oscillation, although the perturbations generated by the tweezers are local, their effect can have implications on the whole system [45, 51].

1.5 STRUCTURE OF THIS THESIS

This thesis is structured as follows:

Chapter 2 provides the theoretical foundations for ion trapping. It starts with an introduction to the linear Paul trap, followed by a discussion of the modifications required for generating two-dimensional crystals in a plane. The chapter includes an overview of ion-laser interactions and how spin-spin interactions can be created in trapped ions. It also covers the effects of optical tweezers on trapped ions and how they can be used to modify spin-spin interactions.

Chapter 3 presents a novel theoretical proposal to engineer two-qubit gates in trapped ions using a combination of optical tweezers and oscillating electric fields. This chapter focuses on the experimental advantages and

challenges of this approach and demonstrates how it can achieve state-of-the-art fidelities while achieving scalability to large ion crystals. We find that this design does not rely on ground state cooling of the ions or the Lamb-Dicke approximation. We perform numerical simulations in order to estimate the maximum achievable fidelities at various tweezers strength. We furthermore study the effects of laser intensity noise, finding that particular attention is needed in order to intensity stabilize optical tweezers to $\sim 1\%$ level.

Chapter 4 introduces a second theoretical method for achieving a two-qubit gate using the optical Magnus effect [52], which arises in tightly focused optical beams. This approach off-resonantly drives the phase-space motion of two ions to engineer a two-qubit gate. The use of optical tweezers in this method simplifies the experimental complexity while maintaining high fidelity.

To assess the robustness of the gate, we conduct numerical simulations for various thermal states, demonstrating that the gate fidelity is insensitive to thermal occupation of motional modes. We also perform an error budget analysis to identify the limiting factors on the achievable gate fidelity. Our results show that off-resonant scattering and misalignment of the tweezers are the two most significant factors. While scattering rates can be reduced by selecting a higher laser detuning, this comes at the cost of increased laser power. Tweezers misalignment of less than 30 nm requires particular attention in the lab, although single tweezer alignment has been experimentally demonstrated with nm precision [53].

Chapter 5 describes the experimental setup used to generate two-dimensional crystals of trapped ions. The chapter includes a detailed description of the ion trap design and construction, the vacuum setup used for ion trapping, the various laser systems and the optical tweezers setup.

Chapter 6 focuses on a comprehensive characterization of the experimental setup. It includes the utilization of the number of hops between ions in a linear crystal as a metric for assessing vacuum quality. Furthermore, the axial and radial trapping frequencies of our Paul trap are thoroughly examined and reported. The chapter also considers the characterization of the optical setup utilized for ion detection. It briefly outlines the implementation and functionality of Spatial Light Modulators (SLM) and provides an overview of various SLM characterization methods employed in the experiment. Notably, the chapter demonstrates how the SLM can effectively rectify optical aberrations within the optical tweezers setup. Lastly, the chapter showcases the results obtained from the initial alignment of an optical tweezer to a single ion, marking a significant milestone in the experimental progress.

THEORETICAL BACKGROUND

This chapter equips the reader with the knowledge necessary to understand the concepts that will be discussed later on. We commence by introducing linear Paul traps and show that with small modifications to the conventional design, we can assemble the ions into two-dimensional crystals. We then describe how interactions between the internal (spin) states of the ions can be engineered using lasers. Finally, we show how optical tweezers can be used to tune the interactions between the ions. This enables us to create a programmable quantum simulator that can be reconfigured and adapted to simulate various quantum systems.

2.1 PAUL TRAPS

One of the most common methods for confining ions is to use a radio-frequency trap, also known as a Paul trap. Although there are many variations of this device's design [54], a linear Paul trap consists of two pairs of radio-frequency electrodes that provide confinement in the radial directions (r_x , r_y). Additionally, a third pair of electrodes supplies a static electric field to provide confinement in the axial (r_z) direction.

2.1.1 *Ideal linear Paul trap*

In a general case the potential generated by a Paul trap can be written as follows:

$$V_{\text{PT}}(\mathbf{r}, t) = \sum_{j,i=x,yz} \frac{U^{\text{DC}}}{2} \alpha_{j,i}^{\text{DC}} r_j r_i + \sum_{j,i=x,yz} \frac{U^{\text{RF}}}{2} \alpha_{j,i}^{\text{RF}} \cos(\Omega_{\text{RF}} t) r_j r_i \quad (2.1)$$

where $U^{\text{DC/RF}}$ are the voltages applied to the DC/RF electrodes, $\alpha_{j,i}^{\text{DC/RF}}$ are matrices containing the geometrical factors for the DC/RF field curvature and Ω_{RF} is the trap driving frequency. For conventional linear Paul traps, the matrices $\alpha_{j,i}^{\text{DC}}$ and $\alpha_{j,i}^{\text{RF}}$ take the form of diagonal and traceless matrices with $\alpha_{z,z}^{\text{DC}} = -1/2\alpha_{x,x/y,y}^{\text{DC}}$ and $\alpha_{x,x}^{\text{RF}} = -\alpha_{y,y}^{\text{RF}}$, $\alpha_{z,z}^{\text{RF}} \sim 0$. The traceless condition is enforced by Maxwell equations imposing $\Delta V_{\text{PT}} = 0$.

2.1.2 Equations of motion

We start by describing the motion of an ion in a linear Paul trap where the matrices $\alpha_{j,i}^{\text{DC}}$ and $\alpha_{j,i}^{\text{RF}}$ are diagonal.

The equations of motion for a singly charged ion can be derived from the potential at ion's location. Ions are usually trapped at the so-called radio-frequency null zone where the effects of the oscillatory potential are minimized. The force induced by the potential V_{PT} is expressed as $F(\mathbf{r}, t) = eE(\mathbf{r}, t)$ where e is the unit of electric charge, assuming singly charged ions, and $E(\mathbf{r}, t)$ is the electric field at the center of the Paul trap given by $E(\mathbf{r}, t) = -\nabla V_{\text{PT}}(\mathbf{r}, t)$. Using the geometrical factors of a ideal linear Paul trap, we obtain:

$$\begin{aligned} E(\mathbf{r}, t) = & -U^{\text{DC}} \left(-\frac{1}{2}\alpha_{z,z}^{\text{DC}}\mathbf{x} - \frac{1}{2}\alpha_{z,z}^{\text{DC}}\mathbf{y} + \alpha_{z,z}^{\text{DC}}\mathbf{z} \right) \\ & - U^{\text{RF}} \cos(\Omega_{\text{RFT}}t) (\alpha_{x,x}^{\text{RF}}\mathbf{x} - \alpha_{x,x}^{\text{RF}}\mathbf{y}), \end{aligned} \quad (2.2)$$

with $\mathbf{x} = r_x\hat{\mathbf{x}}$, $\mathbf{y} = r_y\hat{\mathbf{y}}$, $\mathbf{z} = r_z\hat{\mathbf{z}}$ and $\hat{\mathbf{x}}, \hat{\mathbf{y}}, \hat{\mathbf{z}}$ the three orthogonal unit vectors. From this it is possible to obtain the equations of motion, also known as the *Mathieu differential equations* [55]:

$$\ddot{r}_j = - (a_j^{\text{DC}} - 2q_j^{\text{RF}} \cos(\Omega_{\text{RFT}}t)) \frac{\Omega_{\text{RFT}}^2}{4} r_j, \quad (2.3)$$

with the a_j and q_j the dimensionless trapping parameters:

$$a_z = \frac{4eU^{\text{DC}}\alpha_{z,z}^{\text{DC}}}{m\Omega_{\text{RFT}}^2} = -2a_{x,y}, \quad (2.4)$$

$$q_x = \frac{2eU^{\text{RF}}\alpha_{x,x}^{\text{RF}}}{m\Omega_{\text{RFT}}^2} = -q_y, \quad q_z = 0. \quad (2.5)$$

The stability of ions in a trap is determined by the values of the a_z and q_x parameters, which define the stability conditions. A combination of these parameters that results in a stable configuration is commonly known as a stability diagram. We will not report here the exact solutions for the Mathieu equations. Instead, it was shown [56] that for values of $q_j \ll 1$ and $a_j \ll q_j$ one can expand to a lowest-order approximation and express the ion's motion in a simple form:

$$r_j(t) \approx A_j \cos(\omega_j t + \phi_j) \left(1 + \frac{q_j}{2} \cos(\Omega_{\text{RFT}}t) \right), \quad (2.6)$$

where A_j is the amplitude of motion of the ion, ϕ_j a relative phase and

$$\omega_j \approx \frac{\Omega_{\text{RF}}}{2} \sqrt{a_j + \frac{q_j^2}{2}}. \quad (2.7)$$

The resulting solution consists of two oscillatory terms. The first term, with a frequency of ω_j , is commonly referred to as the *secular motion* or macromotion, which is a slow motion. This motion is modulated by a fast oscillatory term, known as *micromotion* (MM), at the trap drive frequency Ω_{RF} and amplitude $A_j q_j / 2$. This micromotion term is *intrinsic* (iMM) of any ideal Paul trap. For the z direction $q_z \sim 0$ as iMM in this direction is absent. This is due to the fact that confinement along the z -axis is provided by a static potential alone. It is worth noting that the amplitude of the iMM term is proportional to q_j . Therefore, if the trap is operated in a stability region where q_j is small, this term will become less significant.

2.1.3 Types of micromotion and their implications

So far we have described the case of ideal Paul traps. However, imperfections from experimental realizations of an ideal Paul trap give rise to additional types of micromotion usually referred to as *excess* micromotion (eMM). One potential cause of eMM is stray electric fields that displace the ion from the radio-frequency null zone. These stray fields can be generated by electrodes' surface imperfections, residual charges or radio-frequency pick-up. In linear Paul traps, this displacement can be compensated for all ions in the chain by controlling extra DC electrodes. However, in the case of 2-dimensional crystals, eMM can not be compensated for all ions simultaneously due to a necessary radial offset in some of their equilibrium positions. Ions positioned at an offset A_{off} from the radial center of the trap will experience eMM with an amplitude of $\sim A_{\text{off}} q_j / 2$.

Other types of eMM include phase MM caused by phase shifts between the radio-frequency potential or axial radio-frequency pickup [55]. The first type can be minimized during the trap design and assembly phase by controlling the impedance of the radio-frequency electrodes and the connections to them (see for example Sec. 5.1). The second type is usually caused by the small spacing (usually $\sim \text{mm}$) between the radiofrequency electrodes and the radial DC ones. This can lead to a non-zero q_z parameter. In this case the ion's motion in the axial direction will contain a micromotion term as from Eq. (2.6). This effect can be minimized by placing the ions in the symmetric center of the two endcap electrodes [55].

In the context of analog quantum simulations using trapped ions and optical tweezers, eMM has two primary effects. First, it modulates the ions' spin-

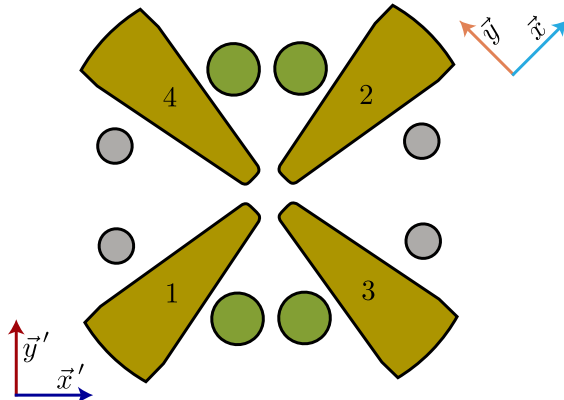


FIGURE 2.1: Section view of the trap used in the experiment. In gold are the two pairs (1-2 and 3-4) of radio frequency electrodes. The electrodes in gray are used for compensating stray fields in the x' -direction. The HV electrodes used for controlling the dimensionality of the crystal are depicted in green. These can as well be used for stray field compensation in the y' -direction.

spin coupling by inducing a Doppler shift. Second, it shifts the anticipated motional modes of an ion crystal [57–59]. Both effects can be taken into account and corrected for by proper parameter optimization and experimental design [57].

2.1.4 Two-dimensional crystals

In the field of quantum simulation it might be interesting to deviate from the usual linear configuration of ion crystals in favor of two-dimensional ones. Two-dimensional crystals allow for better scalability of the system and offer a more natural platform for studying two-dimensional spin-spin Hamiltonians.

The trap built for the experiment described in this thesis is equipped with four pairs of additional DC electrodes. Two pairs are used for eMM compensation on the radial x' direction [55] as shown in Fig. 2.1. The remaining two pairs are used to deviate from the typical potential shape encountered in linear Paul traps.

These pairs of electrodes can be seen in green in Fig. 2.1. We will refer to them as *HV electrodes*. By providing them with a high-voltage electric potential it is possible to lower the trapping frequency on the y -axis while increasing it on the x -axis. When properly tuning these variations in trapping

frequency, the ions can rearrange from a one-dimensional configuration to a two-dimensional one. The HV electrodes can modify the shape of the potential and compete with the strength of the radio-frequency potential. It is therefore useful to redefine the reference system from x - y at low voltage (usual one-dimensional configuration) to x' - y' (two-dimensional configuration) as shown in Fig. 2.1.

We give an expression for the electric field in the new coordinates starting from Eq. (2.2). To do, so we rotate our reference system from (\vec{x}, \vec{y}) to (\vec{x}', \vec{y}') . In this new basis we can write $[x', y']^\top = \mathcal{R}[\pi/4][x, y]^\top$ where $\mathcal{R}[\pi/4]$ is a counterclockwise rotation matrix. We know that the field generated by the endcaps has a uniform curvature on the x, y plane. For this reason, in the new basis $\alpha_{x'}^{\text{DC}} = \alpha_x^{\text{DC}}$ and $\alpha_{y'}^{\text{DC}} = \alpha_y^{\text{DC}}$, and the $\alpha_{j,i}^{\text{DC}}$ and $\alpha_{j,i}^{\text{RF}}$ defined in Eq. (2.1) is:

$$\alpha_{j,i}^{\text{RF}} = \begin{bmatrix} 0 & \alpha_x^{\text{RF}} & 0 \\ \alpha_x^{\text{RF}} & 0 & 0 \\ 0 & 0 & 0 \end{bmatrix}, \quad \alpha_{j,i}^{\text{DC}} = \begin{bmatrix} \frac{-\alpha_z^{\text{DC}}}{2} & 0 & 0 \\ 0 & \frac{-\alpha_z^{\text{DC}}}{2} & 0 \\ 0 & 0 & \alpha_z^{\text{DC}} \end{bmatrix}. \quad (2.8)$$

As the DC potential generated by the HV electrodes can be controlled independently from the one generated by the endcaps this requires the introduction of an additional term to Eq. (2.1):

$$V_{\text{exp}}(\mathbf{r}, t) = V_{\text{PT}}(\mathbf{r}, t) + \sum_{j,i=x,yz} \frac{U_j^{\text{HV}}}{2} \alpha_{j,i}^{\text{HV}} r_j r_i, \quad (2.9)$$

where we defined:

$$\alpha_{j,i}^{\text{DC}} = \begin{bmatrix} \alpha_{x'}^{\text{HV}} & 0 & 0 \\ 0 & \alpha_{y'}^{\text{HV}} & 0 \\ 0 & 0 & 0 \end{bmatrix}. \quad (2.10)$$

From the geometrical reasons $\alpha_z^{\text{HV}} \approx 0$ as the potential induced by the HV electrodes has negligible effects on the z direction. The traceless condition finally imposes that $\alpha_x^{\text{HV}} = -\alpha_y^{\text{HV}} = \alpha^{\text{HV}}$.

The electric field generated by the trap in the new reference system is:

$$\begin{aligned} E(\mathbf{r}, t) = & -U^{\text{DC}} \left(-\frac{1}{2} \alpha_z^{\text{DC}} \mathbf{x}' - \frac{1}{2} \alpha_z^{\text{DC}} \mathbf{y}' + \alpha_z^{\text{DC}} \mathbf{z} \right) \\ & - U^{\text{RF}} \cos(\Omega_{\text{RFT}} t) (\alpha_x^{\text{RF}} r_y \hat{\mathbf{x}}' - \alpha_x^{\text{RF}} r_x \hat{\mathbf{y}}') \\ & - U^{\text{HV}} (\alpha^{\text{HV}} \mathbf{x}' - \alpha^{\text{HV}} \mathbf{y}'), \end{aligned} \quad (2.11)$$

where $\mathbf{x}' = r_{x'} \hat{\mathbf{x}}'$, $\mathbf{y}' = r_{y'} \hat{\mathbf{y}}'$ with $\hat{\mathbf{x}}'$ and $\hat{\mathbf{y}}'$ the unit vector in the new basis.

As $\alpha_z^{\text{HV}} \approx 0$ we can treat the motion only in the radial direction assuming the dynamics in the z direction are well described by the solutions given in section 2.1.2. In terms of the a and q parameters the equations of motion in the radial direction can be written as:

$$\begin{bmatrix} \dot{r}_{x'} \\ \dot{r}_{y'} \end{bmatrix} = \Theta(t) \frac{\Omega_{\text{RF}}^2}{4} \begin{bmatrix} r_{x'} \\ r_{y'} \end{bmatrix}, \quad (2.12)$$

with:

$$\Theta(t) = \begin{bmatrix} a_z - a_{\text{HV}} & -2q_x \cos(\Omega_{\text{RF}}t) \\ -2q_x \cos(\Omega_{\text{RF}}t) & a_z + a_{\text{HV}} \end{bmatrix}. \quad (2.13)$$

Here we defined the new parameter a_{HV} :

$$a_{\text{HV}} = \frac{4eU^{\text{HV}}\alpha_x^{\text{HV}}}{m\Omega_{\text{RF}}^2}. \quad (2.14)$$

Diagonalizing the matrix $\Theta(t)$ leads to a system of uncoupled differential equations. The dynamics of the system can be obtained using a Floquet-Lyapunov approach [59].

Alternatively, a solution can be obtained using the pseudo-potential approximation. In this approximation, the potential generated by the radio-frequency electrodes is assumed to have rotational symmetry that is broken by the electrodes potential in the x' and y' directions. This yields an effective secular trapping frequency in the two new directions given by:

$$\omega_{x'} = \frac{\Omega_{\text{RF}}}{2} \sqrt{\frac{a_z}{2} - a_{\text{HV}} + \frac{q_x^2}{2}}, \quad (2.15)$$

$$\omega_{y'} = \frac{\Omega_{\text{RF}}}{2} \sqrt{\frac{a_z}{2} + a_{\text{HV}} + \frac{q_x^2}{2}}. \quad (2.16)$$

Starting from a 1-dimensional crystal configuration it is possible to control the split between the radial x and y frequencies by varying a_{HV} . By properly tuning this parameter the crystal shape can vary from a 1-dimensional arrangement a 2-dimensional one. However, as the crystal transforms to 2D, bifurcation points are crossed. For example, at the transition between a linear crystal to a “zig-zag” or “zag-zig” configuration. There, one of the collective vibrational frequencies of an ion crystal becomes DC and significant heating can occur. Later in this thesis we will describe in more detail these collective vibrational modes of an ion crystal and show how optical tweezers can be used to modify them in order to avoid bifurcation points. When $\omega_{y'} \approx \omega_z < \omega_{x'}$ the ion crystal will arrange in a full 2-dimensional configuration on the z - y plane.

2.1.5 Ion crystals

So far we have considered the dynamic of one ion in a Paul trap. To consider the dynamics of many ions in a Paul trap we have to take into account the mutual Coulomb interactions. That is, the motion of each ion will be coupled to the motion of all the other ions.

We start by writing the potential generated by the trap on each ion $j = 1 \dots N$, with N being the number of ions present in the trap:

$$V_{\text{trap}} = \sum_{j=1}^N V_{\text{PT}}(\mathbf{r}_i, t), \quad (2.17)$$

where we used Eq.(2.1) and defined the i -ion position as \mathbf{r}_i . Due to their charge, each ion experiences a Coulomb interaction generated by all the other ions present in the trap. We can write the total Coulomb potential as:

$$V_{\text{Coulomb}} = \frac{1}{2} \frac{e^2}{4\pi\epsilon_0} \sum_{\substack{j,i=1 \\ i \neq j}}^N \frac{1}{|\mathbf{r}_j - \mathbf{r}_i|}. \quad (2.18)$$

The total potential experienced by the ions V_{tot} can be expressed as the sum of two components, namely the trapping potential V_{trap} and the Coulomb potential V_{Coulomb} . At low temperatures, the ions tend to remain close to their respective equilibrium positions. The equilibrium position is the point where the forces acting on the ion vanish:

$$\left. \frac{\partial V_{\text{tot}}}{\partial \mathbf{r}_j} \right|_{\mathbf{r}_j=\mathbf{r}_j^0} = 0. \quad (2.19)$$

We can approximate the position of an ion j as $\mathbf{r}_j \approx \mathbf{r}_j^0 + \boldsymbol{\varepsilon}_j$, where \mathbf{r}_j^0 is the equilibrium position of the ion and $\boldsymbol{\varepsilon}_j$ is a small displacement. Using this approximation, we expand the total potential as:

$$V \approx V_0 + \sum_{j=1}^N \boldsymbol{\varepsilon}_j \left. \frac{\partial V_{\text{tot}}}{\partial \mathbf{r}_j} \right|_{\mathbf{r}_j=\mathbf{r}_j^0} + \frac{1}{2} \sum_{j,i=1}^N \boldsymbol{\varepsilon}_j \boldsymbol{\varepsilon}_i \left. \frac{\partial V_{\text{tot}}}{\partial \mathbf{r}_j \partial \mathbf{r}_i} \right|_{\substack{\mathbf{r}_j=\mathbf{r}_j^0 \\ \mathbf{r}_i=\mathbf{r}_i^0}}. \quad (2.20)$$

Ignoring the null terms and the global offset V_0 of Eq. (2.20) yields an expression for the Lagrangian of the system as:

$$\mathcal{L} = \frac{M}{2} \sum_{j=1}^N \dot{\boldsymbol{\varepsilon}}_j^2 - \frac{M}{2} \mathcal{W} \sum_{j,i=1}^N \boldsymbol{\varepsilon}_j \boldsymbol{\varepsilon}_i \mathcal{A}_{i,j}, \quad (2.21)$$

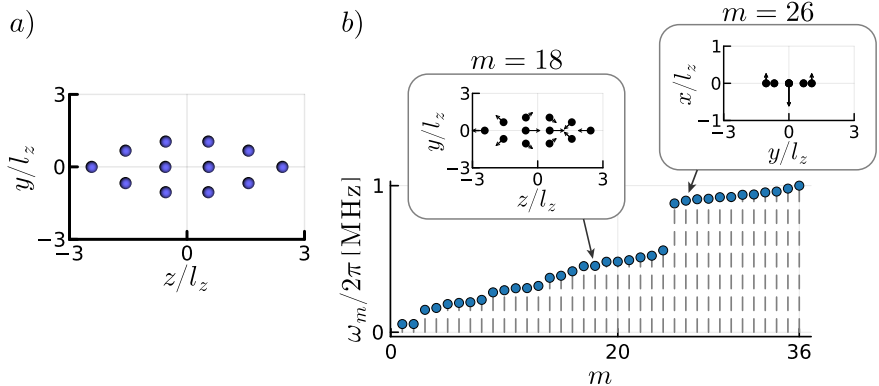


FIGURE 2.2: a) Two-dimensional crystal of $^{171}\text{Yb}^+$ with trapping frequencies $\omega_x = 2\pi \cdot 1 \text{ MHz}$, $\omega_y = 2\pi \cdot 0.3 \text{ MHz}$ and $\omega_z = 2\pi \cdot 0.2 \text{ MHz}$ where the axes have been re-scaled by l_z . b) Eigenfrequencies of vibration of the same ion crystal as a). The inset shows the eigenmodes $m = 18$ (scaled by a factor of 2 for visibility) and $m = 26$. Notice that due to the chosen trapping frequency there is a clear distinction between the in-plane $m < 25$ and out-of-plane ≥ 25 eigenfrequencies.

where we defined $\mathcal{W} = \omega_z \mathbb{1}_N$ and:

$$\mathcal{A}_{i,j} = \left. \frac{\partial V_{\text{tot}}}{\partial \mathbf{r}_j \partial \mathbf{r}_i} \right|_{\substack{\mathbf{r}_j = \mathbf{r}_j^0 \\ \mathbf{r}_i = \mathbf{r}_i^0}} \quad (2.22)$$

is the Hessian matrix calculated at the equilibrium points. It is useful to express the ions' equilibrium position in terms of the normalized inter-ion distance $l_k = (e^2 / (4\pi\epsilon_0 m\omega_k^3))^{1/3}$, with $k = x, y, z$ such that the Hessian matrix is dimensionless. Since the matrix is real, symmetric and non-negative definite its eigenvalues are also non-negative. The eigenvectors \mathbf{b}_m of the N -dimensional matrix and their corresponding dimensionless eigenvalues $\bar{\omega}_m^2$ can be found through exact diagonalization. The original eigenfrequencies frequencies are $\omega_m = \mathcal{W}\bar{\omega}_m$.

In this new basis, any possible motion of the ion crystal can be described as a linear combination of $3N$ uncoupled harmonic oscillators. In Fig. 2.2 a) a 12 ion two-dimensional crystal and its associated eigenmodes and eigenfrequencies are shown.

The accuracy of the eigenmodes and eigenfrequencies of two-dimensional crystals under the pseudo-potential approximation has been extensively studied [58]. The pseudo-potential approximation can predict the equilibrium

position of various ions and the structural phase transitions between crystal configurations. However it fails to precisely determine the eigenfrequencies of the crystal. For a more accurate result the full time-dependent potential has to be considered. This effectively shows that the effect of micromotion is to introduce a shift in the eigenmodes.

2.1.6 *Quantum limit*

When the ion crystal temperature is lowered to $\approx 100\mu K$ the ions' motion should be treated using quantum mechanics. At these levels the quantization of the vibrational energy levels starts playing an important role. As seen in the previous section, under the secular approximation we can approximate the system as m independent harmonic oscillators. Its Hamiltonian can then be written as:

$$\mathcal{H}_{\text{HO}} = \sum_m \hbar\omega_m \left(\hat{a}_m^\dagger \hat{a}_m + \frac{1}{2} \right), \quad (2.23)$$

where $m = 1 \dots 3N$.

2.1.7 *Qubit states*

Trapped ions have emerged as a promising candidate for qubits in quantum computation and simulations, with the selection of suitable ion species dependent on their atomic structure and transition wavelengths.

Despite the various internal states of atomic species, originating from their complex electron structure, the majority of these states can typically be disregarded, allowing for simplification of the system into a two-level system consisting solely of the $|\uparrow\rangle$ and $|\downarrow\rangle$ states with an energy separation of ω_0 . The Hamiltonian for these qubit states in a crystal with N ions can be expressed as:

$$\mathcal{H}_0 = \sum_j^N \hbar \frac{\omega_0}{2} \hat{\sigma}_z. \quad (2.24)$$

Depending on the type of transition between the two states, we can distinguish between *microwave qubits* and *optical qubits*. In the former, the computational basis is selected from two hyperfine substates of the ground state. The splitting between the two states is usually on the order of a few GHz and is frequently chosen from magnetic insensitive states ($m_F = 0$). The energy splitting is typically in the optical range (≈ 400 THz)

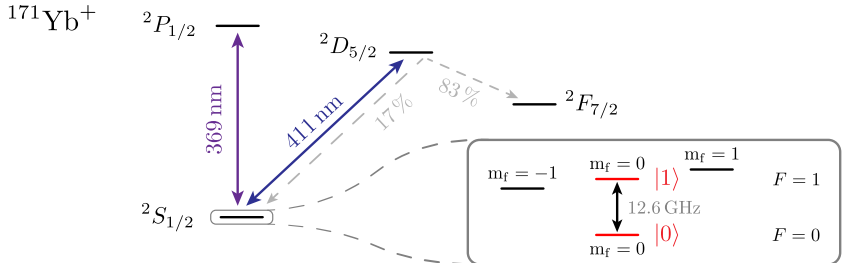


FIGURE 2.3: $^{171}\text{Yb}^+$ Relevant energy levels. The inset shows in red the two hyperfine states used as the computational basis for quantum operations.

In the latter case, the states are encoded between the ground state (S) of the ions and one of the metastable excited electronic state, usually one of the D/F substates.

In our setup we primarily use $^{171}\text{Yb}^+$ as a qubit (sketched in Fig. 2.3 are the relevant energy levels). We encode the qubits states in the $^2S_{1/2}, F = 1, m_F = 0 (|\uparrow\rangle)$ and $^2S_{1/2}, F = 0, m_F = 0 (|\downarrow\rangle)$ states. These two states are magnetic insensitive up to second order and long coherence times have been demonstrated [60]. Thanks to the energy splitting of the two states being ~ 12.6 GHz, single qubits rotations can be driven using microwave fields. Furthermore, coherent control of the two qubit states is preferred as microwave sources are more manageable than optical frequencies.

In addition to its hyperfine ground state structure, $^{171}\text{Yb}^+$ has two long-lived metastable states $^2D_{5/2}$ ($\tau \sim 7.2$ ms) and $^2F_{7/2}$ ($\tau \sim 5.4$ yr) that can be used as an effective second optical qubit. This can enable the implementation of novel types of architectures, as for example *omg* qubits [61]. In this way it would be possible to encode the quantum information using long-lived metastable states as an effective second ion species. Combining metastable states and hyperfine ground states can provide an improvement to state initialization, quantum gates and readout operations.

2.2 IONS-LASER INTERACTIONS

The interaction between laser fields and the internal states of a trapped ion is a necessary building block for quantum computation and quantum simulations. This applies not only to species relying on optical qubits. In fact, the complicated internal energy structure of each species requires the usage of lasers for state initialization, readout and cooling of the ions. We can give

an expression for the interaction Hamiltonian when approximating each ion as a two-level system as:

$$\mathcal{H}_I = \sum_{j=1}^N \hbar \Omega_j \left(e^{-i(\mathbf{k} \cdot \mathbf{r}_j - \omega t)} \hat{\sigma}_-^j + e^{i(\mathbf{k} \cdot \mathbf{r}_j - \omega t)} \hat{\sigma}_+^j \right), \quad (2.25)$$

where Ω_j is the Rabi frequency for the j -th ion, \mathbf{k} is the laser wavevector, ω the laser frequency and $\hat{\sigma}_{+/-}$ the raising/lowering operators. In Eq. (2.25) we ignored the fast rotating terms under the rotating wave approximation and the laser field phase.

2.2.1 Raman interactions

In addition to their role in controlling the internal states of trapped ions, lasers can also be used in a Raman configuration to off-resonantly excite phonon modes in order to engineer multi-qubit quantum gates.

We can describe such a scheme as a Λ -system setup where the detuning from the excited state is large enough to reduce off-resonant scattering rates to $< 1 \text{ s}^{-1}$. To achieve higher coupling, the transition between the qubit states and the excited states is usually chosen to be a dipole allowed transition. A schematic representation of such a scheme can be seen in Fig. 2.4.

The Hamiltonian of a Λ system can be written as:

$$\mathcal{H}_{\text{Raman}} = \begin{bmatrix} 0 & 0 & \Omega_{\downarrow \rightarrow P} \\ 0 & \omega_0 & \Omega_{\uparrow \rightarrow P} \\ \Omega_{P \rightarrow \downarrow}^* & \Omega_{P \rightarrow \uparrow}^* & \Delta \end{bmatrix}, \quad (2.26)$$

in the basis $|\downarrow\rangle, |\uparrow\rangle, |P\rangle$ that compose the Λ -system. Here Δ is the laser detuning from the excited $|P\rangle$ state and $\Omega_{\downarrow \rightarrow P}$ and $\Omega_{\uparrow \rightarrow P}$ are the Rabi frequencies for the $\downarrow \rightarrow P$ and $\uparrow \rightarrow P$ transitions. If the detuning Δ is chosen to be large compared to the line-width of the upper P state it is possible to treat the system as an effective two level system with an effective Rabi frequency of:

$$\Omega_{\text{eff}} = \frac{\Omega_{\uparrow \rightarrow P}^* \Omega_{\downarrow \rightarrow P}}{\Delta}. \quad (2.27)$$

Furthermore, when using Raman beams it is important to consider the impact of photon scattering, which can lead to losses of the quantum information stored in the internal states of the ions. This limits the achievable

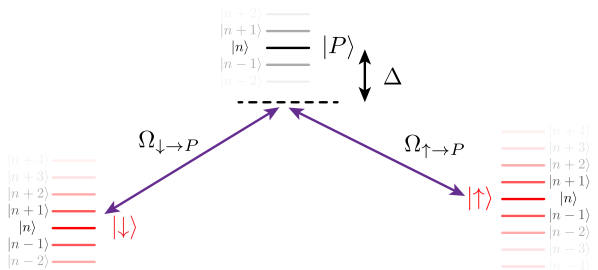


FIGURE 2.4: Schematic representation of a Λ -system (not to scale). The two lasers couple the $|\downarrow\rangle$ and $|\uparrow\rangle$ states through an excite $|P\rangle$ state. Notice the presence of the various vibrational state $|n\rangle$ being the ion in an harmonic potential.

gate fidelity in quantum computing applications and washes out spin-spin coherence effects, which in turn limits the time resolution of quantum simulations. For a detuning $\Delta \gg \Gamma$ where Γ is the transition linewidth, the scattering rate can be approximated as:

$$\mathcal{R} = \Gamma \frac{|\Omega_{\uparrow \rightarrow P}|^2 + |\Omega_{\downarrow \rightarrow P}|^2}{\Delta^2}. \quad (2.28)$$

Raman scattering rate puts a hard limit on the achievable fidelity of quantum gates. One can expect that the time necessary for single qubit rotations is inversely proportional to Ω_{eff} . The scattering probability during a single qubit gate will then be $\sim \mathcal{R}/\Omega_{\text{eff}} \sim 1/\Delta$. This points to the direction of using larger detuning Δ at the expense of higher laser power [62].

Raman transitions have been used to generate multi-qubit logic gates or spin-spin interactions between the ions. By controlling the strength and duration of the Raman pulses, one can induce off-resonant excitations of certain phonon modes of an ion crystal depending on the internal states of the ions, which results in spin-spin interactions. This technique has been used to simulate quantum magnetism [63–65] and to generate complex entangled states of multiple ions [66].

2.2.2 Spin-spin interactions

By introducing an extra detuning μ from one of the states \uparrow or \downarrow it is possible to drive transitions between motional states $(n \rightarrow n')$ of one or more crystal modes m . In order to do so the effective wavevector $\mathbf{k}_{\text{eff}} = \mathbf{k}_1 - \mathbf{k}_2$ between two Raman wavevectors \mathbf{k}_1 and \mathbf{k}_2 needs to have some overlap with the target mode of vibration \mathbf{b}_m such that $\mathbf{b}_m \cdot \mathbf{k}_{\text{eff}} \neq 0$. When $n' = n \pm 1$ we,

respectively, speak of *blue* and *red* side-bands. A blue side-band transition excites the vibration modes of an ion crystal by driving the $|\downarrow, n\rangle \rightarrow |\uparrow, n+1\rangle$ transition. A red side-band transition instead drives $|\downarrow, n\rangle \rightarrow |\uparrow, n-1\rangle$.

We can then replace the \mathbf{r}_j term in Eq. (2.25) with:

$$r_j^{(i)} = \sum_{m=1}^{3N} b_{j,m}^{(i)} \sqrt{\frac{\hbar}{2M\omega_m}} (\hat{a}_m^\dagger + \hat{a}_m), \quad (2.29)$$

where $i = x, y, z$ and $b_{j,m}^{(i)}$ represents the m -th eigenvector component for the j -th ion in the i -direction. We can then express the terms in Eq. (2.25) compactly in terms of the *Lamb-Dicke* parameter as:

$$e^{\mathbf{k}_{\text{eff}} \cdot \mathbf{r}_j} = \exp \left(\sum_{m=1}^{3N} \eta_j^m (\hat{a}_m^\dagger + \hat{a}_m) \right), \quad (2.30)$$

with $\eta_j^m = \mathbf{k}_{\text{eff}} \cdot \mathbf{b}_j^m \sqrt{\frac{\hbar}{2M\omega_m}}$ the Lamb-Dicke parameter for the motional mode m . At low enough temperatures, when $\eta_j^m \ll 1$ it is possible to Taylor expand the exponential terms. We refer to this as a *Lamb-Dicke approximation* when the wavefunction spread of the m -th harmonic oscillator is smaller than the laser wavelength. We can write Eq. (2.25) in the Lamb-Dicke limit and in the interaction picture with respect to Eq. (2.23) [45]:

$$\mathcal{H}_I \approx -i \sum_{j=1}^N \Omega_j \cos(\mu t) \hat{\sigma}_x^j \sum_{m=1}^{3N} \eta_j^m (\hat{a}_m^\dagger + \hat{a}_m), \quad (2.31)$$

with μ the frequency offset (beat-note) between the two Raman beams. The system can be further simplified by choosing a \mathbf{k}_{eff} direction that overlaps with only one direction of motion. In this case the last sum term of Eq. (2.31) reduces from $3N$ to N . In our setup we plan to make use of only the motional modes in the crystal plane as they are less affected by micromotion. In this case the effective wavevector lays in the crystal plane and couples to, at most, $2N$ modes.

The Raman lasers' beat-note frequency is kept far detuned from each motional mode transition in order to avoid to resonantly excite vibrations in the crystal that can lead to changes in the motional states. For a large enough detuning the effective Hamiltonian of the system reduces to that of an Ising interaction [67–70]:

$$\mathcal{H}_{\text{Ising}} = \sum_{j \neq i}^N J_{j,i} \hat{\sigma}_x^j \hat{\sigma}_x^i, \quad (2.32)$$

with:

$$J_{j,i} = g_i g_j \frac{\hbar k_{x,\text{eff}}^2}{2M} \sum_{m=1}^N \frac{b_{j,m} b_{i,m}}{\mu^2 - \omega_m^2}, \quad (2.33)$$

where $k_{x,\text{eff}}$ is the effective wavevector component in the x -direction.

2.3 OPTICAL TWEEZERS

An ion placed in a light field with intensity $I(r)$ will experience an induced dipole moment proportional to the light electric field \mathbf{E} . The proportionality constant α is called the *dynamic polarizability* and, using a classical Lorentz's description of the atom, can be written as [71]:

$$\alpha(\omega) = 6\pi\epsilon_0 c^3 \frac{\Gamma/\omega_j}{\omega_j^2 - \omega^2 - i(\omega^3/\omega_j^2) \Gamma_j}, \quad (2.34)$$

where ω_j is the optical transition frequency of state j and Γ_j is its decay rate. This approximation is valid for a large detuning $\omega_j \gg \omega$ or $\omega \gg \omega_j$ and low saturation. An ion immersed in a monochromatic laser field will experience a dipole force $\mathbf{F}(r) = -\nabla U(\mathbf{r})$ where the dipole potential U is defined as:

$$U(\mathbf{r}) = -\frac{1}{2\epsilon_0 c} \text{Re}(\alpha) I(r). \quad (2.35)$$

Using Eq. (2.34), we rewrite $U(\mathbf{r})$ as [71]:

$$U(\mathbf{r}) = -\sum_j \frac{3\pi c^2}{2\omega_j^3} \left(\frac{\Gamma_j}{\omega_j - \omega} + \frac{\Gamma_j}{\omega_j + \omega} \right) I(\mathbf{r}), \quad (2.36)$$

where the sum runs over all internal states j . From Eq. (2.36) we distinguish two limits $\omega \ll \omega_j$ (red detuning) and $\omega \gg \omega_j$ (blue detuning). In the first case the dipole potential will be attractive while in the second case repulsive.

Even in the case of far detuning, laser light on the ions can induce unwanted off-resonant scattering. It is important to minimize the scattering rate as it can cause the loss of quantum information encoded in the internal state of ions.

We can estimate the scattering rate for transition j as [71]:

$$\mathcal{R}_j = \frac{3\pi c^2}{2\hbar\omega_j^3} \left(\frac{\omega}{\omega_j} \right)^3 \left(\frac{\Gamma_j}{\omega_j - \omega} + \frac{\Gamma}{\omega_j + \omega} \right)^2 I(\mathbf{r}), \quad (2.37)$$

where Γ_j is the decay rate of the transition.

2.3.1 Stark shift

As this thesis focuses on the application of optical tweezers on trapped ions it is necessary to study the effect of the external electric field generated by optical fields on the internal structure of the ions.

In the presence of an external electric field atoms experience the so-called *Stark shift*. The interaction between an external electric field and an atom is described by:

$$\mathcal{H}_{\text{Stark}} = -\mathbf{d} \cdot \mathbf{E}, \quad (2.38)$$

where \mathbf{E} is an external electric field and \mathbf{d} the atomic dipole operator. The interaction term $\mathcal{H}_{\text{Stark}}$ generates an energy-level shift in the atomic level $|\gamma\rangle$. This can be calculated up to second-order perturbation theory:

$$\delta E_\gamma = \langle \gamma | \mathcal{H}_{\text{Stark}} | \gamma \rangle + \sum_{\gamma_j} \frac{|\langle \gamma | \mathcal{H}_{\text{Stark}} | \gamma_j \rangle|^2}{E_\gamma - E_{\gamma_j}} + \mathcal{O}\left(\langle \gamma | \mathcal{H}_{\text{Stark}} | \gamma \rangle^3\right). \quad (2.39)$$

As the dipole operator can only couple states with opposite parity, the first order perturbation term vanishes. The electric field generated by a laser with polarization ϵ can be written as:

$$\mathbf{E}(\omega) = \frac{1}{2} \mathcal{E}_L \epsilon e^{-i\omega t} + \text{c.c.}, \quad (2.40)$$

with the electric field amplitude \mathcal{E}_L . We can write the total shift due to the rotating and counter-rotating terms of the electric field as:

$$\delta E_\gamma = -\left| \frac{1}{2} \mathcal{E}_L \right|^2 \sum_{\gamma_j} \left(\frac{|\langle \gamma | \mathbf{d} \cdot \epsilon | \gamma_j \rangle|^2}{E_\gamma - \hbar(\omega_j - \omega)} + \frac{|\langle \gamma_j | \mathbf{d} \cdot \epsilon | \gamma \rangle|^2}{E_\gamma - \hbar(\omega_j + \omega)} \right). \quad (2.41)$$

Eq. (2.41) can be rewritten in terms of irreducible tensors. A more detailed derivation of this can be found in Appendix A. The total AC stark shift can be expressed as [72]:

$$\delta E_\gamma = -\left| \frac{1}{2} \mathcal{E}_L \right|^2 \sum_{\gamma_j} |\langle \gamma | \hat{\chi}(\omega) | \gamma_j \rangle|^2, \quad (2.42)$$

with:

$$\begin{aligned} \hat{\chi}(\omega) = & \sum_{K=0,1,2} \{ \epsilon^* \otimes \epsilon \}_K \cdot \left\{ \frac{\mathbf{d} \otimes \mathbf{d}}{E_\gamma - \hat{H}_0 - \omega} \right\}_K + \\ & (-1)^K \{ \epsilon^* \otimes \epsilon \}_K \cdot \left\{ \frac{\mathbf{d} \otimes \mathbf{d}}{E_\gamma - \hat{H}_0 + \omega} \right\}_K. \end{aligned} \quad (2.43)$$

We can evaluate the tensor operator $\hat{\chi}(\omega)$ on the unperturbed Hamiltonian H_0 . For a hyperfine energy state $|\gamma\rangle$ we have $|\gamma\rangle \equiv |n, J, F, M\rangle$ such that:

$$\begin{aligned}\alpha_K(\omega) &= \langle n, J, F, M | \left\{ \frac{\mathbf{d} \otimes \mathbf{d}}{E_\gamma - \hat{H}_0 - \omega} \right\}_K + (-1)^K \left\{ \frac{\mathbf{d} \otimes \mathbf{d}}{E_\gamma - \hat{H}_0 + \omega} \right\}_K |n, J, F, M\rangle \\ &= \langle n, J, F, M | \left(\sum_{J', F', M'} \mathbf{d} |J', F', M'\rangle \langle J', F', M'| \mathbf{d} \right)^{(K)} |n, J, F, M\rangle \times \\ &\quad \times \frac{1}{E_{n, J, F, M} - E_{n, J', F', M'} - \omega} + (-1)^K \frac{1}{E_{n, J, F, M} - E_{n, J', F', M'} + \omega},\end{aligned}\quad (2.44)$$

where we identify the scalar ($K = 0$), vector ($K = 1$) and tensor ($K = 2$) polarizabilities. Making use of the Wigner-Eckart theorem it is possible to express the various components in terms of the reduced dipole matrix elements $\langle F, J | |\mathbf{d}| |F', J' \rangle$ as follows [73]:

$$\alpha^{(0)}(\omega) = \sum_{F'} \frac{2\omega_{F', J' \rightarrow F, J} |\langle F, J | |\mathbf{d}| |F', J' \rangle|^2}{3\hbar(\omega_{F', J' \rightarrow F, J}^2 - \omega^2)}, \quad (2.45)$$

$$\alpha^{(1)}(\omega) = \sum_{F'} (-1)^{F+F'+1} \sqrt{\frac{6F(2F+1)}{F+1}} \left\{ \begin{array}{ccc} 1 & 1 & 1 \\ F & F & F' \end{array} \right\} \frac{\omega |\langle F, J | |\mathbf{d}| |F', J' \rangle|^2}{\hbar(\omega_{F', J' \rightarrow F, J}^2 - \omega^2)}, \quad (2.46)$$

$$\begin{aligned}\alpha^{(2)}(\omega) &= \sum_{F'} (-1)^{F+F'} \sqrt{\frac{40F(2F+1)(2F-1)}{3(F+1)(2F+3)}} \left\{ \begin{array}{ccc} 1 & 1 & 2 \\ F & F & F' \end{array} \right\} \times \\ &\quad \times \frac{\omega_{F', J' \rightarrow F, J} |\langle F, J | |\mathbf{d}| |F', J' \rangle|^2}{\hbar(\omega_{F', J' \rightarrow F, J}^2 - \omega^2)},\end{aligned}\quad (2.47)$$

where the reduced matrix elements $|\gamma\rangle \equiv |n, J, F, M\rangle$ can be further refined using the Wigner-Eckart theorem as:

$$\begin{aligned}\langle F, J | |\mathbf{d}| |F', J' \rangle &= \langle J | |\mathbf{d}| |J' \rangle (-1)^{F'+J+1+I} \sqrt{(2F'+1)(2J+1)} \times \\ &\quad \times \left\{ \begin{array}{ccc} J & J' & 1 \\ F' & F & I \end{array} \right\}.\end{aligned}\quad (2.48)$$

The total polarizability of the state $|n, J, F, m\rangle$ is therefore:

$$\begin{aligned}\alpha_F(\omega) &= \alpha^{(0)}(F, \omega) + C \cos(\theta_k) \frac{m_F}{F} \alpha^{(1)}(F, \omega) + \\ &\quad + \left(\frac{3 \cos^2(\theta_p) - 1}{2} \right) \left[\frac{3m_F^2 - F(F+1)}{F(2F-1)} \right] \alpha(F, \omega)^{(2)},\end{aligned}\quad (2.49)$$

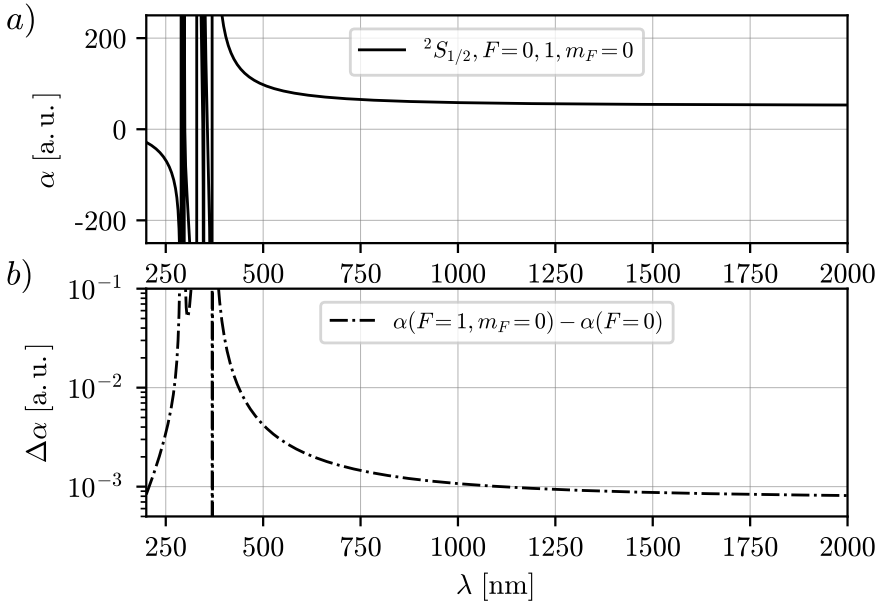


FIGURE 2.5: $^{171}\text{Yb}^+$ $^2S_{1/2}$ state dynamic polarizability for linearly polarized light in the absence of a magnetic field. a) Absolute polarizability of hyperfine states. b) Differential polarizability of states $F = 1, m_F = 0$ and $F = 0$.

where C is the degree of polarization as defined in Appendix A.3. We defined the angles θ_k and θ_p respectively as the angle between the light wavevector and the quantization axis, and the angle between the quantization axis and the direction of polarization. In the absence of a magnetic field we assume the quantization axis to be coincident with the light propagation direction. In the absence of a magnetic field and with linearly polarized light, $\theta_k = \pi/2$ and $\theta_p = 0$.

Notice, that the polarizability tensor contains an off diagonal component that was ignored in our calculations, see appendix A.3. In general this term is much smaller than the energy levels splitting and can be ignored.

The utilization of the irreducible representation of the polarization tensor not only simplifies the equations but also offers valuable insights into the underlying physics associated with each component. Specifically, the scalar component contributes to a level independent shift, similar to the effect of a DC electric field. On the other hand, the vector component induces a shift that depends on the m_F substates, resembling the behavior of a magnetic field,

and is exclusively generated by circularly polarized light. Lastly, the tensorial component is dependent on m_F^2 and represents the second-order response of an atom to an applied electric field. Understanding these distinct components of the polarizability vector provides a comprehensive understanding of how atoms respond to external electromagnetic fields and sheds light on the physical phenomena associated with them.

In the literature the tensor polarizability is often given after contracting the two sums over F' and m' as $E_{J,F,m_F} \approx E_J$. This is usually a good assumption for many atomic systems, however, for the scope of this thesis this relatively small hyperfine shift has to be taken into account. In fact, the AC Stark interaction effectively shifts the qubits resonant frequency and has to be taken into account when implementing quantum operation in the presence of optical tweezers.

For example, when considering the polarizability of $^{171}\text{Yb}^+$ the hyperfine splitting between the two ground state sublevels leads to a non-negligible differential polarizability, as shown in Fig. 2.5 in case of linearly polarized light.

2.3.2 Optical tweezers potential

The dipole potential generated by tightly focused laser light can be used to modify the ions' trapping potential given in Eq. (2.20).

We can approximate the potential generated by the optical tweezers as an additional harmonic potential. This approximation is valid when $\eta_{\text{tw}} \ll 1$, where η_{tw} is the ratio between the spread of the ions' wavefunction l_{HO} to the diffraction limit d of the laser beams:

$$\eta_{\text{tw}} = \frac{l_{\text{HO}}\sqrt{\bar{n}}}{d} = \sqrt{\bar{n}}\sqrt{\frac{\hbar}{2M\omega_{\text{HO}}}\frac{2\text{NA}}{\lambda}}, \quad (2.50)$$

where \bar{n} is the ions' average phonon number, ω_{HO} is the trapping frequency and NA is the numerical aperture of the optical system. For typical systems $l_{\text{HO}} \sim 10 \text{ nm}$, $\text{NA} \sim 0.5$ such that $\eta_{\text{tw}} \sim 10\sqrt{n}/\lambda \ll 1$ with λ expressed in nm.

Under this approximation we can expand the beam at its center. For the scope of this thesis we are interested in the field generated by Gaussian or Laguerre-Gaussian (LG) beams. Tab. 2.1 gives the normalized intensity equations for a Gaussian and Laguerre-Gaussian ($p = 0, l = 1$) beam and their expansion near the center of the beams. Neglecting a global shift in the

Beam Shape	Normalized power ($P(\rho)/P_0$)	$\rho \approx 0 + \mathcal{O}(\rho^4)$
Gaussian	$\frac{2}{\pi w_0^2} e^{-2\rho^2/w_0^2}$	$\frac{2}{\pi w_0^2} - \frac{4\rho^2}{\pi w_0^4}$
LG	$\frac{2}{\pi w_0^2} \left(\frac{\sqrt{2}\rho}{w_0} \right)^{2l} \frac{1}{l!} \mathcal{L}_p^l \left(\rho^2/w_0^2 \right) e^{-2\rho^2/w_0^2}$	
LG ($p = 0, l = 1$)	$\frac{4\rho^2}{\pi w_0^4} e^{-2\rho^2/w_0^2}$	$\frac{4\rho^2}{\pi w_0^4}$

TABLE 2.1: Second order expansions for Gaussian and Laguerre-Gaussian beams near the center up to second order. Notice that although the general LG intensity shape is not normalized, the one for $p = 0, l = 1$ is.

case of a Gaussian beam, we can approximate the field generated by both beams as:

$$U(\omega, x) = \text{sign}[\alpha(\omega)] \frac{1}{2} M \omega_{\text{tw}}^2(\omega) x^2, \quad (2.51)$$

with:

$$\omega_{\text{tw}}(\omega) = \sqrt{\frac{8|\alpha(\omega)| P_0}{2\pi\epsilon_0 c M w_0^4}}, \quad (2.52)$$

where w_0 and P_0 are the beam waist and power respectively. Notice that the mechanical effect of this potential on the ions (trapping or anti-trapping) is defined by the sign of the polarizability α . This expansion is valid for both Gaussian or Laguerre-Gaussian beam shapes as the second order coefficient of their expansion near the center is the same. Note that this is not the case for all other orders of the expansion. The global offset for a Gaussian beam does not affect the potential, although it has to be taken in account when considering scattering rates and differential stark shifts induced on the ions.

2.4 ENGINEERING OF VIBRATIONAL MODES USING OPTICAL TWEEZERS

Under the approximations that lead to Eq. (2.51) it appears evident that optical tweezers can be used to induce local changes in the trapping potential of the ions. Starting from ions in a Paul trap whose potential is defined in Eq. (2.20), we can study the mechanical effects generated by optical tweezers. The additional potential term generated by the presence of optical tweezers on k ions is:

$$V_{\text{tw}} = \sum_k \frac{1}{2} M \Omega_\mu^k \Omega_\nu^k \epsilon_k^\mu \epsilon_k^\nu, \quad (2.53)$$

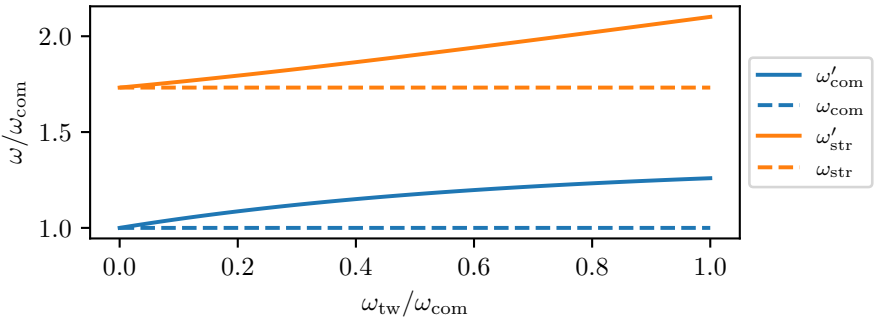


FIGURE 2.6: Effect of adding a trapping tweezer on one of the ions in a two ion crystal. The original axial mode eigenfrequencies ω_{com} and ω_{str} (dashed lines) are shifted to ω'_{com} and ω'_{str} respectively, depending on the tweezer's strength ω_{tw} .

where we defined ϵ_k' as the equilibrium position of ion k and Ω_μ^k as the vector containing the tweezer's strength on the same ion along the \hat{e}_k direction.

The total potential experienced by the ions is given by $V_{\text{tot}} = V_{\text{trap}} + V_{\text{Coulomb}} + V_{\text{tw}}$ where V_{trap} and V_{Coulomb} are, respectively, the potentials generated by the Paul trap and the Coulomb interaction as described in Eq. (2.17) and Eq. (2.18).

From this modified potential we can follow the derivation described in section 2.1.5 and expand V_{tot} to second order as from Eq. (2.20). The Lagrangian of the system will now be dependent on a Hessian matrix similar to the one defined in Eq. (2.22). This new Hessian, however, also contains the additional terms coming from the potential generated by optical tweezers. As described in Sec. 2.1.5 the new Hessian matrix can be diagonalized to find the new eigenvectors \mathbf{b}' and eigenvalues ω'_m of the system.

For a two ($N = 2$) ion linear chain we can provide an analytical expression for the new eigenmodes in the presence of one optical tweezer ω_{tw} on one of the two ions. The new eigenfrequencies in the axial direction are:

$$\begin{aligned}\omega'_1 &= \frac{1}{\sqrt{2}} \sqrt{\omega_{\text{tw}}^2 + 4\omega_z^2 - \sqrt{\omega_{\text{tw}}^4 + 4\omega_z^4}}, \\ \omega'_2 &= \frac{1}{\sqrt{2}} \sqrt{\omega_{\text{tw}}^2 + 4\omega_z^2 + \sqrt{\omega_{\text{tw}}^4 + 4\omega_z^4}},\end{aligned}\quad (2.54)$$

where ω_z is the axial trapping frequency provided by the Paul trap alone. Fig. 2.6 shows the shift in trapping frequencies caused by optical tweezers on the axial modes.

Notice that in the limit $\omega_{\text{tw}} \rightarrow 0$ we recover the native $\omega'_1 = \omega_z$ and $\omega'_2 = \sqrt{3}\omega_z$. If $\omega_{\text{tw}} \rightarrow \infty$ instead, we have $\omega'_1 \rightarrow \sqrt{2}\omega_z$ and $\omega'_2 \rightarrow \infty$. In this regime the eigenmodes of vibration are strongly modified by the presence of the tweezers. As such, then we can no longer consider the ions' motion in terms of the usual center of mass ($\mathbf{b}_1 = 1/\sqrt{2}[1, 1]$) and stretch mode ($\mathbf{b}_2 = 1/\sqrt{2}[-1, 1]$). Instead, the motion has to be expanded in terms of the new eigenbasis. It is possible to define a transformation matrix from the original unperturbed regime to the one in presence of the tweezers as:

$$\mathbf{b}'_n = \mathcal{T}_{\text{tw}} \cdot \mathbf{b}_n, \quad (2.55)$$

$$\mathbf{b}'_n = \begin{bmatrix} \frac{\sqrt{\omega_{\text{tw}}^4 + 4\omega_z^4}}{2\omega_z^2} & -\frac{\omega_{\text{tw}}^2}{2\omega_z^2} \\ 0 & 1 \end{bmatrix} \mathbf{b}_n,$$

where we define \mathcal{T}_{tw} as the matrix transforming the system into the new basis and gave its values for the system here described. In the strong tweezers regime we find that the new renormalized eigenvectors are $\mathbf{b}'_1 = [1, 0]$ and $\mathbf{b}'_2 = [0, 1]$.

The expression of Eq. (2.55) also holds in the general case of $N \neq 2$. An analytical expression for a general N ions case in the perturbed situation is not feasible, so numerical solutions must be utilized. To obtain the diagonal hessian matrix in the unperturbed basis, we begin with the unperturbed case and write $\mathcal{A}_{\text{u}} = \mathcal{D}^{-1} \mathcal{A} \mathcal{D}$, where \mathcal{D} is the invertible matrix that diagonalizes the Hessian and \mathcal{A}_{u} is the diagonal hessian matrix in the unperturbed basis. In the perturbed case $\mathcal{A}' = \mathcal{T}_{\text{tw}}^{-1} \mathcal{D}^{-1} \mathcal{A} \mathcal{D} \mathcal{T}_{\text{tw}}$, with \mathcal{A}' the new perturbed Hessian matrix. This can be further refined as $\mathcal{A}'_{\text{u}} = \mathcal{T}_{\text{u}}^{-1} \mathcal{A}' \mathcal{T}_{\text{u}}$, with $\mathcal{T}_{\text{u}} = \mathcal{D} \mathcal{T}_{\text{tw}} \mathcal{D}'$, where \mathcal{D}' is the matrix that diagonalizes the perturbed Hessian matrix. \mathcal{T}_{u} is the transformation matrix between an unperturbed non-diagonal Hessian to a diagonal perturbed one.

It is also worth noticing that local changes caused by optical tweezers generate global changes in the eigenfrequencies and eigenmodes of the whole crystal. In other words, site-selective potentials can be used to modify the system at a global scale.

A similar treatment can be followed for the radial modes of vibration. In the case of the two ion chain we can obtain similar expressions for the eigenfrequencies. Assuming that the confinement provided by the trap is

degenerate in the x - and y -directions such that $\omega_x = \omega_y = \omega_r$, the new eigenfrequencies in the radial direction are:

$$\begin{aligned}\omega'_3 &= \frac{1}{\sqrt{2}} \sqrt{\omega_{\text{tw}}^2 + 2\omega_r^2 - \omega_z^2 - \sqrt{\omega_{\text{tw}}^4 + \omega_z^4}}, \\ \omega'_4 &= \frac{1}{\sqrt{2}} \sqrt{\omega_{\text{tw}}^2 + 2\omega_r^2 - \omega_z^2 + \sqrt{\omega_{\text{tw}}^4 + \omega_z^4}}.\end{aligned}\quad (2.56)$$

Thus, we have shown how optical tweezers can be used to modify the motional eigenmodes and eigenfrequencies of a trapped ion system. That is, the addition of local potentials generated by optical tweezers can have an effect on the whole motional spectrum of a trapped ion crystal. In the strong tweezers regime the effect is such that the original vibrational modes are completely mixed, forming a new complete set.

2.4.1 Tuning spin-spin interactions

In Section 2.2.2 we demonstrated how to achieve phonon-mediated spin-spin interactions between ions using a global Raman scheme. This type of interaction is not only valuable for generating entangling gates that are beneficial in quantum computing, but also for quantum simulations. Hamiltonians such as the spin-1/2 Hamiltonian shown in Eq. (2.32) are of particular interest since they can display a high level of spin frustration. These types of Hamiltonians are usually too challenging to simulate on a classical computer, but they can be engineered in trapped ions. Therefore, highly frustrated quantum many-body systems can be simulated on such platforms, allowing for new theoretical insights.

Nevertheless, in practice, it is often challenging to realize an ideal Hamiltonian due to various sources of noise and imperfections in the physical system such as imperfect control over the system parameters or fluctuations in the environment. As a result, the system Hamiltonian will differ from the ideal one. The difference can be quantified using an error ϵ_I that we need to minimize, typically the difference between the ideal Hamiltonian and the actual Hamiltonian, and it can be caused by factors such as imperfect control over the system parameters or fluctuations in the environment.

In addition, the set of Hamiltonians that can be implemented on these systems is limited by certain experimental constraints. Specifically, the range of Hamiltonians that can be realized on trapped ions is limited to those that have a power-law decay of $1/r^\alpha$ with $0 \leq \alpha \leq 1.5$, as demonstrated by previous research [74]. While theoretical considerations suggest that the range of Hamiltonians could be expanded to $\alpha \leq 3$, the experimental constraints

on trapped ions currently limit the range to the aforementioned power-law decay rates.

These limitations can however be relaxed when including the perturbations on eigenmodes and eigenfrequencies generated by optical tweezers. In fact, the spin-spin coupling between ion i and j given in Eq. (2.33) depends not only on the Raman beatnote μ but also on the eigenfrequencies and eigenmodes of the system. These can be modified, as shown in section 2.4, by the presence of optical tweezers. This gives rise to new degrees of freedom compared to Eq. (2.33) by having the ability of controlling $\mathbf{b} \rightarrow \mathbf{b}'$ and $\omega_m \rightarrow \omega'_m$. The spin-spin interaction strength of Eq. 2.33 then becomes:

$$J_{j,i} = g_i g_j \frac{\hbar k_{x,\text{eff}}^2}{2M} \sum_{m=1}^N \frac{b'_{j,m} b'_{i,m}}{\mu^2 - (\omega'_m)^2}. \quad (2.57)$$

This shows that by using optical tweezers, it is possible to improve the range of experimentally realizable Hamiltonians beyond the limitations imposed by traditional methods. Specifically, by adjusting the shape of the site-selective tweezers potential, it has been shown [45] that it is possible to approximate power-law interactions with $\alpha > 3$ without being affected by current experimental limitations. This demonstrates the potential of optical tweezers in expanding the range of Hamiltonians that can be simulated on trapped ions.

Moreover, the addition of optical tweezers allows for greater control over the system and can help to reduce errors between the system's Hamiltonian and the target one, thus improving the experimental fidelity. Therefore, optical tweezers have the potential to greatly enhance the capabilities of trapped ion quantum simulators, enabling more accurate and efficient simulations of complex quantum systems.

Optical tweezers can not also lead to further advancements in the study of quantum thermodynamics. Specifically, the effect of optical tweezers is somewhat similar to an effective change in the mass of the trapped ions, which can increase the motional coupling between ions of different species and enable improved sympathetic cooling [51]. This has implications for the study of quantum thermodynamics of particles with programmable mass, as the mass of the trapped ions can be dynamically controlled using optical tweezers [51].

Finally, it is possible to combine optical tweezers with multiple beatnote frequencies in the Raman laser [75, 76] at the expenses of additional experimental complexity. This can help to further increase the tunability of the system.

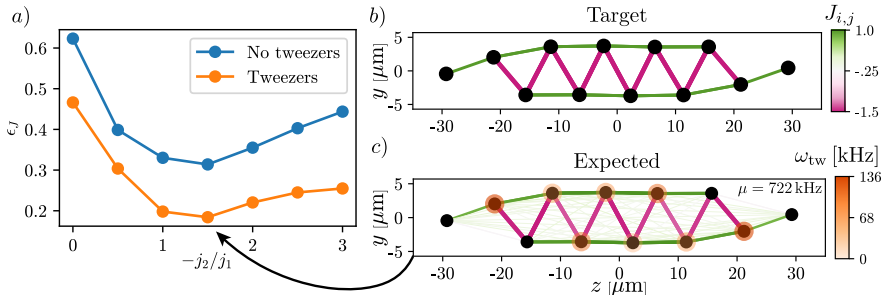


FIGURE 2.7: a) Comparison between w/wo tweezers coupling error ϵ_J for different coupling strength ratios $-j_2/j_1$. b) Target couplings $J_{i,j}$. c) Expected coupling strengths when using a beatnote at frequency $\mu = 722$ kHz and a tweezers pinning frequencies as shown in orange halos. The figure is adapted from Ref. [57].

2.4.2 Optimizing tweezers patterns

We have shown how optical tweezers can modify the phonon spectrum and in turn, modify the spin-spin interactions in the system. However, now a new questions arise. Having a spin-spin Hamiltonian of interest, can this be realized in our system? And if yes, how do we find the optimal tweezer pattern that would realize it?

Starting from an ideal spin-spin coupling $J_{j,i}^{\text{id}}$ and a realizable $J_{j,i}^{\text{exp}}$ we can define the distance ϵ_J between the two as:

$$\epsilon_J = \sqrt{\sum_{j,i}^N \left(J_{j,i}^{\text{id}} - J_{j,i}^{\text{exp}} \right)^2} / \sqrt{\sum_{j,i}^N \left| J_{j,i}^{\text{id}} \right|^2}. \quad (2.58)$$

It is possible to use various optimization procedures in order to find the most accurate tweezer pattern that minimizes the error ϵ_J [45, 77]. Considering the total size of the parameter space this is not a trivial task. Most importantly one has to keep in mind the limitations coming from experimental parameters. And, when choosing the Raman detuning μ this has to be far away ($\gtrsim 10$ kHz) from any of the modes frequencies in order to avoid to resonantly excite crystal's vibrations.

2.4.3 Example: spin ladder

The use of optical tweezers in engineering spin ladder models on trapped ions offers several advantages worth exploring. In particular we consider the

ferromagnetic zig-zag model, with $j_1 > 0$ (the rails of the ladder) and $j_2 < 0$ (the rungs). The zig-zag model (see Fig. 2.7 b)) is an interesting and important topic of study in condensed matter physics. It exhibits frustration and allows for the investigation of spontaneous symmetry breaking. The model offers a wide range of coupling strengths j_1, j_2 , enabling the exploration of different regimes and the study of the interplay between frustration and fluctuations. Its complexity arises from the absence of an exact analytical solution, making it a challenging yet rewarding problem to tackle. Studying the spin ladder model can lead to new insights on the behavior of quantum systems with competing interactions and quantum fluctuations.

While the spin ladder system can be engineered in trapped ions without the use of optical tweezers as from Eq. (2.33), incorporating optical tweezers can enhance the accuracy and fidelity of the experimental realization. By reducing the error ϵ_J between the theoretical model and its practical implementation, optical tweezers contribute to the improvement of quantum simulations in trapped ions.

Fig. 2.7 a) shows a comparison between the predicted spin ladder interactions in trapped ions with or without the aid of optical tweezers for different coupling ratios j_2/j_1 between the rails and the rungs of the ladder. From the plot we see that the usage of optical tweezers can reduce the experimental realization error especially in the regime where $-j_2/j_1 > 1.5$.

It is important to note that while we have focused on spin ladder systems, the application of optical tweezers extends to the engineering of spin-spin interactions in other one-dimensional (1D) or two-dimensional (2D) systems of interest. This includes spin frustrated models found in triangular and kagome lattices, among others [78, 79].

2.4.4 *Experimental considerations*

Strong tweezer confinement can not be provided in the direction of propagation of the laser beams. In this case the potential of Eq.(2.51) can be reduced to two dimensions.

In the setup described in this thesis, tweezers can be applied to ions lying in a z - x plane ($\mu, \nu = 1, 3$) from a direction perpendicular to the plane. In this case the potential will predominantly affect only the in-plane modes that are usually at lower frequencies compared to the out-of-plane modes as shown in Fig. 2.2 for 12 ions. As the tweezers potential has to compete with the, usually, strong harmonic potential generated by a Paul trap, the effect on low frequency modes is more noticeable.

Eq.(2.53) does not take into account any possible displacements between the center of the tweezer potential and the ions' equilibrium position. It can

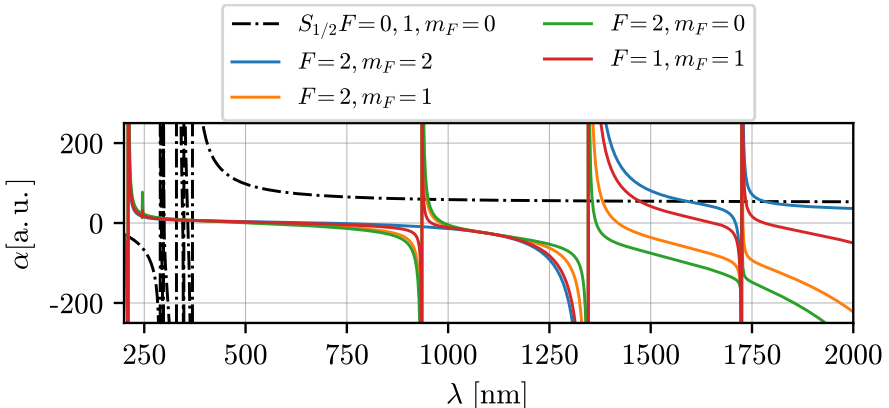


FIGURE 2.8: Calculated $^{171}\text{Yb}^+$ dynamic polarizability for $^2S_{1/2}$ (dashed black) and all F substates (colored) of $^2D_{3/2}$ in the case of linearly polarized light. Notice that, for example, states $^2S_{1/2}$ and $^2D_{3/2}, F = 2, m_F = 0$ (green) have significant opposite polarizabilities at $\lambda(\alpha) = 914(67), 1300(63), 1489(62), 1726(61)$ nm (a.u.).

be shown [45] that small misalignments < 50 nm lead to negligible effects compared to the perfectly aligned case. Nonetheless tweezers misalignment can be used to provide local stress to the ion crystal. This allows for more degrees of freedom and can be exploited to further control the phonon spectra of the crystal [57].

Another effect worth considering is micromotion in the presence of optical tweezers [57]. Micromotion leads to an effective change in the mode structure that has to be taken into account when calculating the effective spin-spin interactions between ions. Furthermore it causes a first order Doppler shift that effectively modulates the spin-spin interaction for each ion. This effect can lead to a significant source of errors on the interaction strength. For this reason it is convenient to engineer spin spin interactions using motional modes for which micromotion has minimal effect as, for example the in-plane (z - x) modes of a two-dimensional ion crystal (see Sec. 2.1.4).

Finally, as the tweezer trapping frequencies are proportional to the laser power, particular attention has to be given to intensity fluctuations. It has been shown [57] that in order to take advantage of optical tweezers, intensity noises have to be kept under the 1% level.

2.4.5 *Spin-dependent optical tweezers*

Optical tweezers can also be used to create quantum logic gates between ions. The approach involves modifying the phonon spectra of an ion crystal in a spin-dependent manner. This can be accomplished by selecting two states that exhibit distinct behavior when exposed to optical tweezers.

For instance, one could identify two internal states with opposite polarizabilities, such that when one state experiences a stronger trapping potential (as from Eq. (2.51)) the other experiences a weaker trapping potential. Fig. 2.8 provides an example of this, where certain laser frequencies cause the $^2S_{1/2}$ state to have opposite polarizability compared to one of the F manifolds of the $^2D_{3/2}$ state.

Alternatively, a similar effect can be achieved by using optical tweezers near a quadrupole transition, where the two qubit states can experience opposite polarizability while keeping the scattering rate low. In chapter 3 and 4 we will show in detail how spin-dependent forces generated by optical tweezers can be exploited to engineer novel types of quantum logic gates.

3

ELECTRICAL FIELD GATE WITH OPTICAL TWEEZERS

Based on
Physical Review Letters **127**, 260502, (2021)

In this chapter we propose a new scalable architecture for trapped ion quantum computing that combines optical tweezers delivering qubit state-dependent local potentials with oscillating electric fields. Since the electric field allows for long-range qubit-qubit interactions mediated by the center-of-mass motion of the ion crystal alone, it is inherently scalable to large ion crystals. Furthermore, the proposed scheme does not rely on either ground state cooling or the Lamb-Dicke approximation. We study the effects of imperfect cooling of the ion crystal, as well as the role of unwanted qubit-motion entanglement, and discuss the prospects of implementing the state-dependent tweezers in the laboratory.

3.1 A NOVEL TWO-QUBIT GATE

Trapped ions form one of the most mature laboratory systems for quantum information processing and quantum simulation [35, 70, 80]. Many of the basic building blocks needed for these technologies have been demonstrated: high fidelity detection and preparation [81], and universal quantum operations performed by external fields coupling to the internal states of the ions. While quantum gates have been performed with very high fidelities in trapped ions [82–84], scaling up the system while maintaining the quality of operations has proven to be challenging. In particular, as the length of ion crystals increases, the number of motional modes to which the gate lasers couple also increases. This leads to a reduction of interaction strength for gates between distant qubits [85]. Furthermore, the number of degrees of freedom with which the qubits can erroneously entangle increases.

Here we propose a novel universal trapped ion quantum computing architecture which uses state-dependent optical tweezer potentials [45, 51, 86] combined with oscillating electric fields to overcome the obstacles described above. Since the electric fields only couple to the center-of-mass (COM) mode of the ion crystal, adverse effects of spectator modes that reduce the range of interaction are avoided. Moreover, our gate does not rely on the Lamb-Dicke

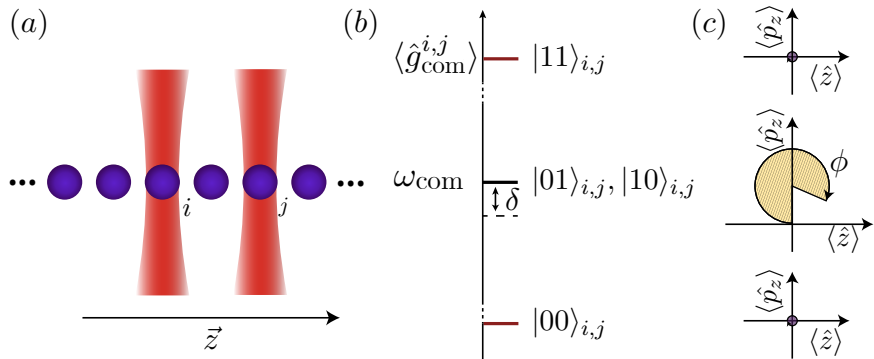


FIGURE 3.1: (a) Schematic representation of a linear chain of ions where optical tweezers are applied to ions *i* and *j*. The tweezers shift the COM mode depending on the internal state of the pair. (b) Level scheme of the four states; only the states $|01\rangle$ and $|10\rangle$ are unaffected by the extra trapping potential generated by the tweezers. (c) Phase space dynamics of the four states when adding an electric field at a frequency $\omega_{\text{com}} - \delta$. Due to the displacement generated by the driving electric field the states $|01\rangle$ and $|10\rangle$ acquire a phase ϕ .

approximation which requires the wavepackets of the ions to be confined to a space smaller than the wavelength of the laser implementing the gate. This extends the parameter regime for gate operation. The combination of such two-qubit gates with single-qubit gates can be used as a universal quantum computer.

We illustrate the gate mechanism applied to qubits *i* and *j* in Fig. 3.1. We simultaneously apply an electric field of amplitude E_0 oscillating close to the COM frequency (at detuning δ) and optical tweezers to the two addressed qubits. The gate works as follows: the tweezers shift the frequency of the COM mode in a state-dependent manner, such that for two qubits in the same state the electric field can no longer excite motion. Thus, the evolution of the system is dominated by phonon mediated effective spin-spin interactions $\propto E_0^2/\delta$. We perform a geometric phase gate by choosing the appropriate E_0 and δ . Since the interactions are merely mediated by the COM mode they are independent of distance. Additionally, the required tweezer power scales linearly with the number of ions in the crystal. Both those factors contribute to the scalability of our proposal.

3.2 REALIZING A GEOMETRIC PHASE GATE

Consider a crystal of N ions with masses M and charge e in a harmonic trap. The normal modes (phonon modes) and mode frequencies of the crystal can be found by diagonalizing the Hessian matrix \mathbf{A} [87]. Here $A^{(ij)} = d^2V/(d\alpha_i d\alpha_j)$, where α_i are small deviations about the equilibrium positions of the ions, and V is the total potential energy. The eigenvectors of the Hessian, denoted by \mathbf{b}_m , are the normal modes of the crystal. The mode frequencies are given by $\omega_m = \sqrt{\lambda_m}$ with λ_m the eigenvalues of \mathbf{A} . For a 1D ion crystal, the eigenmodes separate into three subclasses, corresponding to the directions of motion x, y, z . In the following we focus on the axial direction (z) characterized by the trapfrequency ω_z . We address a specific ion using tweezers formed by focused beams aligned on its equilibrium position, leaving the geometry of the crystal independent of the qubit states. Moreover, we will show that the laser parameters and qubit states can be chosen such that the dynamical polarizability of the qubit states $|0\rangle$ and $|1\rangle$ are of equal magnitude, but opposite sign. If the ions are confined to the tweezer waist, the tweezer potential can be approximated by a state-dependent harmonic potential: $\hat{H}_{\text{tw}}^{i,j} = \frac{1}{2}M\omega_{\text{tw}}^2(\hat{z}_i^2\hat{\sigma}_z^i + \hat{z}_j^2\hat{\sigma}_z^j)$. Here, $\hat{\sigma}_z^i$ ($\hat{\sigma}_z^j$) is the Pauli matrix operating on ion i (j) and \hat{z}_i (\hat{z}_j) is the position operator relative to the equilibrium position of ion i (j). The proposed gate requires the simultaneous application of the tweezers and an oscillating electric field generated by applying an rf-voltage to an electrode close to the ion crystal. The total Hamiltonian is then given by:

$$\hat{H} = \sum_m \omega_m \left(\hat{a}_m^\dagger \hat{a}_m + \frac{1}{2} \right) + \hat{H}_{\text{tw}}^{i,j} + \hat{H}_{\text{E}}(t), \quad (3.1)$$

with $\hat{H}_{\text{E}}(t)$ denoting the electric field interaction and \hat{a}_m^\dagger (\hat{a}_m) the creation (annihilation) operator of mode m . Since a homogeneous electric field E_0 only couples to the COM motion,

$$\hat{H}_{\text{E}}(t) = 2\gamma(\hat{a}_{\text{com}}^\dagger + \hat{a}_{\text{com}})\cos(\mu t),$$

where $\gamma = eE_0l_{\text{com}}/2$, $l_{\text{com}} = (2M\omega_{\text{com}})^{-1/2}$ and $\mu = \omega_{\text{com}} + \delta$ is the frequency of the electric field. If $\omega_{\text{tw}} \ll \omega_m$ for all modes, we can use perturbation theory to find the new mode frequencies in the presence of the tweezers: $\tilde{\omega}_m \approx \omega_m + \sum_k b_{mk} \hat{A}_{\text{tw}}^{(ij)} b_{mk} + \dots$ with $k = 1, \dots, N$. Here, the perturbation of the tweezers to the Hessian matrix is given by $\hat{A}_{\text{tw}}^{(ij)} = \omega_{\text{tw}}^2 (\hat{\sigma}_z^i + \hat{\sigma}_z^j)$. To first order,

$$\tilde{\omega}_m^{i,j} \approx \sqrt{\omega_m^2 + \omega_{\text{tw}}^2 (b_{mi}^2 \hat{\sigma}_z^i + b_{mj}^2 \hat{\sigma}_z^j)}. \quad (3.2)$$

which shows that the mode frequencies shift depending on the states of qubits i and j . In order to gain intuition about the dynamics generated by Eq. (3.1), we apply the unitary transformation $\hat{U}_1 = \exp [i(\delta\hat{a}_{\text{com}}^\dagger\hat{a}_{\text{com}} + \sum_m \omega_m \hat{a}_m^\dagger\hat{a}_m)t]$, as well as the rotating wave approximation, neglecting terms oscillating faster than δ . Next, we apply Lang-Firsov unitary transformation [88], $\hat{U}_2 = \exp [\hat{V}(\hat{a}_{\text{com}}^\dagger - \hat{a}_{\text{com}})]$, with $\hat{V} = \gamma(\hat{g}_{\text{com}}^{i,j} - \delta\mathbb{1})^{-1}$. This eliminates the first-order phonon coupling. The resulting Hamiltonian is,

$$\begin{aligned}\hat{H}_2 = & \sum_m \hat{g}_m^{i,j} (\hat{a}_m^\dagger \hat{a}_m + 1/2) - \delta \hat{a}_{\text{com}}^\dagger \hat{a}_{\text{com}} \\ & - \frac{\gamma^2}{2\delta} \hat{\sigma}_z^i \hat{\sigma}_z^j + \frac{\gamma^2}{g_{\text{com}}^+ - \delta} \hat{W}_+ + \frac{\gamma^2}{g_{\text{com}}^- - \delta} \hat{W}_-, \end{aligned}\quad (3.3)$$

with $\hat{W}_+ = |11\rangle_{ij}\langle 11|_{ij}$ and $\hat{W}_- = |00\rangle_{ij}\langle 00|_{ij}$ where we have dropped energy offset terms $\propto \mathbb{1}$. The operator $\hat{g}_m^{i,j} = \tilde{\omega}_m^{i,j} - \omega_m$ contains the qubit state dependence and g_{com}^\pm are calculated by setting $\hat{\sigma}_z^i + \hat{\sigma}_z^j \rightarrow \pm 2$. For the COM mode, $\mathbf{b}_{\text{com},i}^2 = \mathbf{b}_{\text{com},j}^2 = 1/N$ [87], thus $\hat{g}_{\text{com}}^{ij} = \sqrt{\omega_{\text{com}}^2 + \omega_{\text{tw}}^2} \left(\hat{\sigma}_z^{(i)} + \hat{\sigma}_z^{(j)} \right) / N - \omega_{\text{com}}$ (see Fig. 3.1). In the limit $\omega_{\text{tw}} \ll \omega_{\text{com}}$, we obtain $\hat{g}_{\text{com}}^{ij} \approx \omega_{\text{tw}}^2 \left(\hat{\sigma}_z^{(i)} + \hat{\sigma}_z^{(j)} \right) / (2N\omega_{\text{com}})$ which shows that for a given $\hat{g}_{\text{com}}^{ij}$ the tweezer intensity should scale linearly with N .

3.2.1 Effective Hamiltonian

The first line of the Hamiltonian 3.3 contains the qubit-state dependence of the phonon modes. This may lead to residual qubit-phonon entanglement at the end of the gate, causing errors. However, straightforward spin-echo sequences correct these errors. The second line contains the qubit-qubit interactions, and the first term dominates for $|\delta| \ll |g^\pm|$. To achieve a geometric phase gate we set the gate time to $\tau = 2\pi/\delta$ and $\gamma^2/\delta^2 = \pi/4$ [68, 89]. To characterize the gate under experimental conditions, we first consider two $^{171}\text{Yb}^+$ ions with trap frequency $\omega_{\text{com}} = 2\pi \times 1 \text{ MHz}$. Next, we consider $N = 4$ ions to demonstrate the scalability of our scheme. We assume that the ions are initialized in a thermal state with \bar{n} motional quanta. The gate sequence consists of four pulses of duration $\tau = 2\pi/\delta$, as illustrated in Fig. 3.2 (a). Each pulse uses adiabatic ramping for the electric field and laser interaction to avoid non-adiabatic coupling of phonon modes. At the end of the first pulse we use π -pulses on both ions to remove the extra phases accumulated due to the last two terms in Eq. 3.3. However, this spin echo pulse does not fully correct for the residual qubit-motion entanglement because $g_m^{i,j}(|11\rangle) + g_m^{i,j}(|00\rangle) \neq g_m^{i,j}(|01\rangle) + g_m^{i,j}(|10\rangle)$. This can be compensated with

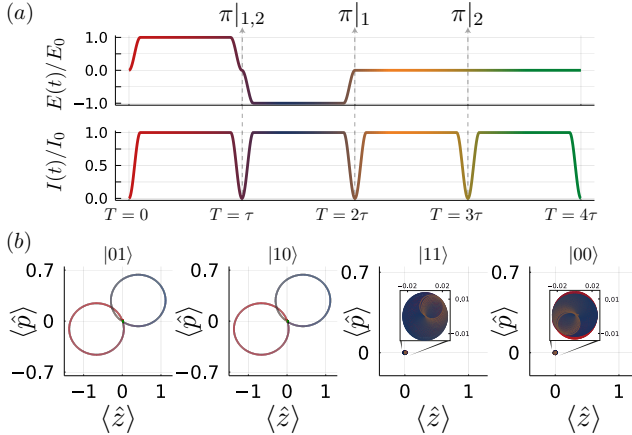


FIGURE 3.2: (a) Pulse sequence used for the simulations, $E(t)/E_0$ and $I(t)/I_0$ are the normalized electric field and laser intensities, respectively. At the end of each of the first three pulses we perform a π -pulse on either ion 1 and 2, 1 or 2. (b) Phase space dynamics for a two-ion crystal in natural units. When the ions are in the state $|01\rangle$ or $|10\rangle$ the electric field makes them oscillate. For the states $|11\rangle$ and $|00\rangle$, the electric field is not resonant with the COM mode. The residual motion of states $|11\rangle$ and $|00\rangle$ is highlighted in the insets. The parameters used are: $\delta = 2\pi \times 0.001$ MHz, $E_0 = 0.269$ mV/m, $\omega_{\text{com}} = 2\pi \times 1$ MHz and $\omega_{\text{tw}} = 2\pi \times 250$ kHz.

one more spin echo pulse on each ion separately. To this end, the 2nd pulse is applied to qubit 1 and the 3rd pulse to qubit 2 or vice versa, with the electric field switched off, see Fig. 3.2 (a).

3.3 GATE FIDELITY AND SCALABILITY

We simulate the gate dynamics generated by Eq. 3.1 and use process fidelity to characterize its performance. For simplicity, we first ignore the contribution of the stretch mode and set ($m = \text{com}$). In Fig. 3.2 (b) we illustrate the gate mechanism using the phase space dynamics for a two-ion crystal of $^{171}\text{Yb}^+$ prepared in the ground state of motion. For the states $|01\rangle$ and $|10\rangle$, $\hat{g}_{\text{com}}^{ij} \approx 0$. Thus, these states follow the displacement generated by the electric field. On the other hand, the other two states $|11\rangle$ and $|00\rangle$ are not significantly displaced in phase space since the COM mode frequency is shifted by the tweezers. The chosen gate parameters ensure that the phases accumulated for these four states correspond to a geometric phase gate.

For ions initialized in a thermal state \bar{n} , the process fidelity is given by [90]:

$$\bar{F}(\hat{U}_{\text{id}}, \hat{U}_{\text{H}}) = \frac{\sum_l \text{tr} [\hat{U}_{\text{id}} \hat{\sigma}_l^\dagger \hat{U}_{\text{id}}^\dagger \hat{\sigma}_l (\hat{U}_{\text{H}})] + d^2}{d^2 (d+1)}, \quad (3.4)$$

where $\hat{\sigma}_l(\hat{U}_{\text{H}}) \equiv \text{tr}_{\text{FS}}[\hat{U}_{\text{H}} [|n\rangle\langle n| \otimes \hat{\sigma}_l] \hat{U}_{\text{H}}^\dagger]$ is the projector on one of the $SU(2)$ d -dimensional representation of Pauli matrices (here $d = 4$ for a two ions case) and on the Fock state $|n\rangle$, \hat{U}_{id} is the ideal phase gate, and \hat{U}_{H} is the unitary generated by the Hamiltonian shown in Eq. 3.1 in the interaction picture. In Fig. 3.3 we show the process fidelity of the proposed gate for $\delta/2\pi = 1$ kHz in the single mode approximation with two different \bar{n} along with a more thorough calculation including the stretch mode. With the single mode approximation, shown in solid blue and dashed orange lines, \bar{F} exceeds 99% at relatively low tweezer strength, $\omega_{\text{tw}}/\omega_{\text{com}} \gtrsim 0.1$. Fidelities higher than 99.9% can be obtained for $\omega_{\text{tw}}/\omega_{\text{com}} \gtrsim 0.21$. Higher tweezers intensity also allow us to perform faster gates at larger detunings while maintaining high fidelities. The green pentagons show \bar{F} including the contribution of the stretch mode and confirm the validity of the single mode approximation. We note that when considering the contribution from both modes, we need to take into account a small correction to the electric field frequency μ . This originates from the perturbation induced by the presence of tweezers on the original eigenmodes of the system. The deviation can be calculated either by perturbation theory (two ions) or by exact diagonalization (four ions) which are shown in the second row of Table. 3.1. We demonstrate the scalability of the scheme by considering four ions in a harmonic potential under the full tweezer Hamiltonian and including all four modes of motion. As discussed above, for each ion pair we correct δ given the COM mode shift. We show that \bar{F} for each ion pair at $\omega_{\text{tw}} = 2\pi \times 254$ kHz, as shown in Tab.3.1, does not degrade compared to the two ion crystal. This demonstrates the scalability of our scheme subject to laser power limitations since the required tweezer intensity $\propto N$. However, since the gate does not require the Lamb-Dicke regime, the needed tweezer power can be limited by lowering ω_{com} considerably. Finally, we study the effect of noise Λ on the tweezer intensity during the four pulses. We consider two scenarios illustrated in Fig. 3.4. In Γ_{DC} , we consider shot-to-shot noise at frequencies $\nu_A \ll 1/\tau$ and find that the spin echo pulses in the gate sequence build in resilience to this type of noise (see Fig. 3.4). The second case is the worst case scenario: noise contribution at the same frequency as the individual laser pules ($\nu_A \sim 1/\tau$). Then the dephasing in each pulse adds up, lowering \bar{F} considerably. For big ion crystals inhomogeneities of the electric field gradient should also be considered. Our simulations indicate that these do not affect the \bar{F} significantly.

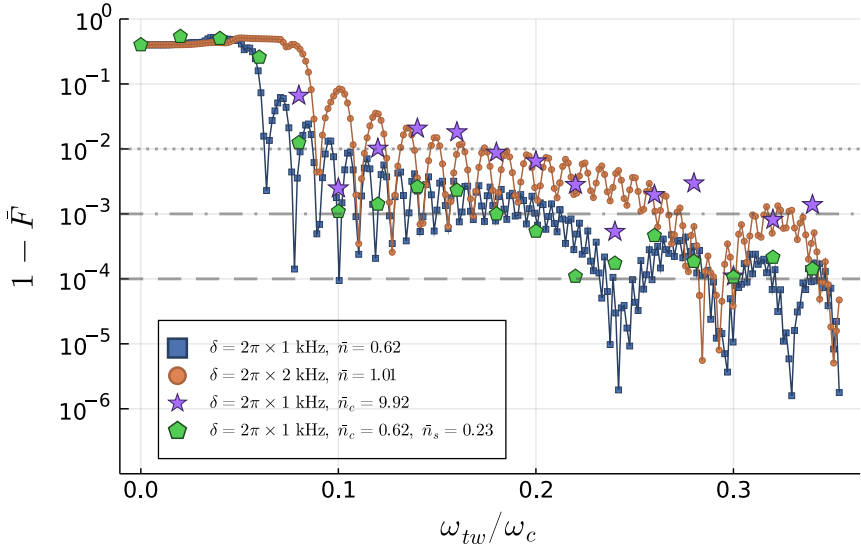


FIGURE 3.3: Process fidelity as a function of tweezers strength for a two ion crystal at different δ and \bar{n} at $\omega_{\text{com}} = 2\pi \times 1 \text{ MHz}$. The resulting gate time is 4τ with $\tau = 2\pi/\delta$. The green pentagons show the fidelity for a two ion crystal taken into account the contribution of both modes. The Fock state cut-off for the thermal state used in the calculations is $n_{\max} = 20$ for the single mode cases with $\bar{n} \leq 1$ and $n_{\max} = 100$ for $\bar{n} \simeq 10$. For the two modes case $n_{c,\max} = 14$ and $n_{s,\max} = 10$, with \bar{n}_c and \bar{n}_s respectively the average phonon number in the COM and stretch mode.

3.4 EXPERIMENTAL CONSIDERATIONS

The tweezer potential takes the form: $\Phi_{|j\rangle}(\mathbf{r}) \propto \alpha_{|j\rangle}(\lambda_{\text{tw}})I(\mathbf{r})$ with $\alpha_{|j\rangle}(\lambda_{\text{tw}})$ the dynamic polarizability at the tweezer wavelength λ_{tw} of qubit state $|j\rangle$ and $I(\mathbf{r})$ the intensity pattern [71]. Expanding a Gaussian intensity pattern with waist $w_0 \gg l_m$ with $l_m = (2M\omega_m)^{-1/2}$ we obtain $\Phi_{|j\rangle}(z) \approx \Phi_{|j\rangle}(0) + M\omega_{|j\rangle}^2 z^2/2$, with $\omega_{|j\rangle}^2 = -4\Phi_{|j\rangle}(0)/(Mw_0^2)$ [71]. Here, we assumed that the tweezer has the largest curvature in the z -direction, and disregard the other directions.

We must identify qubit states with opposite dynamical polarizabilities such that $\omega_{|1\rangle}^2 = -\omega_{|0\rangle}^2$. Qubits encoded in the ground $S_{1/2}$ and metastable $D_{5/2}$ states of Ca^+ , Sr^+ or Ba^+ fulfill this condition. The differential polarizabilities

Pair	$\textcircled{1}\textcircled{2} \circ \circ$	$\textcircled{1} \circ \textcircled{3} \circ$	$\textcircled{1} \circ \circ \textcircled{4}$	$\circ \textcircled{2}\textcircled{3} \circ$
$(1 - F)10^4$	3.7	4.7	2.4	1.1
$(\omega_{\text{com}} - \mu)$ [kHz]	1.212	1.325	1.488	1.162

TABLE 3.1: Fidelities and detunings for all combinations of pairs in a four ion chain. All modes are in the ground state of motion, $\omega_{\text{tw}} = 2\pi \times 257$ kHz and $\omega_{\text{com}} = 2\pi \times 1$ MHz.

of these states can be tuned over a wide range by choosing the tweezer wavelength and Zeeman substate m_j of the $D_{5/2}$ manifold [91]. Furthermore, it is beneficial to have no residual differential Stark shift at the center of the tweezer as this may lead to dephasing of the qubits in case of laser intensity fluctuations. The spin echo sequence will eliminate shot-to-shot variations, but not fluctuations within a single implementation. Vanishing differential Stark shift in the center of the tweezer can be straightforwardly obtained using non-Gaussian hollow tweezers [53, 92]. Another solution is to use bichromatic tweezers with wavelengths $\lambda_{\text{tw}}^{(1)}$ and $\lambda_{\text{tw}}^{(2)}$ and beamwaists w_1 and w_2 . We then require that in the center of the tweezer ($z = 0$): $\Phi_{|0\rangle}^{(1)} + \Phi_{|0\rangle}^{(2)} = \Phi_{|1\rangle}^{(1)} + \Phi_{|1\rangle}^{(2)}$ and $\Phi_{|0\rangle}^{(1)}/w_1^2 + \Phi_{|0\rangle}^{(2)}/w_2^2 = -\Phi_{|1\rangle}^{(1)}/w_1^2 - \Phi_{|1\rangle}^{(2)}/w_2^2$. In the experimentally convenient limit where $w_1 \ll w_2$, this reduces to: $\Phi_{|0\rangle}^{(1)} = -\Phi_{|1\rangle}^{(1)}$ and $\Phi_{|0\rangle}^{(2)} - \Phi_{|1\rangle}^{(2)} = 2\Phi_{|1\rangle}^{(1)}$. Note that the frequency sum and difference should not be close to any transition as this will lead to additional Stark shifts or photon scattering.

As a practical example, we consider the qubit states $|0\rangle = |S_{1/2}, m_j = 1/2\rangle$ and $|1\rangle = |D_{5/2}, m_j = 3/2\rangle$ in ${}^{40}\text{Ca}^+$ [93]. We obtain $\Phi_{|0\rangle}^{(1)} = -\Phi_{|1\rangle}^{(1)}$ at around $\lambda_1 = 770$ nm [91]. The second requirement can be met by setting $\lambda_2 \approx 900$ nm. The relative close proximity of the $D_{5/2} \rightarrow P_{3/2}$ transition at 854 nm causes photon scattering Γ_{sc} which limits the attainable coupling strength. We estimate $\Gamma_{\text{sc}} = \Phi_{|j\rangle}^{(i)} \Gamma_{\text{tr}} / \Delta_{|j\rangle, \xi}^{(i)}$ for each transition ξ , state $|j\rangle$ and tweezer i with Γ_ξ the transition linewidth and $\Delta_{|j\rangle, \xi}^{(i)}$ the frequency detuning. Demanding $\Gamma_{\text{sc}}/2\pi \lesssim 1 \text{ s}^{-1}$, we find $|\Phi_{|j\rangle}^{(i)}| \lesssim 20$ MHz for all i and $|j\rangle$. This results in $|\omega_{\text{tw}}| \lesssim 2\pi \times 70$ kHz for $w_2 \gg w_1 = 1 \mu\text{m}$.

It is also possible to use qubits that are encoded in the ground $S_{1/2}$ hyperfine or Zeeman states of the ions. Here, circularly polarized tweezers may be used to obtain large differential Stark shifts. However, this approach precludes the use of magnetic field insensitive qubits [71, 94]. One solution is to make use of quadrupole transitions [95, 96]. These have coupling strengths that are typically $\sim 2\pi a_0/\lambda \sim 10^{-3} - 10^{-4}$ times smaller than for dipole allowed

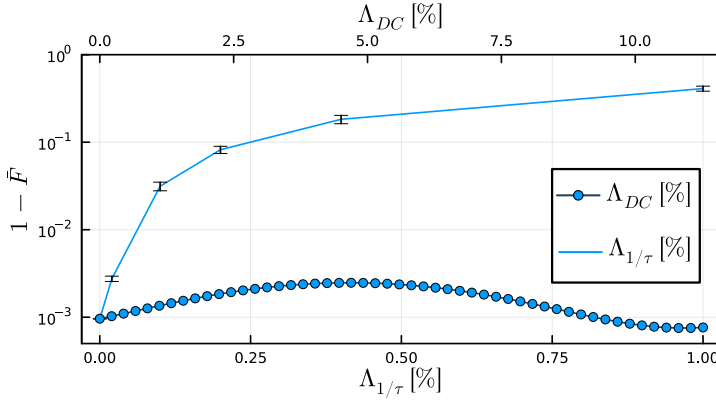


FIGURE 3.4: Effect on noise Λ on the tweezer laser intensity at frequencies $\nu_A = 1/\tau$ and shot-to-shot noise ($\nu_A = 0$) for $\omega_{tw} \sim 2\pi \times 180$ kHz, $\delta = 2\pi \times 1$ kHz and $\omega_c = 2\pi \times 1$ MHz. The points at $\nu_A = 1/\tau$ are taken assuming a random gaussian noise for each of the four gate pulses with a standard deviation $\sigma = \Lambda_{1/\tau}$. The points at $\nu_A = 0$ assume a change in the tweezer intensity Λ_{DC} for times longer than the gate time τ .

transitions, with a_0 the Bohr radius, but have highly suppressed photon scattering rates even at small detunings. Tuning the tweezer wavelength far away from all dipole-allowed transitions, the differential Stark shift originates from the quadrupole transitions alone [71, 94, 95]. In case only a single transition k' obeys $\Delta_{k'} \ll \omega_0$, with ω_0 the frequency difference between the qubit states and $\Delta_{k'}$ the detuning, we can make a two-level approximation for the transition $|0\rangle \rightarrow |k'\rangle$ and obtain: $\Phi_{|0\rangle} \approx \nu_{\text{Dipole}} + \Omega_{k'}^2/(4\Delta_{k'})$ while $\Phi_{|1\rangle} \approx \nu_{\text{Dipole}}$ with $\Omega_{k'}$ the Rabi frequency. Approximating the Stark shift due to the dipole transitions to arise mainly from a single (effective) transition, $\nu_{\text{Dipole}} = \Omega_{\text{Dipole}}^2/(4\Delta_{\text{Dipole}})$, we get $\Omega_{k'}^2/(4\Delta_{k'}) = -\nu_{\text{Dipole}}$ if we set $\Delta_{k'} = -\epsilon^2 \Delta_{\text{Dipole}}$ with $\Omega_{k'} = \epsilon \times \Omega_{\text{Dipole}}$. The detuning Δ_{Dipole} can be estimated as the frequency difference between the quadrupole transition and the strong D1 and D2 transitions and lies typically in the 100-THz range [97]. Therefore, we require $\Delta_{k'} \sim 1 - 100$ MHz for $\epsilon = 10^{-3} - 10^{-4}$. Since we require in addition $\Delta_{k'} < \Omega_{k'}$ to avoid driving the transition, we get differential Stark shifts of $\sim 0.1 - 10$ MHz and $\omega_{tw} \sim 2\pi(30 - 300)/\sqrt{M_u}$ kHz, with M_u the mass of the ion in atomic mass units and $w_0 = 1\ \mu\text{m}$. By comparison, switching to a Laguerre-Gaussian mode with radial index $p = 1$, the Rabi frequency in the center of the tweezer vanishes, whereas ω_{tw} remains unaltered for the

same w_0 . In this situation, we only require $\Delta_{k'} < \Omega_{k'}(z_{\max})$, with z_{\max} the maximum amplitude of motion of the ions during the gate. For the presented calculations $z_{\max} \sim 10 \text{ nm} \ll w_0$ such that ω_{tw} can be significantly larger than for Gaussian tweezers.

3.5 CONCLUSIONS

We have proposed and analysed a new architecture for performing quantum computation with trapped ions that uses optical tweezers and oscillating electric fields. The infrastructural simplicity of our scheme makes it attractive, while the ability to individually address the ions by the tweezer makes it universal. Furthermore, our proposal does not rely on the Lamb-Dicke approximation and is independent of the qubit separation. Residual qubit-phonon entanglement that may lead to decoherence is prevented by a spin-echo sequence. Taking experimental considerations into account, the scheme can be performed on optical qubits and on ground state qubits. Here, either circularly polarized or hollow tweezers such as those derived from e.g. Laguerre-Gaussian modes [53, 92] could be used. The challenge will be to supply sufficient curvature to such tweezers while maintaining excellent control. For this active stabilization of the power and direction of the tweezers may be required. Finally, it seems feasible to consider a fast gate version of the proposed gate, in analogy to Ref. [98] where electric field pulses are combined with Rydberg excitation of the trapped ions in order to implement quantum logic gates.

4

M A G N U S Q U A N T U M G A T E

Based on
arXiv:2301.04668 (2023)

In this chapter we propose a novel way of engineering two-qubits gates on trapped ions based on the optical Magnus effect. We consider the implementation of quantum logic gates in trapped ions using tightly focused optical tweezers. Strong polarization gradients near the tweezer focus lead to qubit-state dependent forces on the ion. We show that these may be used to implement quantum logic gates on pairs of ion qubits in a crystal. The qubit-state dependent forces generated by this effect live on the plane perpendicular to the direction of propagation of the laser beams opening new ways of coupling to motional modes of an ion crystal. The proposed gate does not require ground state cooling of the ions although the waist of the tightly focused beam needs to be comparable with its wavelength in order to achieve the needed field curvature. Furthermore, the gate can be performed on both ground state and magnetic field insensitive clock state qubits without the need for counter-propagating laser fields. This simplifies the setup and eliminates errors due to phase instabilities between the gate laser beams. Finally, we show that imperfections in the gate execution, in particular a 30 nm tweezer alignment error leads to an infidelity of $\sim 10^{-3}$. In the absence of experimental imperfections and within the limits of the gate model explored in this work the fidelity is predicted to be ~ 0.99988 when using a Laguerre-Gaussian beam to suppress photon scattering errors.

4.1 THE MAGNUS EFFECT FOR ENGINEERING A TWO-QUBIT GATE

Trapped ions are one of the most mature platforms for the implementation of quantum computing and quantum logic gates have been implemented with very high fidelity in these systems [83, 84]. Usually, the quantum logic gates in trapped ions rely on state-dependent forces applied to the ions by laser fields or magnetic fields. The exchange of motional quanta between the ions then leads to effective qubit-qubit interactions. Several recent works have explored how the use of state-of-the-art optical tweezer technology can benefit the trapped ion quantum computer. Optical tweezers can be used to confine atoms very strongly by inducing a dipole in them and find application in

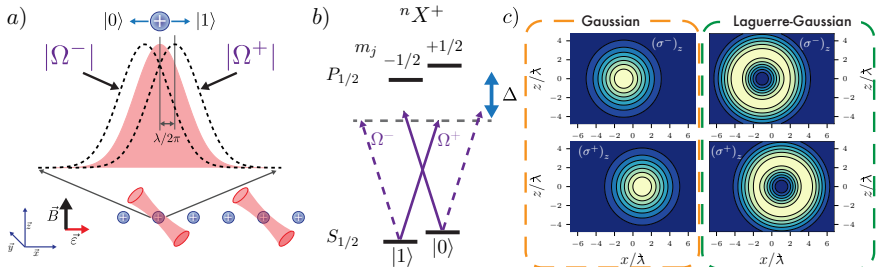


FIGURE 4.1: Schematic representation of the two-qubit gate. a) We apply tweezers propagating along the $-y$ direction on the two ions forming the gate. The tweezer intensity can be decomposed into three polarization components. b) Simplified level scheme of an alkaline-earth like ion without nuclear spin showing the encoding of the qubit in its Zeeman ground states. The two polarization components of the tweezer couple to different states in the $P_{1/2}$ manifold with detuning Δ . This causes the minima of the tweezer potentials to be shifted by an amount $\pm\lambda$ depending on the qubit state. c) Main polarization components for a Gaussian and Laguerre-Gaussian ($l = 1, n = 0$) tightly focused tweezer.

neutral atomic quantum simulators, in which tweezers are used to levitate individual atoms [24–26, 99, 100]. In trapped ions, tweezers may be used to tune the soundwave spectrum in the ion crystal and thereby to program the interactions between the qubits [45, 51, 86]. Furthermore, in a recent work [101] we have proposed combining state-dependent optical tweezers with oscillating electric fields to build a universal trapped ion quantum computer with extremely long-ranged interactions between the qubits.

In this work, we consider another scenario, in which we make use of the strong polarization gradients that occur in optical tweezers. We note that strong gradients in optical potentials have been previously investigated to implement two-qubit gates without the need for ground-state cooling [102–104]. However, our approach utilizes the state-dependent displacement of the tweezer potential due to polarization gradients [52, 105, 106]. We propose to use this optical analogue of the Magnus effect to implement quantum logic gates in trapped ions [52].

4.2 SETUP

We consider linearly x -polarized, Gaussian tweezers, pointing in the $-y$ direction and tightly focused at two qubits between which we wish to implement

a quantum logic gate. The quantum computing platform here considered is a linear crystal of N alkali-like trapped ions of mass m . In the focal plane the ions experience a strong polarization gradient along the x direction, such that the polarization is linear (x) in the center and circular (σ^\pm_z) in the wings of the Gaussian. A direct calculation (see Section 4.3.1) decomposing the field in the focal plane into its circular components (σ^\pm_z) (and π_z) shows that, to a good approximation, the circular components are near-Gaussian distributions, displaced in opposite directions along the x axis. We depict this setup in Fig. 4.1. Note that the circular components rotate in the xy plane, i.e. a plane containing the \mathbf{k} vector of the light. As shown in Fig. 4.1, the (σ^\pm_z) component is displaced by an amount $\pm\lambda \equiv \pm\lambda/2\pi$, with λ the tweezer wavelength. As the total field is the superposition of two displaced Gaussians, its intensity is slightly elongated along x . Hollow tweezers (Gaussian-Laguerre) can be used instead of Gaussian ones. This will provide the needed field curvature while keeping near-zero intensity at the center of the beam, drastically reducing the probability of off-resonant scattering that might limit the gate fidelity.

For simplicity, we first consider ions without nuclear spin, such as $^{40}\text{Ca}^+$, $^{88}\text{Sr}^+$, $^{138}\text{Ba}^+$ and $^{174}\text{Yb}^+$. The qubits are encoded in the electronic ground states $^2S_{1/2}$ and $|0\rangle = |j = 1/2, m_j = 1/2\rangle$ and $|1\rangle = |j = 1/2, m_j = -1/2\rangle$ with j the total electronic angular momentum and m_j its projection on the quantization axis. The magnetic field lies along the z -direction and the tweezers are polarized along the x -direction, such that the ions experience linearly polarized laser light. The direction along the x -axis is the long direction of the ion trap, with trap frequency ω_x . The motion of the ions along the x -direction can be described by collective modes of harmonic motion with frequencies ω_m and mode vectors $b_{i,m}$, with m labeling the mode and i the ion [87].

We choose the detuning between the tweezers and the D1 transition to be large enough to avoid photon scattering, but much smaller than the spin-orbit coupling splitting of the 2P state. In this way, we can neglect coupling to the $P_{3/2}$ state. In what follows we will show that this requirement can be satisfied experimentally. Close to the center of the tweezer, strong polarization gradients appear and as a result, the two qubit states experience slightly different tweezer potentials. In particular, as we show in Fig. 4.1(a), the optical Magnus effect causes each qubit state to experience a tweezer potential that is offset from the apparent center of the tweezer by $\sim\lambda$ [52]. Hence, we may approximate the tweezer potential as :

$$\hat{U}(x) = -U_0 \exp(-2(\hat{x} + \hat{\sigma}_z \lambda)^2/w_0^2) \quad (4.1)$$

$$\approx -\tilde{U}_0 + \frac{1}{2}m\omega_{\text{tw}}^2\hat{x}^2 + gx\hat{\sigma}_z \quad (4.2)$$

with $\omega_{\text{tw}} = \sqrt{4\tilde{U}_0(w_0^2 - 4\lambda^2)/(mw_0^4)}$, $g = 4\tilde{U}_0\lambda/w_0^2$, and $\tilde{U}_0 = U_0 \exp(-2\lambda^2/w_0^2) \approx U_0$. Here U_0 is the tweezer potential in the center and the beam waist is w_0 . Our approximation replaces the tweezer potential with a harmonic potential and is valid for $w_0 \gg l_m$, with $l_m = \sqrt{\hbar/2m\omega_m}$. The last term in $U(x)$ is the result of the spin-dependent force g coupling the internal state of the qubit, $\hat{\sigma}_z$, to its motion \hat{x} . Thus, the optical Magnus effect allows us to straightforwardly implement a quantum gate.

4.3 TWEEZER HAMILTONIAN

In the interaction picture with respect to $\hat{H}_0 = \hbar\omega_m \hat{a}_m^\dagger \hat{a}_m$ the tweezer Hamiltonian on ions i and j is:

$$\hat{H}_1 = A(t) \left(\frac{1}{2} m \omega_{\text{tw}}^2 (\hat{x}_i^2 + \hat{x}_j^2) + g \left(\hat{\sigma}_z^{(i)} \hat{x}_i + \hat{\sigma}_z^{(j)} \hat{x}_j \right) \right). \quad (4.3)$$

Here, $\hat{x}_i = \sum_m l_m b_{im} (\hat{a}_m e^{-i\omega_m t} + \hat{a}_m^\dagger e^{i\omega_m t})$ is the position operator of ion i in the interaction picture, with \hat{a}_m^\dagger the creation operator for the mode m , and $0 \leq A(t) \leq 1$ specifies the time-dependence of the tweezer intensity. The qubit-state independent terms in \hat{H}_1 do not alter the dynamics of the quantum gate. We ignore these terms and arrive at:

$$\hat{H}_2 = A(t) g \left(\hat{x}_i \hat{\sigma}_z^{(i)} + \hat{x}_j \hat{\sigma}_z^{(j)} \right), \quad (4.4)$$

which takes the form of a spin-phonon coupling Hamiltonian reminiscent of the Mølmer-Sørensen scheme for phonon-mediated quantum gates in trapped ions [107]. However, at this stage we still have various choices available for $A(t)$, depending on which type of quantum gate we would like to implement. For instance, pulsed $A(t)$ could be used to perform fast gates. Here, we choose $A(t)$ to obtain a geometric phase gate. For this, we set $2A(t) = 1 - \cos(\nu t + \phi)$ where $\phi = 0$ assures a smooth ramp of the tweezer intensity and $\nu = \omega_c + \delta$ with the subscript c denoting the center-of-mass (c.o.m.) mode for which $\omega_c = \omega_x$ and $b_{i,c} = 1/\sqrt{N}$. We write the operators \hat{x}_i and \hat{x}_j in terms of \hat{a}_c and \hat{a}_c^\dagger and perform the rotating wave approximation to arrive at:

$$\hat{H}_3 = \frac{gl_c}{4\sqrt{N}} (\hat{a}_c e^{i\delta t} + \hat{a}_c^\dagger e^{-i\delta t}) \left(\hat{\sigma}_z^{(i)} + \hat{\sigma}_z^{(j)} \right). \quad (4.5)$$

To derive the qubit-qubit interactions forming the geometric phase gate, we perform a unitary transformation $\hat{U}_1 = e^{-i\delta\hat{a}_c^\dagger\hat{a}_c t}$ to eliminate the time depen-

dence, followed by a Lang-Firsov [88] transformation, $\hat{U}_2 = \exp(\hat{\alpha}(\hat{a}_c^\dagger - \hat{a}_c))$ with $\hat{\alpha} = -\frac{\tilde{g}}{\delta} (\hat{\sigma}_z^{(i)} + \hat{\sigma}_z^{(j)})$. Disregarding qubit-independent terms, we obtain

$$H_{\text{eff}} = \frac{2\tilde{g}^2}{\hbar\delta} \hat{\sigma}_z^{(i)} \hat{\sigma}_z^{(j)}, \quad (4.6)$$

with $\tilde{g} = gl_c/(4\sqrt{N}) = \tilde{\eta}\tilde{U}_0$, with the proportionality factor $\tilde{\eta} = \lambda l_c/(\sqrt{N}w_0^2)$. This Hamiltonian generates qubit-qubit interactions that can be used to implement a geometric phase gate by setting the gate time $\tau = 2\pi/\delta$ and $\frac{\tilde{g}^2\tau}{\hbar^2\delta} = \pi/4$.

4.3.1 Optical Magnus effect

A key characteristic of a tightly focused beam is the strong field curvature near the focus. This not only affects the local intensity but also its polarization structure. To calculate this, we take a superposition of plane waves labeled by their wave vector in spherical coordinates, $\mathbf{k} = (k, \theta, \phi)$. Taking $k = \omega/c$ as fixed we write

$$\mathbf{E}(\mathbf{r}) \propto \int_0^{2\pi} d\phi \int_0^\pi d\theta \sin \theta \mathbf{u}_x(\theta, \phi) a(\theta, \phi) e^{i\mathbf{k} \cdot \mathbf{r}}$$

with $\mathbf{u}_x(\theta, \phi)$ a polarization vector obtained by co-rotating the \mathbf{x} unit vector when \mathbf{k} is rotated from \mathbf{z} to (θ, ϕ) , such that $\mathbf{u}_x(\theta, \phi) \cdot \mathbf{k} = 0$, see also Ref. [52]. In the calculation we center the beam around $\theta = 0$, and the focal plane is given by $\mathbf{r} = (x, y, 0)$. The shape of the beam is determined by the amplitude function $a(\theta, \phi)$. For a Gaussian beam we set $a(\theta, \phi) = \exp(-\theta^2/w_\theta^2)$; for the lowest order ($l = 1$) Laguerre-Gaussian (LG) beam we set $a(\theta, \phi) = \theta \exp(i\phi - \theta^2/w_\theta^2)$. After performing the above integral we rotate the results for tweezers propagating along the $-y$ direction. Finally, the circular field components σ^\pm shown in Fig. 1 of the main text are obtained as the projection onto unit vectors $(\mathbf{x} \pm i\mathbf{y})/\sqrt{2}$. In Fig. 4.2, all three polarization components for a Laguerre-Gaussian beam are shown. Note that the σ^- and σ^+ components have similar intensity while the π -polarization is suppressed by a factor ~ 100 .

4.4 CHARACTERIZATION OF THE GATE

We analyse the gate dynamics by performing numerical simulation of the full dynamics generated by the Hamiltonian $\hat{H}_{\text{sim}} = \hat{H}_0 + \hat{U}(x_i) + \hat{U}(x_j)$ for a two dimensional ion crystal where the tweezers potentials $\hat{U}(x_{i;j})$ on ions

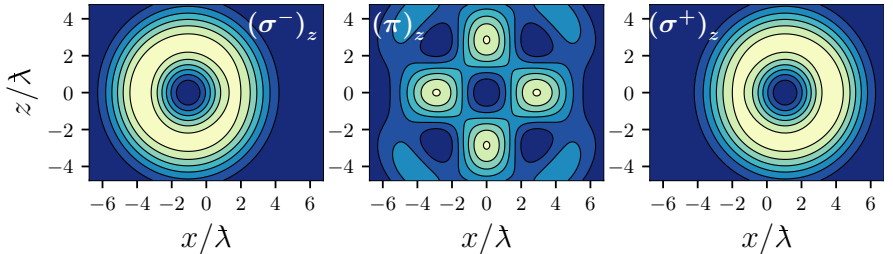


FIGURE 4.2: Intensity of the polarization components for a LG beam calculated at the focus. The π -polarization component has been enhanced by a factor 100 to make it visible. Here we set $w_0 = 0.6$

i and j have been expanded up to fourth-order including spin-independent terms. We use realistic experimental parameters: $\sim 450 \mu\text{W}$ of tweezer laser power focused to a waist of $w_0 \sim 0.5 \mu\text{m}$ and tuned 22 THz to the red from the ${}^2S_{1/2} \rightarrow {}^2P_{1/2}$ transition in ${}^{174}\text{Yb}^+$ ($\lambda = 369.5 \text{ nm}$). This results in $\tilde{U}_0/h \sim 1.6 \text{ MHz}$, $\tilde{g}/h = 2.1 \text{ kHz}/\sqrt{N}$, and setting $\delta = 2\pi \times 12.2 \text{ kHz}/\sqrt{N}$ the gate time for the geometric phase gate is $\tau = 170\sqrt{N}\mu\text{s}$. With a calculated qubit-state independent tweezer potential of $\omega_{\text{tw}} \sim 2\pi \times 37 \text{ kHz}$, the center-of-mass mode frequency ($\omega_c/2\pi \sim 1 \text{ MHz}$) is shifted by $\sim 2\omega_{\text{tw}}^2/\omega_c N \sim 2\pi \times 710/N \text{ Hz}$. This shift can easily be taken into account by correcting δ accordingly. In these estimates, we neglected the contribution from other dipole allowed transitions, that are detuned by $\sim 66 \text{ THz}$ (the relatively weak ${}^2S_{1/2} \rightarrow {}^3[3/2]_{3/2}$ transition) and 115 THz (the strong D2 line) or more.

We consider the gate unitary with a spin-echo sequence given by $U(0, \tau) = X^{\otimes 2}U(\tau/2, \tau)X^{\otimes 2}U(0, \tau/2)$, where $X^{\otimes 2}$ is a qubit flip on both qubits. This spin echo sequence is needed in order to remove local rotations on the qubits states and possible timing errors. We calculate the unitary time evolution operator $U(0, \tau)$ for a system of two ions with their motional c.o.m. and stretch modes and truncate their respective Hilbert spaces to $n_c \leq 18$ and $n_s \leq 10$. In figure 4.3 we show the process fidelity of the gate assuming the ions are in their motional ground state ($\bar{n} = 0$) as a function of gate time.

The gate fidelity of $\mathcal{F} = 0.999988$ with $n_c = n_s = 0$ rivals the current standard approaches. Moreover, the performance of our gate is robust to the thermal occupation of the motional modes. We characterize the gate performance in presence of thermal phonons using the average gate fidelity [90] and find that it depends weakly on the motional state of the two ions. In fact, using $\bar{n}_c = 0.62$, $\bar{n}_s = 0.23$, the fidelity is almost unaltered at $\mathcal{F}_{\text{th}} = 0.999989$.

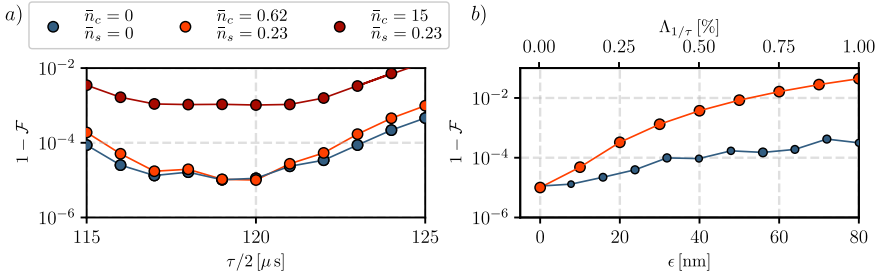


FIGURE 4.3: Calculated infidelities based on numerical simulations of the full Hamiltonian \hat{H}_{sim} , neglecting errors due to photon scattering (see Tab. 4.1). We report the infidelity for ground state cooled ions $\bar{n}_c, \bar{n}_s = 0$ (blue), sub-Doppler cooled thermal state with $\bar{n}_c = 0.62, \bar{n}_s = 0.23$ (orange) and $\bar{n}_c = 15, \bar{n}_s = 0.23$ (red, using in this case a Fock cutoff $n_c \leq 120, n_s \leq 10$). (a) Process infidelity of the two-qubit Magnus gate for different gate times. (b) Effects of misalignment ϵ (orange) and intensity noise $A_{1/\tau}$ (blue) on the gate fidelity. The size of each intensity noise data point represents the standard deviation of 20 simulation where we generated a random Gaussian noise with $\sigma = A_{1/\tau}$ on each of the two pulses. This implies a noise on the laser intensity at frequency $1/\tau$ that can not be removed by the spin-echo sequence.

In Tab. 4.1 we report the main sources of gate's infidelities. One of main experimental challenges is perfect tweezer alignment. We have studied the resilience of the gate against misalignment of the tweezer in the x -direction, which we denote by ϵ . In the presence of misalignment, $\tilde{U}_0 \rightarrow U_0 \exp^{-2(\epsilon + \delta_z \lambda)^2 / \omega_0^2}$. Thus, the misalignment has two effects: (i) it changes the tweezer potential at the center of the tweezer and therefore the phase accumulation in the phase gate, and (ii) it shifts the potential in a qubit-state-dependent way. The second contribution is corrected to lowest order by a spin-echo sequence. Figure 4.3(b) shows the infidelity as a function of ϵ . Here we assume that the tweezers are misaligned on both ions in the same way which seems the experimentally most likely case. The unitary $U(0, \tau)$ leads to phase space trajectories for $\langle x(t) \rangle$ and $\langle p_x(t) \rangle$ associated with the c.o.m. motion (see Section 4.4.1). As expected, we find approximately circular phase-space orbits for the even parity states $|00\rangle, |11\rangle$, and very little motion for the odd parity ones. We see that every state combination leads to ion motion, but the difference in motion still leads to a high fidelity of $\gtrsim 0.999$ as shown in Figure 4.3(b). For the quoted experimental parameters the fidelity is limited by the scattering rate to 0.99988 when using Laguerre-Gaussian

Error source	γ_{ph}	γ_{ph}	ϵ	$A_{1/\tau}$	$\Delta\tau$
	Gaussian	Laguerre-Gaussian	30 nm	0.5%	$\pm 5 \mu\text{s}$
$1 - \mathcal{F}$	2.4×10^{-3}	1.2×10^{-4}	1.3×10^{-3}	9.3×10^{-5}	2.7×10^{-4}

TABLE 4.1: Main sources of gate errors. We estimate γ_{ph} as the probability of off-resonant scattering in for $^{174}\text{Yb}^+$ during the gate time ($\tau = 240 \mu\text{s}$) for a Gaussian and Laguerre-Gaussian beams. Other typical sources of errors are misalignment (ϵ), tweezer intensity noise ($A_{1/\tau}$) and timing ($\Delta\tau$). The values here reported are for laser parameters used in our numerical simulations.

beams. Note however, that this limit can be further reduced by increasing the detuning at the expenses of the required laser power.

4.4.1 Phase-space dynamics

We study the phase-space dynamics of the ions by simulating the time dependent Hamiltonian using trotterization with time-steps of $10^{-4} \tau$. At each time-step we evaluate the expectation value of the $\langle \hat{x} \rangle$ and $\langle \hat{p} \rangle$ for the center of mass mode. As expected, we find approximately circular phase-space orbits for the even parity states $|00\rangle$, $|11\rangle$, and very little motion for the odd parity ones. In Fig. 4.4 it is possible to see the evolution in phase-space for all the four spin states in case of perfectly aligned and slightly misaligned tweezers. As described in the main text we simulate numerically the full Hamiltonian defined as $\hat{H}_{\text{sim}} = \hat{H}_0 + \hat{U}(x_i) + \hat{U}(x_j)$ where in case of misalignment ϵ , $\hat{U}(x)$ reads as :

$$\begin{aligned}
U(x) &\approx -U_0 e^{-2((\hat{x}-\hat{\epsilon})+\hat{\sigma}_z \lambda)^2/w_0^2} \\
&\approx -\tilde{U}_0 + 4\tilde{U}_0 \frac{\hat{\sigma}_z \lambda - \hat{\epsilon}}{w_0^2} \hat{x} \\
&+ \frac{1}{2}\tilde{U}_0 \left(\frac{4(w_0^2 - 4\lambda^2)}{w_0^4} \right) \hat{x}^2 - \frac{1}{2}\tilde{U}_0 \left(\frac{16(\hat{\epsilon}^2 - 2\hat{\sigma}_z \hat{\epsilon} \lambda)}{w_0^4} \right) \hat{x}^2 \\
&- \left(8\tilde{U}_0 \hat{\sigma}_z \lambda \frac{3w_0^2 - 4(3\hat{\epsilon}^2 + \lambda^2)}{3w_0^6} \right) \hat{x}^3 \\
&+ \left(8\tilde{U}_0 \hat{\epsilon} \frac{3w_0^2 - 4(\hat{\epsilon}^2 + 3\lambda^2)}{3w_0^6} \right) \hat{x}^3 \\
&- \left(2\tilde{U}_0 \hat{\sigma}_z \lambda \hat{\epsilon} \frac{-48w_0^2 + 64(\hat{\epsilon}^2 + \lambda^2)}{3w_0^8} \right) \hat{x}^4 \\
&+ \left(2\tilde{U}_0 \frac{3w_0^4 - 24w_0^2(\hat{\epsilon}^2 + \lambda^2) + 16(\hat{\epsilon}^4 + 6\hat{\epsilon}^2\lambda^2 + \lambda^4)}{3w_0^8} \right) \hat{x}^4.
\end{aligned}$$

with

$$\tilde{U}_0 = U_0 e^{-2(\hat{\epsilon} + \hat{\sigma}_z \lambda)^2/w_0^2}$$

A small tweezer misalignment ϵ gives rise to new spin-dependent terms in the Hamiltonian that shift the trapping potential in a state dependent way. In Fig. 4.4 is shown how the dynamics is affected in the case where the tweezers are misaligned by 30 nm.

4.5 CLOCK STATE CASE

While the calculation was performed for the electron spin qubit states in $^{174}\text{Yb}^+$, it should also be possible to use the hyperfine clock states $|F = m_F = 0\rangle$ and $|F = 1, m_F = 0\rangle$ in $^{171}\text{Yb}^+$. This qubit is insensitive to magnetic field noise and coherence times of up to an hour have been measured [60]. In this case, the tweezers are formed by a bichromatic co-propagating laser field detuned by Δ from the D1 transition at 369.5 nm with overall detuning $\Delta \ll \omega_{\text{FS}}$, the fine structure splitting. We set the frequency difference in the bichromatic tweezer to 12.6 GHz, corresponding to the transition between the qubit states [108]. The tweezer laser then causes Raman coupling between the qubit states via two distinct paths. In the first path, the qubits are coupled via the state $|P_{1/2}, F = 1, m_F = -1\rangle$ due to

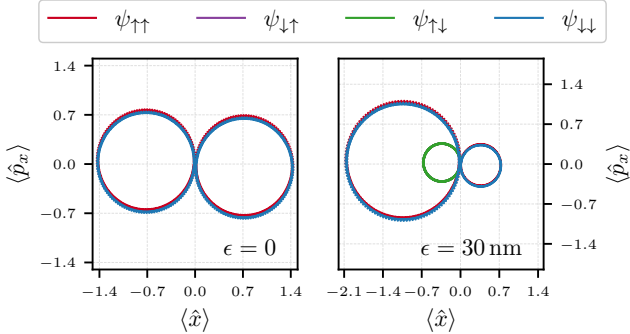


FIGURE 4.4: Center of mass mode phase-space dynamics for perfectly aligned tweezer (left) and for 30 nm misaligned ones (right). For the simulation we used the same parameters as for $\tau/2 = 120 \mu\text{s}$ point in Figure 1(a) of the main text.

the σ^- polarization component in the tweezer. In the other, the qubits are coupled via the state $|P_{1/2}, F = 1, m_F = +1\rangle$ due to the σ^+ component in the tweezer. We denote the Rabi frequencies of each path as $\Omega_{1,2}^\pm(x)$. The corresponding Raman couplings of each path interfere destructively in the center of the tweezer due to a relative minus sign between $\Omega_1^+(x)$ and $\Omega_2^+(x)$ in their Clebsch-Gordan coefficient, $\propto (\Omega_1^-(0)\Omega_2^-(0) + \Omega_1^+(0)\Omega_2^+(0))/\Delta = 0$. However, the Magnus effect causes a strong position dependence of the relative strength of both paths of magnitude

$$\Omega_{\text{eff}}(x) = \frac{\Omega_1^-(x)\Omega_2^-(x)}{\Delta} + \frac{\Omega_1^+(x)\Omega_2^+(x)}{\Delta} \approx \frac{\Omega^2}{\Delta} \frac{4\lambda x}{w_0^2}, \quad (4.7)$$

where we assumed $x \ll \lambda \ll w_0$ and $|\Omega_i^\pm(0)| = \Omega/\sqrt{2}$ with $i = 1, 2$, such that both laser frequencies have the same power. As a result, a qubit state-dependent force appears as in Eq. (4.4), except that we must now replace $\hat{\sigma}_z^{(i,j)} \rightarrow \hat{\sigma}_x^{(i,j)}$ and the gate takes the form of the usual Mølmer-Sørensen interaction $\propto \hat{\sigma}_x^{(i)}\hat{\sigma}_x^{(j)}$ [107]. Amplitude modulation via $A(t)$ allows again for resonant enhancement of the gate.

In addition to the Raman coupling, we obtain a tweezer potential (AC Stark shift) for each qubit state of magnitude

$$\delta_{\text{AC}}^{|k\rangle}(x) = \sum_{i=1,2} \sum_{j=+, -} \frac{|\Omega_i^j(x)|^2}{\Delta_{i,|k\rangle}} \quad (4.8)$$

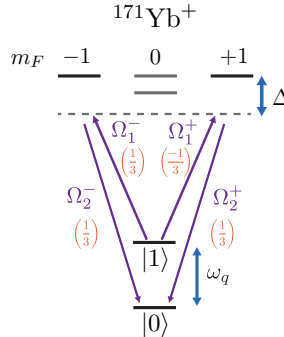


FIGURE 4.5: Relevant energy levels of $^{171}\text{Yb}^+$ for implementing the gate on hyperfine qubit splitted by ω_q . The coupling can be achieved using a pair of Raman beams detuned from the upper state $^2\text{P}_{1/2}$ by Δ . In the brackets are the angular contributions to the various dipole transition elements.

with $\Delta_{1,|0\rangle} = \Delta - \omega_q$, $\Delta_{2,|0\rangle} = \Delta$, $\Delta_{1,|1\rangle} = \Delta$ and $\Delta_{2,|1\rangle} = \Delta + \omega_q$. This causes an additional trapping potential $\Phi(x) \approx \frac{1}{2}m\omega_{\text{tw}}^2x^2$ that is independent of the qubit state as before, as well as a position-dependent differential Stark shift $\delta_{\text{AC}}(x) = \delta_{\text{AC}}^{(1)}(x) - \delta_{\text{AC}}^{(0)}(x)$. In the limit $\omega_q \ll |\Delta|$,

$$\delta_{\text{AC}}(x) \approx -\frac{\omega_q}{\Delta^2} \sum_{i=1,2} \sum_{j=+, -} |\Omega_i^j(x)|^2 \quad (4.9)$$

$$= -\frac{\omega_q}{\Delta} \tilde{U}_0(x) \quad (4.10)$$

This differential Stark shift is estimated to be small, $\delta_{\text{AC}}/2\pi \approx 2.7 \text{ kHz}$ for the numbers used in the simulations, and can be compensated by a corresponding Raman detuning.

Photon scattering on the D1 transition can be estimated as $\gamma_{\text{ph}} \sim \tilde{U}_0 \Gamma / (\hbar \Delta) \sim 9 \text{ s}^{-1}$ with $\Gamma = 1.23 \times 10^8 \text{ s}^{-1}$ in Yb^+ . This adverse effect may be reduced significantly by employing hollow tweezers [53, 92, 101, 109] at the expense of added complexity. For a hollow beam with a waist $w_0 = 0.5 \mu\text{m}$ and $\sim 450 \mu\text{W}$ we obtain a scattering rate of $\sim 0.47 \text{ s}^{-1}$. As long as $\omega_{\text{tw}} \ll \Omega_{\text{rf}}$, the drive frequency of the Paul trap, no parametric excitations can occur and micromotion of the ions is not a problem. Other errors, such as due to intensity noise of the laser, heating of the ions due to electric field noise and decoherence due to magnetic field noise have the same effect as in other gate implementations. Finally, we note that because the tweezers are far detuned from the closest transitions, the exact overall frequency of the tweezer laser is irrelevant.

4.6 CONCLUSIONS

In conclusion, we have described a novel type of quantum phase gate based on the optical Magnus effect using optical tweezers in a linear chain of trapped ions. The main benefit is that the gate does not require counter-propagating laser fields, greatly simplifying the setup and eliminating errors due to phase instabilities between the gate laser beams. Furthermore, the state-dependent force generated by the Magnus effect allows to perform the gate by coupling to motional modes on the plane perpendicular to the direction of propagation of the tweezers allowing novel experimental implementations. The proposed gate does not require ground state cooling and can perform a quantum logic gate on any pair of ion qubits by spatial addressing. The expected gate fidelity rivals the state of the art also for ions that are not cooled to the ground-state of motion.

5

EXPERIMENTAL SET UP

This chapter describes the design and construction as well as the methodology employed in our experimental setup, which involves the confinement of two-dimensional ion crystals and the modification of their phonon spectrum using optical tweezers. Our primary objective is to demonstrate the feasibility of achieving tunable spin-spin interactions between ions by combining a global Raman scheme with optical tweezers. The construction and design of the setup presents a number of significant challenges:

Trap stability : In trapped ion quantum computing, it is essential to engineer a trap with low heating rates and excellent mechanical stability. To meet these requirements, we have chosen a “bulky” ion trap that has a length of $\approx 7\text{ cm}$ and a distance of $\approx 1\text{ mm}$ from the radial electrodes to the trap center. We also took into account the heating of the trap itself, as a bulky ion trap would require radio-frequency voltages of several hundred V_{pp} , and some of this power is typically converted into heat due to the resistance of the trap.

To mitigate this problem, we chose titanium as the substrate material for our trap due to its low thermal expansion coefficient. We then electroplated a layer of gold with a thickness of $\approx 30\text{ }\mu\text{m}$ onto the radio-frequency electrodes of the trap, corresponding to the expected skin depth at the frequency ($\sim 6\text{ MHz}$) used for driving the trap in our experiment.

Two dimensional crystals : In our experiment, we aim to arrange many ions in a two-dimensional shape. This offers several advantages, such as providing a natural platform for studying two-dimensional Hamiltonians and addressing scalability challenges in trapped ion experiments.

Typical linear Paul traps confine charged particles in three dimensions by utilizing oscillating and static electrodes to create a finite-sized potential well. The detailed principle of operation of Paul traps is described in Chapter 2.1. To create a two-dimensional trapping potential, we split the degeneracy in the radial direction by decreasing confinement in one direction and increasing it in the other. To this end, we incorporate additional electrodes near the trap center, which are engineered to accept high voltages of the order of kV while avoiding electrostatic discharges in vacuum. Once the ions reach low enough

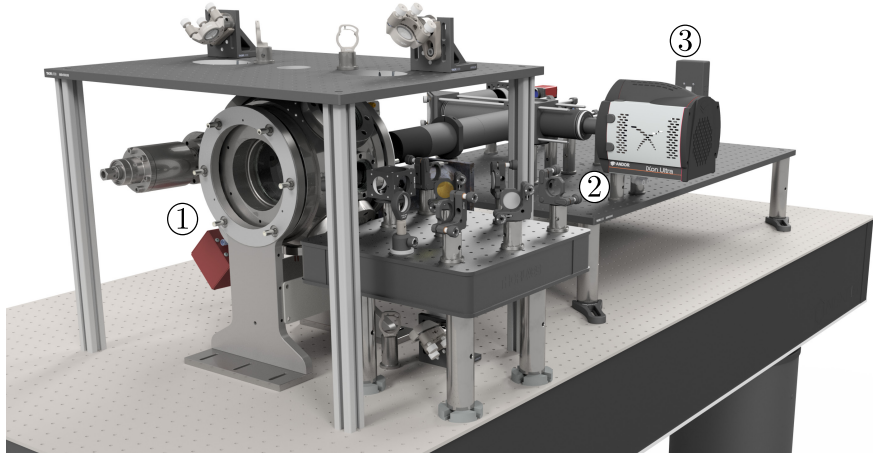


FIGURE 5.1: Rendering of the whole experimental setup (lasers not included) on the optical table. The setup is composed by: ① main vacuum chamber, ② imaging system and ③ SLM used for the generation of optical tweezers.

temperatures they tend to crystallize in a triangular lattice. Due to the particular shape of the potential in our trap this will happen on a two-dimensional plane.

Optical access : The control of qubit states is a key requirement for trapped ion quantum computers and simulators, with the energy separation between these states typically falling in the optical domain and thus requiring the use of lasers. Raman schemes that use lasers are also employed to excite the vibrational states of an ion crystal and require good optical access in order to address the ions from various directions. We use optical tweezers to modify the phonon spectrum of trapped ions, which requires tweezers with a power in the range of hundreds of mW and waists on the order of $1 \mu\text{m}$. Achieving such small waists at the ions' location necessitates the use of high numerical aperture (NA) optics. This translates into two primary design options: using short-focus lenses with small diameters that are situated in close proximity to the ions (typically in vacuum), or employing longer-focus lenses with larger diameters that can be located outside of the vacuum chamber. In our experiment, we selected the latter option, as it provides greater flexibility for further optimization, allowing us to access the optics without having to open the vacuum chamber.

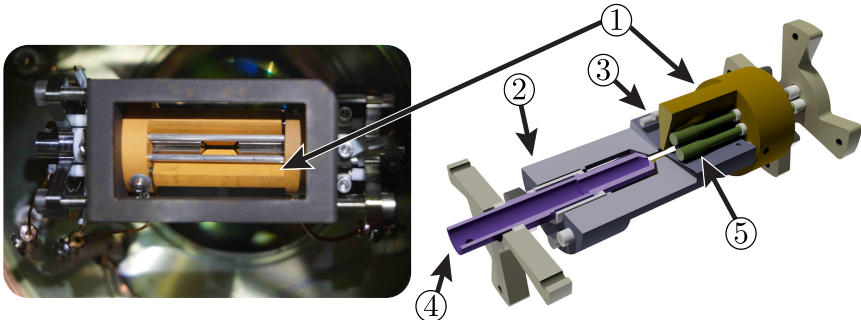


FIGURE 5.2: Left: Photo of the assembled radio-frequency trap used in the experiment. Right: Section view of the 3D model of the trap. The following composing elements can be seen: ① and ② pairs of gold plated radio-frequency electrodes for radial confinement, ③ compensation rods for micromotion compensation, ④ endcaps for axial confinement, ⑤ thick rods used for micromotion compensation and reshaping of the radial potential.

All the parts described in this chapter compose the experimental setup used in the scope of this thesis. The full rendering of the experimental setup described in this chapter can be seen in Fig. 5.1.

5.1 ION TRAP

Figure 5.2 displays the design of the linear Paul trap utilized in the experiment. The trap comprises two pairs of hyperbolically shaped electrodes that provide radial confinement to the ions, as shown in Fig. 5.3. Each pair of electrodes is constructed from a single block of grade 2 titanium. To reduce the total resistance of the trap, we coated the surface of the electrodes with gold, as described in section 5.2. To ensure precise alignment between the two pairs of blades, spherical insulating spacers made of ceramic material¹ are placed between them.

In addition to the blade pairs, the experimental setup incorporates other electrodes, constructed from stainless steel (SST-316), to provide confinement in all three directions. Among these additional electrodes are a pair of hollow endcap electrodes that are specifically designed to provide axial confinement. The hollow structure of these electrodes provides additional optical access from the sides of the trap. Furthermore, two pairs of compensation rods

¹ Ceratec Si3N4 G5 Ø2.5 mm

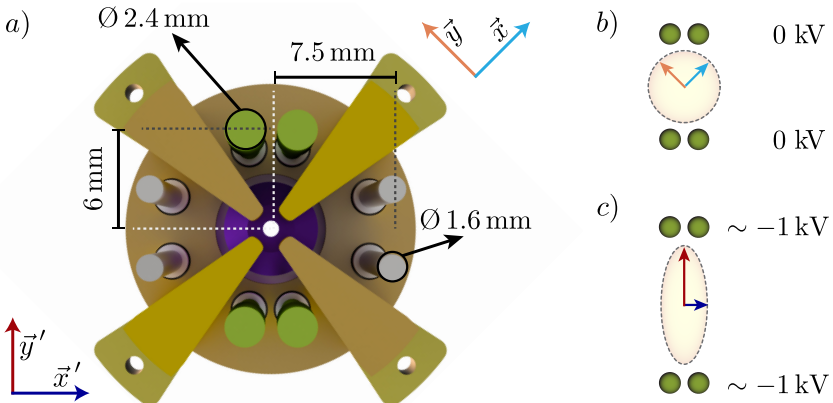


FIGURE 5.3: a) Section of the radio-frequency trap in the axial direction. In green are the HV electrodes used to stretch the radial confinement in the y direction. b) Representation of the change in trap potential (orange-yellow) when increasing the DC voltage on the HV electrodes.

are included in the setup to compensate for stray electric fields. These compensation rods are strategically positioned to counteract any undesired electric field components that may influence the ion confinement. By carefully adjusting the voltages applied to these compensation rods, the effect of stray electric fields can be minimized, resulting in improved trapping stability and accuracy.

Lastly, the setup incorporates two pairs of thicker rods that serve the purpose of stretching the confinement potential. These rods are employed to modify the shape of the potential well and create a two-dimensional crystal structure. By selectively stretching the radial confining potential in a specific direction, the ions arrange themselves in a two-dimensional crystal. The engineering of the potential shape, including the design and optimization of the voltages applied to these rods, is discussed in detail in the subsequent section, providing further insight into the construction and operation of the experimental setup.

5.1.1 *A flatter potential*

Our trap design, which differs from conventional linear traps, allows us to generate two-dimensional crystals. Typical radio-frequency traps use pairs of compensation rods in two perpendicular directions. Once a DC voltage is applied, these electrodes can be used to compensate for stray electric fields

or manufacturing defects of the trap that could cause excess micromotion (eMM).

We utilize a pair of such compensation electrodes to *stretch* the potential in one direction (see Fig. 5.3). This removes the radial degeneracy in trapping frequency such that one axis has stronger confinement than the other. To effectively compete with the strong radial confinement offered by the radio-frequency blades, the rods are thicker and closer to the center compared to conventional compensation electrodes. Fig. 5.3 provides information about the sizes of the DC electrode pairs and their distance from the trap center. We define \vec{x} and \vec{y} as the two orthogonal trapping axes aligned with the radio-frequency blades. In the absence of voltage applied to the HV electrodes, the trap configuration is as shown in Fig. 5.3b). However, by applying a strong (few kV) negative voltage on the thick compensation electrodes, we can decrease the trapping confinement in the y' -direction of the rods while increasing it in the x' -direction, as predicted by the Earnshaw theorem. The original vectors \vec{x} and \vec{y} are then rotated to new axes \vec{x}' and \vec{y}' as shown in figure Fig.5.3 c). The trap will now have two weakly trapping axes z and y' and a strong confining one x' . In this way the ions will tend to create crystals on the z - y' plane.

The two pairs of HV electrodes are connected to a negative polarity high voltage supply². The remaining electrodes, compensation rods (in gray in Fig. 5.3) and endcaps (in purple in Fig.5.3) are connected to a bipolar voltage supply³ in order to be able to control the ions position in all three directions.

5.1.2 Helical resonator and trap filtering

Typical radio-frequency voltage amplitudes used in bulky ion traps are in the range of ~ 100 V. These voltages are achieved by resonantly driving a *LRC* circuit which suppresses non-resonant signals and acts as a band filter, reducing possible ion heating due to external noise.

A helical resonator, also known as an auto-transformer, acts as an inductor L , while R and C are characteristic of the system itself (trap, resonator, and connecting elements). To achieve a strong confinement in the radial direction, we engineered the inductance of the helical resonator in order to bring the resonant frequency of the trap close to 6 MHz. This value is chosen to strike a good balance between minimizing intrinsic micromotion and achieving faster phase space dynamics. The resonance frequency of the circuit, consisting of the helical resonator and trap, is given by $1/\sqrt{LC}$. The capacitance also plays

² Iseg EHS 40 100n_S10, 4 channels negative polarity 0-10 kV/0,75 mA max per channel

³ Iseg EBS C0 30_SHV, 12 channels -3/3 kV 0.5 mA per channel

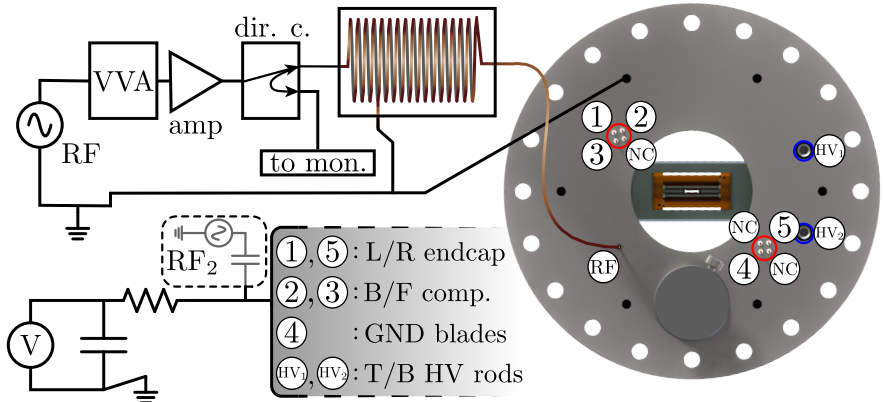


FIGURE 5.4: Schematics of the radio-frequency and DC circuits connected to the trap. The amplitude of the trap drive signal produced by a frequency generator (RF) is controlled using a variable voltage attenuator (VVA) before being amplified (amp.) and monitored through a directional coupler (dir. c.). The DC signals feedthroughs are circled in red and blue and connected as following: ① left endcap, ② back compensation rods, ③ front compensation rods, ⑤ right endcap, ④ grounded pair of blades, top high voltage rods (HV₁) and bottom high voltage rods (HV₂) are filtered through a RC circuit as described in the text. Optionally some DC electrodes are capacitive coupled to a second frequency generator (RF₂) used to resonantly excite the vibrational center of mass mode of the ions.

a role in the thermal dissipation of the trap, as described by the equation $P_d = \frac{1}{2}V_0^2\Omega^2C^2R$ [110], where V_0 is the radio-frequency voltage.

The trap capacitance is mainly influenced by the material used to isolate the various electrodes (in our case MACOR® ceramic) and the thickness of that material. We designed the trap to maintain a capacitance of around ~ 20 pF and measured it to be 18.8 ± 0.2 pF by minimizing the contact area between the electrodes and the ceramic, using vacuum as the primary electrical isolation. Although the capacitance and resistance are fixed once the trap has been produced it is possible to tune the resonant frequency of the system by adding an extra capacitance C_2 to the system or by changing L of the helical resonator accordingly.

The gold coating on the trap reduces its resistance, thereby reducing thermal dissipation. Titanium was chosen as the substrate for the radio-frequency electrodes due to its stiffness and low thermal expansion coefficient.

Parameter	Resonator 1	Resonator 2	Resonator 3
N windings	12	40	30
wire ϕ [mm]	2.5	0.8	1.1
coil ϕ [mm]	45	45	45
coil pitch [mm]	5.5	1.58	2.1
tube ϕ [mm]	80.5	80.5	80.5
tube length [mm]	108	108	108
Q	100	48	
Ω [MHz]	11.4	5.8	

TABLE 5.1: Characteristics of the various helical resonators used in the experiment.

The electrical connections to the trap are shown in Fig. 5.4. The radio-frequency source⁴ amplitude is controlled by a variable voltage attenuator⁵ before being amplified⁶. A directional coupler⁷ is present before the helical resonator in order to monitor⁸ and stabilize the reflectance from the trap using an FPGA board⁹. A second frequency generator¹⁰ can be optionally connected to some of the electrodes to measure the trapping frequency in various trapping directions as described in Chapter 6.2.

Several helical resonators were fabricated until the desired resonant frequency was obtained. To accomplish this, we modified a helical resonator that had been previously constructed [111]. Although we retained the same housing, the copper coil inside was altered. The first helical resonator (resonator 1 in Tab. 5.1) was composed of a coil wrapped around a PTFE core. The other two resonators were wound on a 3D-printed support.

Undesired heating of the ions can be induced by radio-frequency noise, resonant with the secular or drive frequencies, on the DC electrodes. For this reason we added a filter-board just outside the vacuum chamber in order to minimize possible pick-up noise in the cable going from the filters to the in-vacuum connections as shown in Fig. 5.4. Low voltage ($|V| \leq 3\text{ kV}$) electrodes use a passive RC ¹¹ filter with a cutoff frequency of 1.4 kHz. This

⁴ Hewlett-Packard 8657A

⁵ Minicircuits ZX73-2500+

⁶ Minicircuits ZHL-5W-1+

⁷ Mini-Circuits ZDC-10-1+

⁸ Analog Devices 6GHz RMS Power Detector LT558

⁹ Redpitaya STEMlab 125-14

¹⁰ Agilent 33250A

¹¹ $R = 50\text{ k}\Omega$ 5% Ohmite SM204035002JE, $C = 2200\text{ pF}$ 5% Kemet PHE450XB4220JB10R17

value was chosen in order to avoid introducing any limitation on the ramping speed of the power supply (3kV/s or ~ 4.5 kHz) while still effectively reducing possible spurious noise on the DC lines. High voltage electrodes ($|V| \leq 10$ kV) involved a greater challenge in finding components working reliably in the voltage range. We opted for a RC^{12} filter with a cutoff frequency of 2.1 kHz. This imposes a limit on the maximum ramping speed provided by the power supply (10 kV/s or ~ 15 kHz). However, the use of these electrodes is to modify the potential shape (as shown in Fig. 5.3b and c) and choose the geometry of the crystal in the experiment. Once this has been fixed no other dynamic adjustment is expected during normal operation.

5.2 GOLD PLATING

As mentioned in the previous sections, one of the destabilizing factors of ion traps is thermal heating generated by the strong voltages used for radial confinement. Typical bulky ion traps use principles of resonant circuits to build up voltages of the order of 200-300 V_{pp} at MHz frequencies. Our trap is no exception to this, achieving a radio-frequency amplitude of around 300 V. Even for the low resistance ($Ti \sim 5.2 \times 10^{-5} \Omega cm$, SST $\sim 7 \times 10^{-5} \Omega cm$) values of bare metal these amplitudes might lead to a significant increase in temperature of the whole trap and consequently a significant thermal expansion of the metal of the trap. Taking into account these factor we have chosen to use grade 2 titanium as the base component of the electrodes due to its hardness, magnetic properties and conductivity.

5.2.1 *Etching of titanium*

To ensure good adhesion of the gold to the Titanium substrate, the electrodes were etched to eliminate the thin layer of TiO. Due to its exceptional resistance to corrosion, titanium poses a significant challenge when it comes to the process of etching. Etching this metal necessitates the use of solutions with strong electron affinity like Hydrofluoric acid (HF). As we did not have prior knowledge of the process, we tested it on a pair of grade 2 titanium rods to evaluate the etching rate of HF on titanium. Here are the steps that have been taken in order to prepare and use the 3%HF etching solution :

1. In a big beaker, prepare a good amount of saturated sodium bicarbonate ($NaHCO_3$) solution. This solution will be used to neutralize the HF used in the procedure. For the amount of HF used in our procedure we

12 R = 50 k Ω 5% Ohmite SM204035002JE, C = 1500 pF 5% Vishay HVCC103Y6P152MEAX

prepared around 500ml of solution, although 3.5 ml of NaHCO₃ per ml of 40% HF should be sufficient.

2. Fill a 100 ml beaker with 37 ml demineralized water.
3. In another beaker pour some of 40% HF solution making sure to pour more than the necessary 3ml.
4. Using an automatic pipette withdraw 3 ml of HF and pour it slowly in the beaker with the demineralized water.
5. Once all the 3ml of HF have been poured in the beaker dispose of the pipette in the big beaker.
6. Stir the solution until the HF and the demineralized water are well mixed.
7. Insert the part that needs to be etched in the solution. After a few seconds bubbles should appear, confirming that the process has started.
8. Once the desired time has passed dispose of every part that was in contact with the HF in the big beaker and check that its pH is higher than 8.

A first etching and electroplating test was done using pairs of rods having a separation of 2 mm and a diameter of 2 mm in order to keep the geometry as similar as possible to the blade electrodes of the trap. The thickness of the rods has been measured at 4 different points before and after proceeding with the HF etching as shown in Fig.5.5. The rods have been kept in the solution for exactly 15 minutes while stirring the solution every few minutes. The diameter of the rods was measured before and after being immersed in the 3% HF solution for 15 minutes. We compare the change in diameter at various points as shown in Fig. 5.5. Multiple measurements were taken at different angles to minimize potential errors due to non-uniform etching. The etching rate of grade 2 titanium for the 3% HF solution was estimated to be $(6.98 \pm 0.16) \mu\text{m min}^{-1}$ based on our measurements. However, our estimation assumes a constant etching rate during the entire immersion time and does not account for the depletion of HF in the solution during the etching process. In our case, the exposed surface area of the rods was approximately 542 mm². Based on an average etching depth of around 0.1 mm during the 15-minute immersion period, we can estimate the total etched volume as approximately 50 mm³. The volume of the 3% HF solution used for the etching process was approximately 1200 mm³, well above the total etched volume. Therefore, the depletion of HF during the etching process in this range should be negligible.

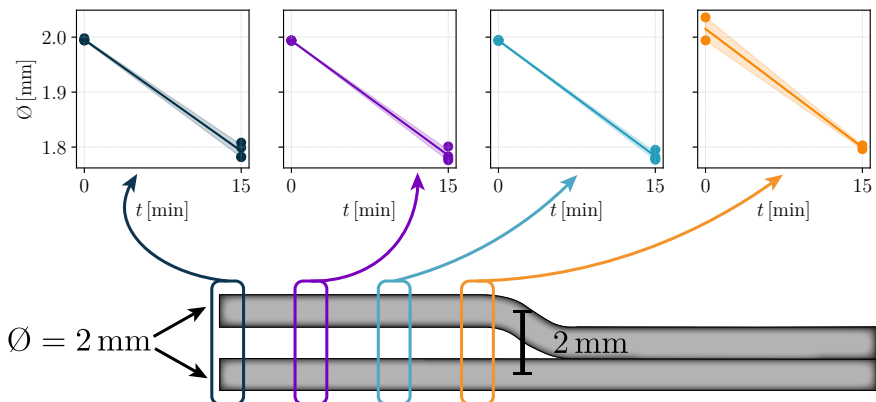


FIGURE 5.5: Schematic representation of the rods, having a geometry as similar as possible to the trap blades, used for testing the etching and electroplating processes. In the four plots has been reported the diameter at different points before and after the etching procedure showing an uniform amount of etched titanium at all four positions.

The process has been repeated for a similar time on several pairs of the trap blade electrodes. Each of them having a total exposed area of $\sim 33 \text{ cm}^2$. Although the total blade surface is much larger than the rods used in the test, it was challenging to reliably measure the change in diameter at multiple points before and after the process due to the complex geometry of the electrodes. Instead, a confocal scanning microscope was used to analyze the surface of the blades, as detailed in Sec. 5.2.3.

5.2.2 Gold electroplating

After having etched away the unwanted substrate of TiO from the blades' surface we proceeded to electroplate their surface. Considering the skin depth of gold at the trap drive frequency of 6 MHz, we aimed for a coating thickness of approximately $30 \mu\text{m}$. We initially tested the electroplating process on several pairs of test rods, similar to our approach for etching. In order to determine the optimal electroplating conditions, we immersed the rods in a gold electroplating solution¹³ for different durations and at different current values as depicted in Fig 5.6 b). We found that smoother surfaces were achieved at slow plating rates (low current) and by submerging the elements deep in the solution, away from the surface where turbulence increased the

¹³ Transene, TSG-250

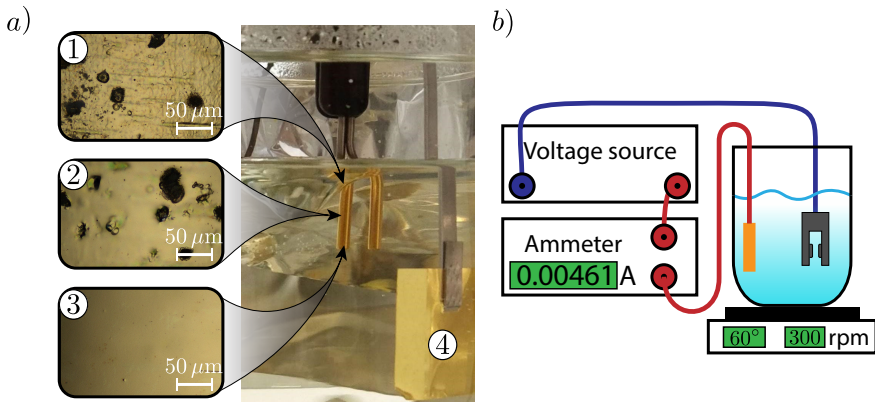


FIGURE 5.6: a) Effects of the turbulence on electroplating. The test rods surface more exposed to turbulence ① presents more defects than the surface of the rods that was more deep in the solution ③. Gold anode ④ used to keep a constant concentration of gold in the solution. b) Schematic representation of the setup used for electroplating.

rate of defects formation. The effects of turbulence and a schematic of the setup used in the process are shown in Fig. 5.6 a) and b). We observed that increasing the electroplating current resulted in a faster process, but at the cost of an uneven surface that did not adhere well to the titanium substrate. Therefore, we achieved the best results using a current of 5 mA. The final samples have been coated continuously for 57 hours and 8 minutes per pair of blades. For the whole plating process the blades have been rotated every 6 minutes in order to achieve a homogeneous plating of the surface. Using this method we achieve a gold coating thickness of $\sim 27 \mu\text{m}$.

5.2.3 Surface analysis

The surface roughness of the blades was examined using a confocal scanning microscope¹⁴. We compared the surface roughness of the blades after machining, etching, and gold plating. To quantitatively assess the surface roughness, we report the average of profile heights deviation from the mean surface (S_a) and the root mean square value of the profile heights deviation from the mean surface height (S_q). These two parameters are defined as:

¹⁴ Keyence VK-X1100

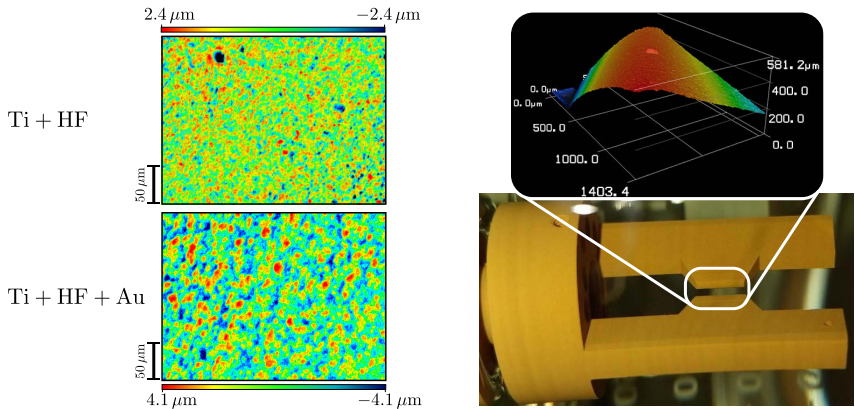


FIGURE 5.7: Surface of the radio-frequency electrodes before and after the plating process. Near the blades of the electrodes the surface appears smoother although a “big” ($\sim 40 \mu\text{m}$ tall) defect can be seen on the side, see right inset. No bigger defects have been noticed on both blades.

	S_a	S_q
Etched electrodes	0.6 μm	0.8 μm
Plated electrodes	1.0 μm	1.3 μm

TABLE 5.2: Measured surface roughness for etched and plated electrodes.

$$S_a = \frac{1}{A} \iint_A |z(x, y)| dA \quad S_q = \sqrt{\frac{1}{A} \iint_A |z(x, y)|^2 dA}, \quad (5.1)$$

where A is the analyzed area and $z(x, y)$ is the sampled height of the surface at the position x, y . We measure S_a and S_q before and after electroplating the electrodes. The comparison between etched and plated surfaces are reported in Tab. 5.2. Fig. 5.7 presents a comparison between microscope scans of the surface before and after electroplating. Although the surface roughness appears slightly worse after electroplating one has to consider that the average height/depth of a surface defect is on the order of few μm while the ions are trapped around 1 mm from the electrodes surface.

At that distance, the electric field inhomogeneities generated by the surface defects will average out and have a negligible effect. Despite the minor change in surface roughness, we observed a significant decrease in the resistivity of the trap. Taking into account that the thickness of the gold substrate

achieved is similar to the skin depth at a frequency of 6 MHz, and considering the resistivity of gold is approximately $\approx 5\%$ of that of titanium, it can be inferred that there is a significant decrease of approximately $\approx 95\%$ in the resistivity of the trap.

5.3 VACUUM SYSTEM

The design of the experiment's vacuum system took into consideration the need for optimal optical access, ultra high vacuum conditions ($\leq 1 \times 10^{-10}$ mbar), and the ability to use optical tweezers to address single ions. It also allows for greater freedom in making future improvements to the system.

Ultra high vacuum conditions are necessary to minimize collisions between the ions and background gases that could result in crystal melting or coherence loss. The assembly of the vacuum chamber can be seen in Fig. 5.8. The main optical access to the ion trap is provided by two large windows located on opposite sides of the vacuum chamber. The first window, visible in Fig. 5.8 behind the trap, has a diameter of 70 mm and is used for ion imaging and optical tweezers. The second one on the opposite side is a re-entrant viewport with a diameter of 102 mm. The trap is located at the exact center of the two windows such that optics with similar numerical aperture can be used. All around the vacuum chamber are three DN63CF windows and three DN35CF windows to maximize the laser access to the ions. One of the four DN63CF is used for a combined ion/NEG pump¹⁵. The DN35CF below the vacuum chamber is used for the oven used to load Yb in the trap. On the left side of the vacuum chamber there is a cross extension where one of the DN35CF windows, a gauge¹⁶ and a valve¹⁷ are connected. The valve is necessary for connections with an external pump, mostly used during bakeout. The pressure inside the vacuum chamber is monitored through the current reading of the ion pump.

The Yb oven used in the experiment can be seen in Fig. 5.8b). It is composed of two tubes, one of which is hollow and filled with Yb¹⁸. Both rods have a diameter of 2 mm. The hollow one has a wall thickness of 0.1 mm. Between the two rods a tantalum plate (0.1 mm thick, 10 mm long and 4 mm large) has been laser welded. By applying a constant current to the two rods, the plate can be heated, which in turn heats up the hollow tube containing Yb. The rate of Yb released in the direction of the trap can be adjusted by controlling the current supplied to the oven. In order to minimize potential

¹⁵ SAES Z300

¹⁶ Agilent UHV-24 Bayard-Alpert Ion Gauge Tube

¹⁷ VAT All-metal angle valve 57132-GE02

¹⁸ Sigma-Aldrich 548804 5g Ytterbium chunks 99.9% trace metals basis.

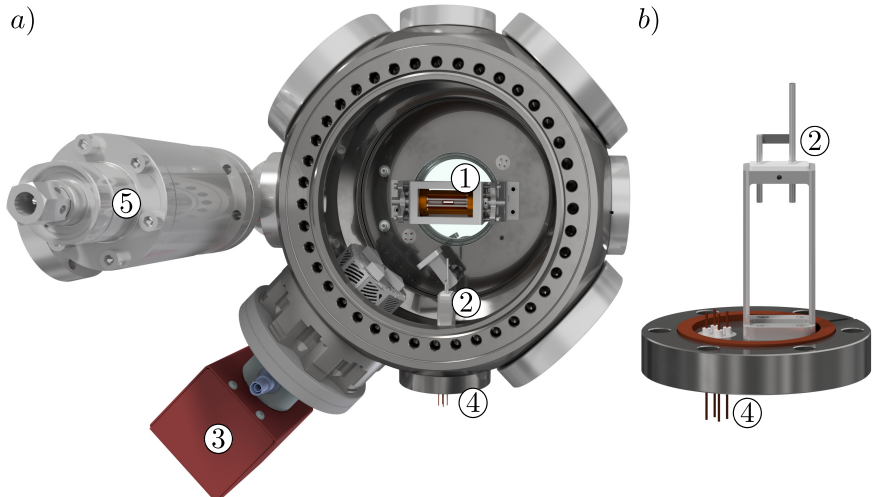


FIGURE 5.8: a) Rendering of the experimental vacuum system. ① Ion trap and 70 mm diameter window (behind it) used for optical tweezers and imaging. ② Yb oven and rotary feed-through. ③ NEG/ion pump, ④ Electrical connections for the oven, ⑤ Cross extension and valve used for connecting an external pump. b) Close up of the Ytterbium oven

collisions between the neutral Yb released by the oven and ionized Yb already present in the trap, a rotary feed-through¹⁹ is utilized as depicted in Fig. 5.8. By rotating the feed-through, the oven flux can be blocked or unblocked as needed.

5.3.1 Magnetic field

We typically use the magnetic insensitive transition $|^2S_{1/2}, F = 1, m_F = 0\rangle$ to $|^2S_{1/2}, F = 0\rangle$ as our qubit. Although this is a first-order magnetic insensitive transition, the usage of permanent magnets permits to achieve longer coherence times compared to coils [60]. For this reason and for splitting the $^2S_{1/2}, F = 1$ magnetic substates in $^{171}\text{Yb}^+$, an external magnetic field is provided by 74 permanent magnets²⁰ mounted in a circle around the vacuum chamber holder. Each of the circular holders mounted on each side of the

¹⁹ Hositrad Rotary Feedthrough H102100, Adapted by Technology Center, University of Amsterdam

²⁰ IBS Magnet SmCo DeltaMagnet® DE64

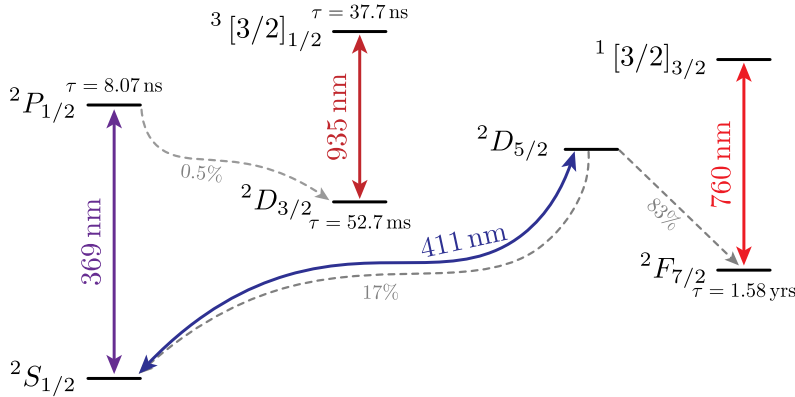


FIGURE 5.9: Relevant energy levels of $^{174}\text{Yb}^+$ [112–119].

vacuum chamber can hold up to 37 permanent magnets, and the magnetic field strength can be adjusted by adding or removing these magnets. The magnetic field at the center of the trap is approximately 1.5 G when using all 37 magnets.

Changing the magnetic field direction is not easy but will be necessary for EIT cooling and Raman interactions. To address this issue, a second holder has been built, which can hold up to 272 larger permanent magnets²¹. This new holder can be freely moved around the vacuum chamber to steer the magnetic field in the desired direction in the future.

5.4 LASER SYSTEMS

The majority of the experimental work in this thesis utilizes two isotopes of ytterbium, namely $^{174}\text{Yb}^+$ and $^{171}\text{Yb}^+$. The former is advantageous for a first characterization of the trap and alignment of optical tweezers as it requires a simplified optical setup due to the absence of nuclear spin, resulting in simpler internal energy levels compared to $^{171}\text{Yb}^+$. Moreover, the mass difference between the two isotopes has minimal impact on the trapping frequency or crystal configuration in the trap. The energy levels of $^{174}\text{Yb}^+$ and $^{171}\text{Yb}^+$ are shown, respectively, in Fig. 5.9 and 5.10. Despite the simplicity of the optical setup for $^{174}\text{Yb}^+$, $^{171}\text{Yb}^+$ remains of greater interest in the field of quantum computation and simulation. With a spin- $\frac{1}{2}$ nucleus, the $^2\text{S}_{1/2}$ state is split into $^2\text{S}_{1/2}, F = 1$ and $^2\text{S}_{1/2}, F = 0$. The states $^2\text{S}_{1/2}, F = 1, m_F = 0$ and $^2\text{S}_{1/2}, F = 0, m_F = 0$ (see inset in Fig. 5.10) are robust against magnetic

²¹ China Rare Earth Magnet Ltd. D6x10mm, Sm2Co17, magnetized through long axis

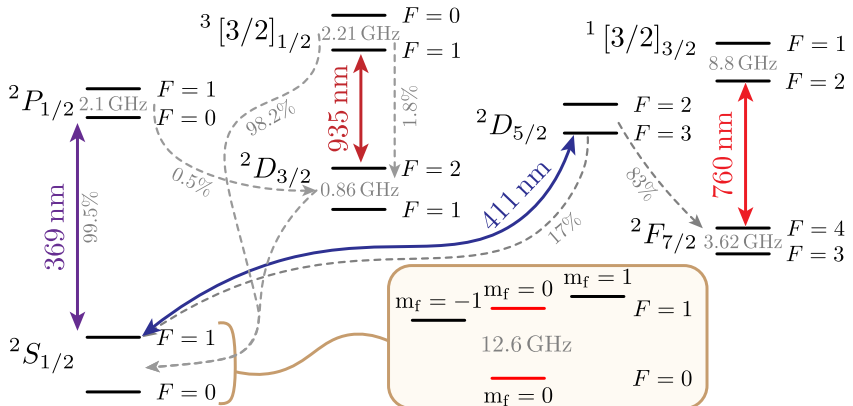


FIGURE 5.10: Relevant energy levels of $^{171}\text{Yb}^+$ [112–119].

field noise up to second order, making them suitable for use as qubits. The energy separation between these two qubit states is $\approx 12.64\text{ GHz}$. Since this transition falls within the microwave range, it can be driven using a microwave source or a Raman scheme. All the other internal transitions of both $^{174}\text{Yb}^+$ and $^{171}\text{Yb}^+$ must be addressed optically, requiring multiple laser systems, which will be discussed in subsequent sections.

5.4.1 Laser addressing of ions

The laser frequencies needed for trapping and controlling $^{174}\text{Yb}^+$ or $^{171}\text{Yb}^+$ are shown respectively in Fig. 5.9 and Fig. 5.10. The various lasers are aligned to the center of the trap as depicted in Fig. 5.11 and 5.18. The 935 nm, 760 nm, 369 nm and 399 nm lasers are overlapped on the side of the trap. The two UV beams (369 nm and 399 nm) from this side are used only for the photo-ionization process and switched off once the required number of ions in the trap has been reached.

Doppler cooling is provided by an extra 369 nm beam entering the trap from the bottom between the two blades. Notice that when dealing with linear crystals the voltage on the HV electrodes is set to 0. In this configuration the trapping axes are defined as in Fig. 5.3b and the bottom beam offers efficient cooling of all trapping directions (x' , y' and z). An extra 411 nm beam is entering the trap from the top left direction. This beam is used to pump the ions in the $^2\text{F}_{7/2}$ state when aligning optical tweezers using the 760 nm transition. This procedure will be described more in detail in Sec. 5.7

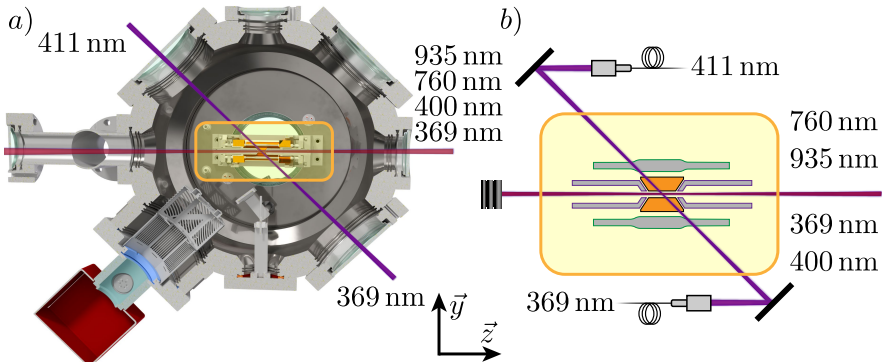


FIGURE 5.11: Sketch of how the laser beams are aligned to the (a) vacuum chamber and (b) ion trap.

5.4.2 Photo-ionization laser

Neutral Yb atoms are released from the resistive oven, as shown in Fig. 5.8b), by heating small Yb chunks inside it using a constant current applied to the oven’s resistance. To minimize vacuum contamination due to the substances released by the oven, we keep its temperature as low as possible while still allowing efficient loading (approximately one ion per few seconds). The oven is aligned with the center of the trap to ensure that most of the flux passes through this region. In the trapping region between the radio-frequency blades, we use a two-step photo-ionization process to ionize Yb. This allows us to select which Yb isotope is loaded into the trap. By tuning the laser frequency at around 399 nm in resonance with the $^1\text{S}_0 \rightarrow ^1\text{P}_1$ transition we can load one of the various stable Yb isotopes, such as ^{168}Yb , ^{170}Yb , ^{171}Yb , ^{172}Yb , ^{174}Yb , and ^{176}Yb . It is not possible to laser cool $^{173}\text{Yb}^+$ in our trap as its hyperfine splitting would require extra EOMs.

Once neutral Yb has been excited to the $^1\text{P}_1$ state a second photon at $\lambda < 394$ nm is necessary to reach the photo-ionization threshold. We use the 369 nm Doppler cooling laser for this second step. Both 369 nm and 399 nm lasers are overlapped at the center of the trap such that we make sure that the ionization happens near the center of the trap.

The 399 nm laser is a homebuilt external cavity laser diode (ECDL) adapted from [120]. The laser is composed of a diode²² and grating²³ in Littrow configuration. The temperature and current of the laser diode are controlled and

²² Nichia NDV4316 wavelength selected 399 nm

²³ Thorlabs GH13-24U, UV reflective holographic grating

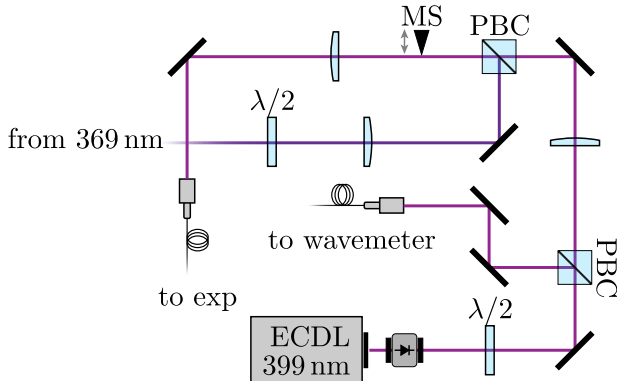


FIGURE 5.12: 399 nm laser setup.

stabilized by home-built electronics [121].

The 369 nm and 399 nm lasers enter the vacuum chamber from the side, as shown in Fig. 5.11. This orientation is chosen to minimize Doppler broadening, as it is perpendicular to the direction of Yb flux originating from the oven. The 369 nm laser for the second ionization step is red-detuned from the $^2\text{S}_{1/2} \rightarrow ^2\text{P}_{1/2}$ transition in singly-ionized Yb. This allows for efficient immediate cooling of atoms ionized at the center of the trap. The two lasers are overlapped at the laser setup as shown in Fig. 5.12. To achieve efficient ion loading, a substantial amount of power ($\sim 250 \mu\text{W}$ for the 369 nm laser and $\sim 4 \text{ mW}$ for the 399 nm laser) is used. However, such high power can easily saturate the camera. For this reason a mechanical shutter (MS) allows us to switch off both branches once the required amount of ions has been loaded. Since both beams pass through the hollow endcaps of the trap along its axis, they need to have a sub-millimeter waist at the center of the trap. With a power of $\sim 4 \text{ mW}$ and a waist of $\sim 1 \text{ mm}$ the 399 nm laser is well above the required saturation limit of neutral Yb ($I_{\text{sat},1\text{P}_1} = 60 \text{ mW/cm}^2$ [115]). During loading, the laser frequencies can be monitored on a wavemeter²⁴. A home-built PID system²⁵ based on a fast analog output controller²⁶ takes care of compensating for frequency drifts.

²⁴ HighFinesse WS7-3

²⁵ WavemeterService, WMonitor

²⁶ National Instrument NI6713

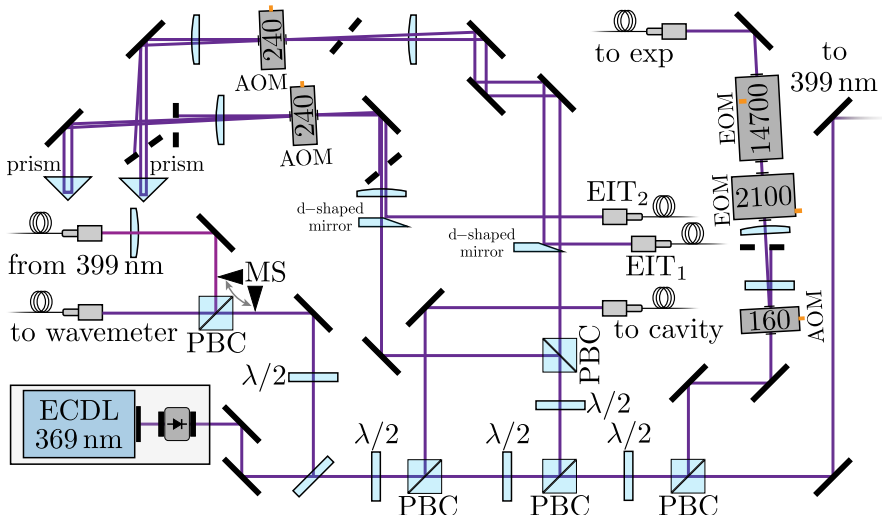


FIGURE 5.13: 369 nm laser setup. All AOM and EOM frequencies reported in the figure are in MHz.

5.4.3 Detection and cooling laser

The 369 nm laser used for photo-ionization, imaging, and cooling of the ions in the trap is based on a commercial ECDL²⁷. The laser drives the dipole $^2\text{S}_{1/2} \rightarrow ^2\text{P}_{1/2}$ (D1) transition in Yb (see Fig.5.9 and 5.10). With a lifetime of $\tau = 8.12(2)$ ns [117] this transition is suitable for Doppler cooling and imaging of the ions. Additionally, the transition can be employed for implementing sub-Doppler cooling [122, 123] of ion crystals. The schematic of the laser setup [121] can be seen in Fig.5.13. The laser diode is kept detuned by ~ -170 MHz from the $^2\text{S}_{1/2} \rightarrow ^2\text{P}_{1/2}$ in Yb^+ . One of the branches is overlapped with the 399 nm for the photo-ionization step as described in Sec.5.4.2. Having only one channel available a mechanical switch (MS) permits to select which of the two lasers' frequencies to monitor on the wavemeter. A second branch goes to the experiment after passing through a controllable +160 MHz AOM, a 2.1 GHz EOM (used for state initialization of $^{171}\text{Yb}^+$) and a 14.7 GHz EOM (used for cooling and detection of $^{171}\text{Yb}^+$). This branch is nearly resonant with the D1 transition and enters the trap from the bottom as can be seen in Fig.5.11. To compensate for frequency

²⁷ Toptica DLC DL PRO HP 369.

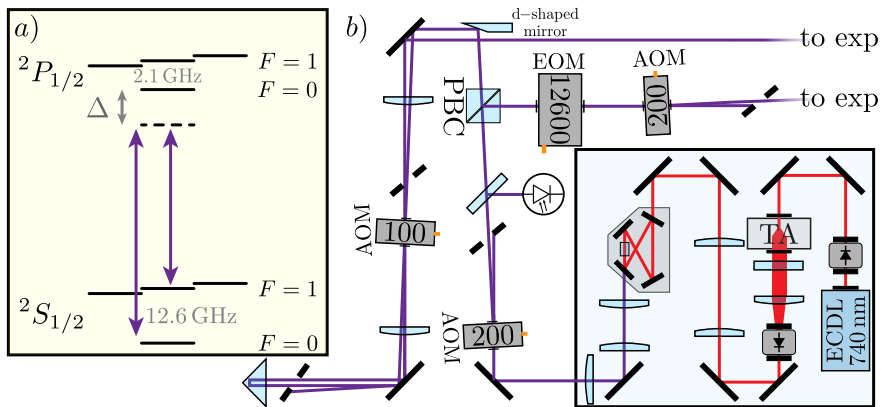


FIGURE 5.14: a) A Raman scheme can be achieved by using two laser beams detuned by ~ 13.8 THz from the $S \rightarrow P$ transition in $^{171}\text{Yb}^+$. This can be done by using a 12.6 GHz EOM. b) Raman laser setup used in the experiment.

drifts during normal operation the laser is kept locked to a low finesse cavity as described in Sec.5.5.

Another two EIT (EIT_1 and EIT_2) branches are present in the setup [124]. These will allow us to efficiently cool two-dimensional crystals [123] of ions to the Lamb-Dicke regime necessary in order to reliably implement quantum gates.

5.4.4 Raman Laser

Generating state-dependent forces on ions is crucial for achieving spin-spin interactions. This is done by driving a Raman $^2\text{S}_{1/2}, F = 0 \rightarrow ^2\text{S}_{1/2}, F = 1, m_F = 0$ transition using a high-power frequency-doubled laser²⁸, as depicted in Fig. 5.14. The laser can deliver up to 130 mW at 369 nm and is tunable within ± 5 nm. To minimize intensity noise during gate operations, an intensity stabilization circuit²⁹ is included in the laser setup.

A 200 MHz AOM used for intensity stabilization can also be employed for pulse shaping. Assuming a total usable power of approximately ~ 50 mW on the ions, a detuning of 13.8 THz, and a beam waist of $100 \mu\text{m}$, to address ion-crystals evenly, we obtain a two photon Rabi frequency of 12.5 kHz and a scattering rate of 0.5 s^{-1} .

²⁸ Toptica TA-SHG pro 369

²⁹ Digital Controller for Laser Intensity Stabilization [125]

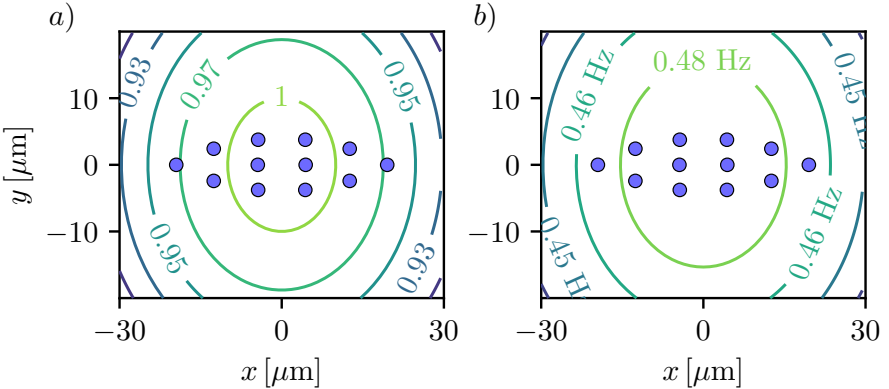


FIGURE 5.15: a) Normalized Rabi frequencies for two global Raman beams with $100 \mu\text{m}$ waist and 50 mW power each. For $^{171}\text{Yb}^+$ we find $\Omega_{\text{eff}} \sim 2\pi \cdot 13.6 \text{ kHz}$ at the center. b) scattering rate \mathcal{R} . The crystal parameters and size are the same as in Fig. 2.2

The two Raman branches have an offset of 12.6 GHz in order to couple the two hyperfine states in the ${}^2\text{S}_{1/2}$ state. Two separate AOMs, driven by two phase-locked DDS³⁰, can tune the frequency offset between the two laser branches, allowing for control of the beat-note frequency necessary to off-resonantly excite the ion chain's motional modes.

In our experimental setup, we intend to employ two global Raman beams to induce spin-spin interactions between ions [78, 85]. When such a beam is applied to a two-dimensional crystal that is relatively large compared to the usual beam size, it becomes necessary to consider the spatial overlap between the two. This beam-size effect is illustrated in Figure 5.15. Ions located at the border of the crystal experience Rabi frequencies which are approximately 3% less than those at the center, leading to inhomogeneous spin-spin interactions. This issue can be mitigated by using elliptical beams instead of Gaussian beams, or by correcting for the inhomogeneities using optical tweezers.

5.4.5 Repumper lasers

During cooling and detection using the D1 transition in Yb^+ it is possible to populate the metastable ($\tau \sim 52 \text{ ms}$) ${}^2\text{D}_{3/2}$ as the ${}^2\text{P}_{1/2}$ has a non-zero

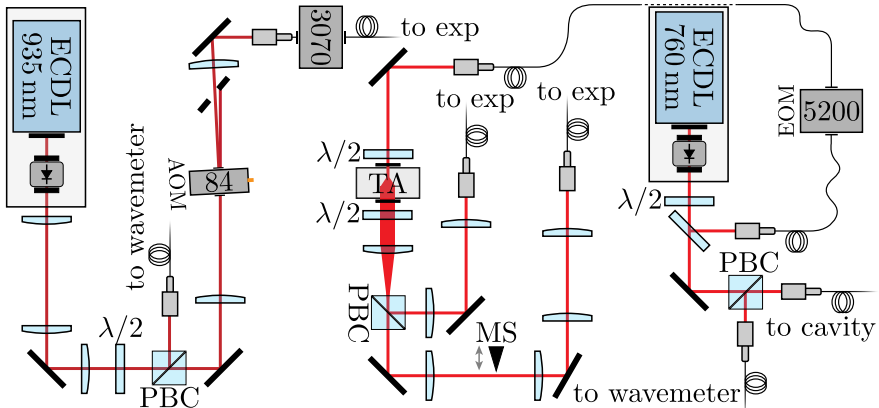


FIGURE 5.16: left: 935 nm and right: 760 nm lasers setup. All reported AOM and EOM frequencies reported in the figure are in MHz.

branching ratio (0.5 % [114]) (see Fig.5.9). Populating the mentioned state reduces fluorescence and cooling efficiency. To overcome this issue, we use a repumper laser operating at a wavelength of 935 nm. Through resonant excitation of the $^2D_{3/2} \rightarrow ^3[3/2]_{1/2}$ transition, the population residing in the metastable $^2D_{3/2}$ state can be transferred back to the $^2S_{1/2}$ ground state. In fact, the upper $^3[3/2]_{1/2}$ state has a shorter lifetime (~ 38 ns) and a ~ 98 % branching ratio to the ground state $^2S_{1/2}$. In case of $^{171}\text{Yb}^+$ an EOM is necessary in order to address all the hyperfine substates as shown in Fig. 5.10.

Collisions with background gases happening when Yb^+ is in the $^2D_{3/2}$ state can cause decay to the long lived (~ 1.58 yrs) $^2F_{7/2}$ state. This state can also be populated when driving the $^2S_{1/2} \rightarrow ^2D_{5/2}$ quadrupole transition at 411 nm as shown in Fig. 5.9. Having a natural line-width of $\Gamma = 2\pi \times 22$ Hz this narrow quadrupole transition is mostly used for ion thermometry, electron shelving and for the first alignments of optical tweezers.

Both 935 nm³¹ and 760 nm³² systems are based on a commercial ECDL. The full optical setup for both lasers is shown in Fig. 5.4.5. The frequencies of both lasers are monitored using a wavemeter, with the 935 nm laser relying solely on this for frequency stabilization, similar to the system used for the 399 nm laser described in Sec.5.4.2. The 760 nm laser can be locked to an external cavity for better stability as described in Sec.5.5. Both lasers are

³¹ Toptica DLC DL PRO 935.

³² Toptica DLC DL PRO 760.

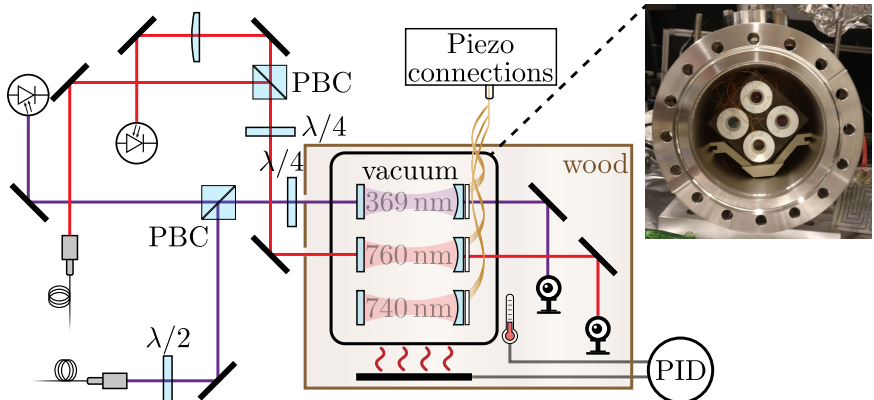


FIGURE 5.17: Optical setup for locking lasers to the cavity. The ZERODUR® block with the four cavities in it can be seen in the inset. Notice, in white, the piezoelectric rings used to tune the cavity length and keep the lasers resonant with the transitions in Yb^+ .

equipped with fiber EOMs needed when trapping $^{171}\text{Yb}^+$ to address all hyperfine states.

The 760 nm laser is further amplified using a tapered amplifier (TA). This gives us up to 100 mW of usable power at the trap location in order to efficiently drive the ${}^2\text{F}_{7/2} \rightarrow {}^1[3/2]_{3/2}$ transition.

5.5 OPTICAL CAVITY

Some of the lasers described in Sec.5.4 are locked to a medium-finesse optical cavity [121]. The cavity, shown in Fig. 5.17, is made out of a single ZERODUR® block³³ adapted from a previous unused cavity [111] in which four bores have been machined. Each of the bores is used as a cavity-unit at a different wavelength, although we use only three of the four cavity-units. ZERODUR® has been chosen thanks to its extremely low thermal expansion coefficient in order to minimize thermal drifts in cavity length. The whole block has a length of 10 cm and has been inserted in a vacuum chamber for a better isolation from the surrounding environment. By baking the vacuum chamber at $\sim 95^\circ\text{C}$ for three days we reach a vacuum of $< 1 \times 10^{-8}$ mbar. In order to reduce thermal fluctuations the vacuum chamber is wrapped in resistive heaters and foam. A PID controller takes care of keeping the temper-

³³ Schott AG, Expansion Class 0. Modified by Glass Instrumentation, Technology Center, University of Amsterdam

ature of the cavity stable at $\sim 27^\circ\text{C}$. Further isolation from the environment is provided by a wooden box that encloses the vacuum chamber and part of the optical setup as shown in Fig. 5.5.

With a cavity-unit length of 10 cm we obtain a free spectral range $\nu_{\text{fsr}} = 1.5 \text{ GHz}$. Both 369 nm and 760 nm lasers are locked to two of the cavity-units using the Pound-Drever-Hall (PDH) method [126]. In order to fulfill the resonance condition on the ions the mirrors mounted on one side of the cavity are glued³⁴ to MACOR® ceramics holder in turn glued to two piezoelectric rings³⁵. The laser can be kept at the desired frequency while adjusting the cavity length using the voltage supplied to piezoelectric rings until one of the cavity modes come in range. Once the laser has been locked to the cavity, the piezoelectric rings are also used to keep the frequency stable by using a PID system, based on the wavemeter-readings, similar to what has been described in Sec. 5.4.2.

All three cavity units use a plano-concave configuration with a plano-plano mirror directly glued on the ZERODUR® block. The other plano-concave mirror with a radius of curvature of 250 mm are mounted on the MACOR® ceramic holders. Two of the cavity-units mirrors are coated³⁶ for usage in the 740 – 760 nm range. These two cavity-units are used to lock the 760 nm laser and the 740 nm Raman source. A third cavity-unit using UV coated mirrors³⁷, is used to lock the 369 nm laser. All the three cavity-units utilize mirrors with a reflectivity $R \sim 99.7\%$ achieving a finesse $\mathcal{F} \sim 1000$ and a line-width $\delta_\nu = 1.4 \text{ MHz}$. In the following subsection the three cavities are described more in detail.

5.5.1 UV cavity

The UV cavity is used to lock the 369 nm laser used for cooling and detection of the ions. The mirror reflectivity curve allows for a second laser at 411 nm to be locked to the cavity. In this way it would be possible to realize a transfer-lock as the 411 nm laser used in the experiment is also locked to a commercial high-finesse cavity ($\mathcal{F} = 26500$).

We couple around $100 \mu\text{W}$ of laser light to the cavity. The laser is locked to the cavity through a typical PDH locking scheme. We use a DDS³⁸ to generate a signal at 18.6 MHz. This is used to modulate the laser current ($\sim 74 \text{ mV}_{\text{pp}}$). The reflected signal from the cavity is measured by a photo-diode³⁹ and

³⁴ Epoxy Technology, OG142-112

³⁵ Meggitt A/S OD24.4 ID22.4 L4 and OD18.3 ID16.7 L4

³⁶ Altechna UVFS $\varnothing = 12.7 \text{ mm}$, $R > 99.7\% @ 740 - 760 \text{ nm}$, AOI = 0°

³⁷ Lens-Optics $\varnothing = 12.7 \text{ mm}$, $R = 99.7 \pm 0.2\% @ 369 - 411 \text{ nm}$, AOI = 0°

³⁸ Analog Devices EVAL-AD9854, PicoDDS

³⁹ Thorlabs PDA10A-EC

further amplified⁴⁰. Due to the poor performances of the photo-diode in the UV-range the signal requires a fair amount of amplification and filtering. For this reason a custom made photo-diode amplification board⁴¹ will be installed in the future to improve the signal-to-noise ratio.

The signal measured at the photo-diode is then filtered and mixed⁴² in order to obtain an error signal. The best error signal is found for the $\text{TEM}_{pl}(0,8)$ mode. The phase between the modulation source and the photo-diode signal is fixed by choosing cables of appropriate length. Once demodulated the error signal is sent to the laser head current DC modulation input for a fast feedback ($\sim \text{MHz}$) and to a programmable FPGA⁴³ for a slower feedback on the laser piezoelectric actuator ($\sim \text{kHz}$). The PID settings of the latter feedback can be controlled through a web-interface⁴⁴.

5.5.2 *IR cavity*

The infrared (740 nm and 760 nm) cavity uses a similar lock system as for the previously described UV cavity. Also in this case, roughly $100\,\mu\text{W}$ of laser light is coupled to the cavity. Thanks to the increased performances of photo-detectors in the infrared, however, the system does not require as much amplification as in the UV case. The frequency modulation is generated by a programmable FPGA⁴³. The FPGA is also used for demodulation of the error signal that is then sent to the digital laser controller with built-in PID⁴⁵. The locking parameters in this case are directly chosen on the laser controller.

5.6 DETECTION SYSTEM

The detection system used in the experiment is shown in Fig. 5.18. The detection of ions is primarily carried out using a high-performance EMCCD camera⁴⁶, which has a quantum efficiency of approximately $\sim 54\%$ at 369 nm. To prevent contamination from background light, a narrow UV filter⁴⁷ is positioned before the camera and PMT⁴⁸. Using a mechanical flip mirror⁴⁹ it

⁴⁰ Minicircuits ZFL-500LN+

⁴¹ Hamamatsu S5973-02. Amplification board custom made from the electronic workshop at University of Amsterdam

⁴² Minicircuits ZFL-500LN+

⁴³ Redpitaya STEMlab 125-14

⁴⁴ Lock-in+PID [127]

⁴⁵ Topical DLC PRO

⁴⁶ Andor iXon Ultra 897 UVB

⁴⁷ Semrock 370/6 nm BrightLine® single-band bandpass filter

⁴⁸ Sens-Tech P25PC

⁴⁹ Eksma optics Motorized Flipper Mount 940-0090

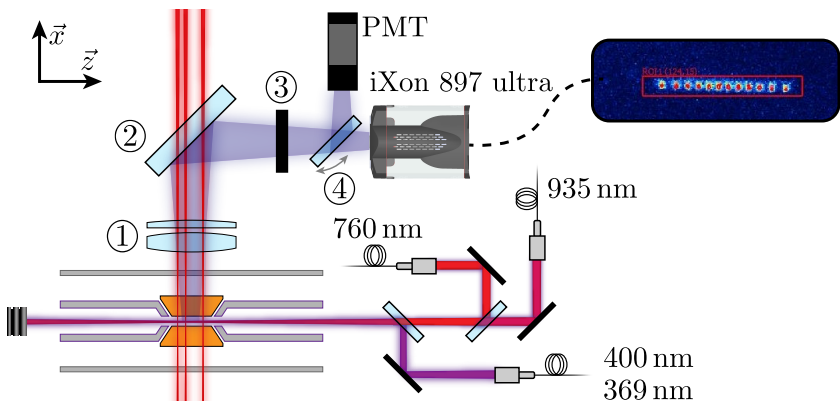


FIGURE 5.18: Top view of part of the setup used for imaging of the ions and optical tweezers. The light collected from the ions by the imaging lenses ① is split from the tweezers light using a dichroic mirror ② and redirected after filtering ③ to a camera or a PMT for detection using a mechanical flip mirror ④. In the inset is an ion string of 12 ions as typically rendered in our control system.

is possible to switch between the camera or PMT for light detection. While the PMT offers a higher detection speed of approximately 100 MHz it is not possible to use it to detect more ions at once or to discriminate between various crystal configurations. For this reason we mostly perform detection using the camera.

The lenses⁵⁰ closer to the vacuum chamber are shared by the optical tweezers and the imaging system. They consist of a doublet composed of a 2-inch aspherical lens with an effective focal length of 80 mm and a numerical aperture of 0.29, and a 2-inch plano-convex lens with a focal length of 750 mm. The two lenses together form a telescope with a magnification factor of ~ 8.3 . We plan to generate optical tweezers using a $\lambda = 800$ nm commercial laser system⁵¹ having a peak power of ~ 2 W. To ensure optimal performance for both the imaging and optical tweezers, we simulated⁵² the optical system and determined the best configuration to minimize spherical aberrations at both the 369 nm and 800 nm. We choose to image the ions from the side of the trap where the compensation rods are thinner (as shown in Fig. 5.3). This enables us to maximize our photon collection efficiency, which is now

⁵⁰ Asphericon AFL50-80-S-U and Thorlabs LA4745. Coating : Tafelmaier X/UAMCS1 $R < 0.5\% @ 350-425/800-1100$ nm

⁵¹ Toptica SYST DL PRO 808 nm

⁵² OpticStudio Zemax

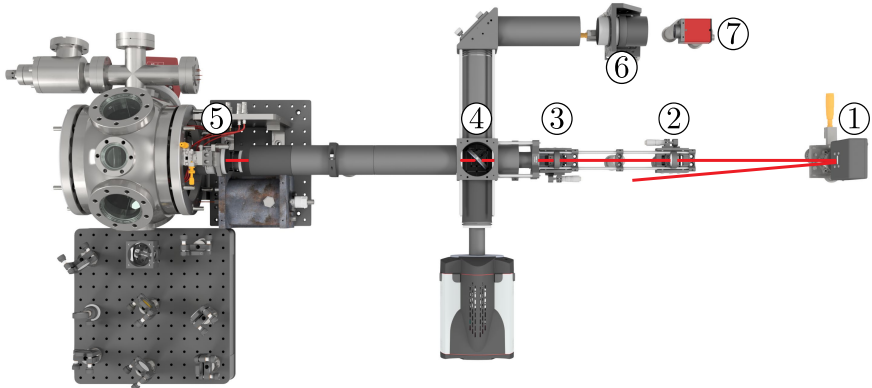


FIGURE 5.19: CAD rendering of the SLM setup. A SLM ① is used to control the phase pattern of incident light. After the first lens ② the desired intensity pattern is obtained. Lenses ③ and ⑤ compose a telescope to demagnify the tweezers on the ions. A dichroic mirror ④ is used to separate imaging light from the tweezer's light. A second camera ⑦ can be used to monitor the tweezers during the experiment, the last two lenses ⑥ before this camera are the same as the ones used for the imaging system ⑤.

limited by the numerical aperture of the lenses rather than any geometrical limitations of the trap itself. With a distance of ~ 70 mm from the center of the trap and a diameter of 2 in. we obtain a 3% collection efficiency that gets further reduced to 1.4% once taken into account the quantum efficiency of the camera and the reflectivity of the dichroic mirror⁵³.

5.7 SPATIAL LIGHT MODULATOR

The optical setup used to generate optical tweezers can be seen in Fig. 5.7 and is composed by a positive meniscus lens⁵⁴ after the SLM. The optical beam has an initial diameter of ~ 12 mm in order to maximize the filling of the active SLM surface. In order to maximize the SLM efficiency the maximum angle of incidence on the SLM has to be $< 5^\circ$. This poses a constraint on the distance between the SLM and the first lens that has to be at least 15 cm away from the SLM head to avoid any cropping of the incoming beam. A second lens⁵⁵ and the two lenses before the vacuum chamber (used also for imaging

⁵³ Thorlabs DMLP505L

⁵⁴ Thorlabs LE1234-B

⁵⁵ Thorlabs LBF254-150-B

purposes, see Sec. 5.6) compose a telescope to de-magnify the tweezers size down to a few μm of diameter. Both lenses are mounted on micrometer translation stages for precise alignment of the beam focus. The SLM is also mounted on a micrometer precision translation and rotation stage for small adjustments. The tweezers intensity and shape can be monitored through part of the light reflected by the dichroic mirror using a second camera.

We use a reflective SLM⁵⁶ to create our optical tweezers. This SLM functions as a programmable optical element, allowing us to manipulate the phase of an incident beam at each pixel. By doing so, we take advantage of the interference phenomenon to generate laser intensities of any desired shape.

A typical SLM is based on liquid crystal technology, where the crystal orientation of each pixel can be controlled through the application of varying voltages. As the crystal is birefringent and the incoming light is linearly polarized, the refractive index experienced by the light wave will differ based on the pixel's chosen crystal orientation. By controlling the phase delay at each pixel, we can imprint a phase pattern onto the incoming light, thereby controlling its intensity. This intensity control is based on the Fourier transform properties of lenses. In fact, by applying Fourier optics to the optical elements, we can demonstrate that the intensity at the focus position of the first lens after the SLM is determined by the Fourier transform of the incident light.

6

SET UP CHARACTERIZATION

This chapter describes the characterization of the experimental setup illustrated in Chapter 5. We first characterize the background pressure of the vacuum chamber which puts a limit on the stability of the system. Collisions between an ion crystal and a background molecule induce a melting event forcing the ions to rearrange in a new crystalline structure. Such events can disrupt the system during measurements, necessitating a fresh initialization process and resulting in a decrease in the data acquisition rate. Next, we proceed to characterize the ion trap utilized in the experiment. We measure the field curvatures produced by the various electrodes and investigate how the HV electrodes split the radial degeneracy, enabling the creation of two-dimensional crystals.

Following that, we analyze and characterize our imaging system to determine its magnification factor. This factor proves to be useful to compensate for micromotion and mapping the intensity distribution of the optical tweezers.

Finally, we delve into the description and characterization of the SLM employed in the experiment. We explore various experimental factors that must be taken into account when aligning the optical tweezers with a single ion. We outline the alignment procedure for the optical tweezer to a single ion, demonstrating how precise control of the SLM and trap voltages allows for the complete mapping of the tweezer's shape.

6.1 BAKING OF VACUUM SETUP

In order to achieve a ultra-high vacuum (UHV) environment, we performed a high temperature baking of the whole vacuum chamber (view-ports excluded) at $\sim 500^\circ\text{C}$ for 8 hours. During this process the steel (SST) that composes most of the vacuum chamber oxidizes. This creates an oxide layer on all SST surfaces such that the hydrogen present in the metal cannot escape.

After completing the assembly of the whole vacuum setup shown in Fig. 5.8 we connected the vacuum chamber to a turbo pump through the vacuum valve (element 5 in Fig. 5.8). Once the pressure has stabilized to $\sim 10^{-7}$ mbar level we increased the temperature of the vacuum chamber up to $\sim 240^\circ\text{C}$ in a period of few days. The limit in maximum temperature has been imposed by the Kapton insulation around the copper cables that connect the ion trap to the external power feedthroughs. The speed of the temperature increase

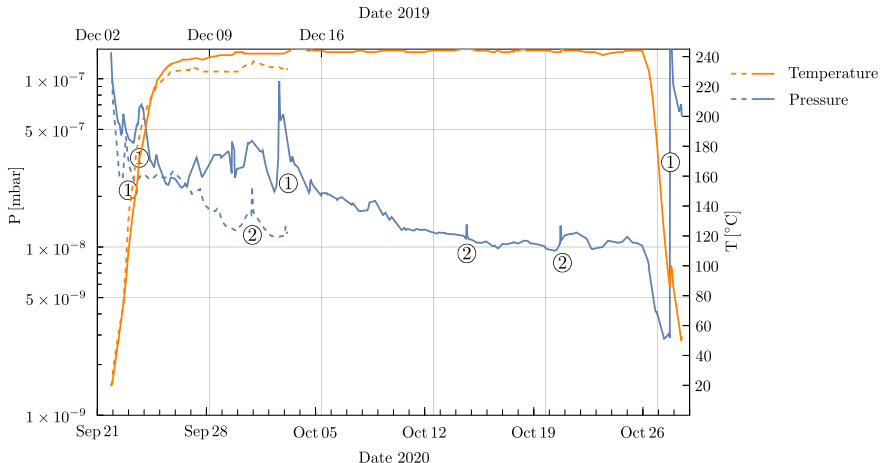


FIGURE 6.1: Temperature (orange) and pressure (blue) evolution of two different bakings of the vacuum chamber done in December 2019 (dashed) and October 2020 (solid). At certain times during the baking, the NEG element has been activated (①, $\sim 525\text{ }^{\circ}\text{C}$) or conditioned (②, $\sim 300\text{ }^{\circ}\text{C}$). The vacuum chamber has been heated to $\approx 240\text{ }^{\circ}\text{C}$

was kept low in order to reduce the possibility of cracks in the glass¹ that composes the viewports ($< 1\text{ }^{\circ}\text{C}/\text{min}$).

We performed two main bakings of the vacuum chamber in order to improve the vacuum quality. The two bakings were performed in December 2019 and October 2020 for a duration of 2 weeks and ~ 1 month, respectively. A third baking was performed in August 2022 when the vacuum chamber extension used for connecting the ion pump and the Yb oven have been replaced. Both the 2020 and 2019 baking can be seen in Fig. 6.1. At the beginning and the end of the baking procedure, the getter element² has been heated to $\sim 525\text{ }^{\circ}\text{C}$ (activation). Furthermore, low temperature activations $\sim 300\text{ }^{\circ}\text{C}$ (conditioning mode) were performed each 5-7 days in order to clean the getter element.

6.1.1 Vacuum characterization

Maintaining UHV or even lower pressure is crucial to prolong the lifespan of ion crystals. Melting events can be triggered by collisions between ions and

¹ Kodial, Alkali Borosilicate 7056

² SAES Non Evaporable Getter (NEG)

background gases. Typically, these collisions follow the Langevin type [128, 129].

To determine the number of background gas collisions that occur within a specific time frame for a linear chain of N ions, we load a chain of 7 ions with one ion maintained in a dark state, such as ${}^2F_{7/2}$. By capturing an image of the crystal every 200 ms, we track the position of the dark ion over a duration of 200 s. Figure 1.4 shows the time evolution of this process, with the dark ion hopping between different positions in the ion chain.

The Langevin collision rate, denoted as η_L , is related to the density of the background gas, ρ_b . We can express ρ_b as $\rho_b = \eta_L / (2\pi)\sqrt{\mu_b/C_4}$, where μ_b is the reduced mass of the ion background-gas system, and C_4 represents the C_4 parameter for a background collision. Assuming that the background gas consists mostly of air ($\sim 78\%$ N₂ and 20% O₂), we estimate $C_4 \approx 2.65 \times 10^{-57} \text{ Jm}^4$ [128, 130, 131] and $\mu_b \approx 24.82 \text{ a.u.}$ The Langevin rate can be obtained from the number of jumps n_j observed during a time t , given by $\eta_L = n_j / (tN - t)$. On average, we measure $n_j \approx 8 \pm 1$ over a period of $t = 200$ s, resulting in $\eta_L = (6.66 \pm 0.83) \times 10^{-3}$. Using the ideal gas law $p = \rho_b k_B T$, where k_B is the Boltzmann constant and $T \approx 295$ K is the gas temperature in the vacuum chamber, we can estimate the background gas pressure to be $p < (1.6 \pm 0.2) \times 10^{-10} \text{ mbar}$. Although this pressure estimation aligns with the readings from the ion pump ($p \leq 1 \times 10^{-10} \text{ mbar}$), it appears to be too high to prevent melting events in large ion crystals during typical experimental runs.

As a result, a second baking process was conducted at the end of 2020 to improve the vacuum conditions (see Figure 1.5). However, it was observed that the vacuum quality began deteriorating again in the following months. Subsequently, in 2022, it was discovered that the primary full-metal valve used to connect the vacuum chamber to an external turbo-pump was leaking. To address this issue, a second valve was added in front of the existing one. Since the pressure readings at the ion pump steadily decreased after the introduction of the second valve we believe that no further leaks should be present in the setup. Nevertheless, due to contamination of the vacuum another activation of the getter element is necessary.

6.2 TRAP FREQUENCIES MEASUREMENT

To characterize the Paul trap and assess the impact of the HV rods on the crystal geometry, a single ion's motion is excited using a radio-frequency field. The RF field is supplied by a frequency generator capacitively connected to a pair of compensation electrodes for inducing motion in the x' direction, or

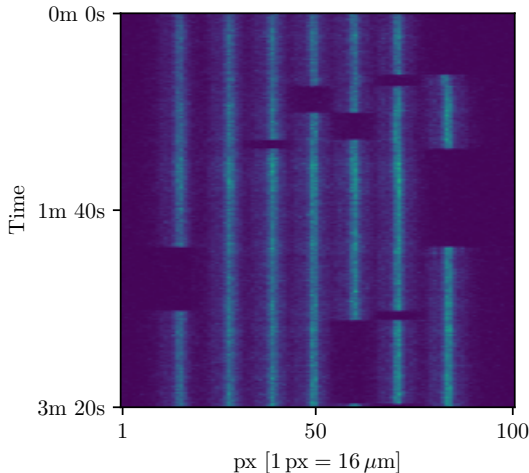


FIGURE 6.2: Ions hopping rate. We keep one of the ions that compose a 7 ions chain in a dark state while counting the number of hops in $t = 200$ s. We find that in total the ion chain undergoes collisions with background gases ~ 8 times.

to a pair of HV electrodes for exciting motion in the y' direction as shown in Fig. 5.3.

By scanning the applied frequency, we observe when the ion appears blurred on the camera or being expelled from the trap, noting down the resonant frequency. Since the compensation electrodes used for these measurements align with the imaging system, detecting motion in the x' direction is more challenging compared to the y' direction. To address this, we apply radio-frequency amplitudes of $5\text{--}10$ V_{pp} in the x' direction but as little as $0.1\text{--}1$ V_{pp} in the y' direction.

To investigate the radial frequency splitting induced by the HV electrodes, similar measurements are performed while varying the voltage U^{HV} applied to these electrodes as shown in Fig. 6.3. It is worth noting that although motion in the y' direction is more discernible, accurately measuring the trapping frequencies in this direction becomes increasingly difficult due to the anti-confining effect of the HV electrodes. At a voltage of $U^{\text{HV}} \sim -800$ V, the ions are prone to expulsion from the trap, leading to larger errors in the measured trap frequency.

The frequencies in the x' and y' directions are given by Eq. (2.16), were we defined an additional stability parameter a_{HV} for the field generated by the HV electrodes. Nevertheless, this parameter does not take into account

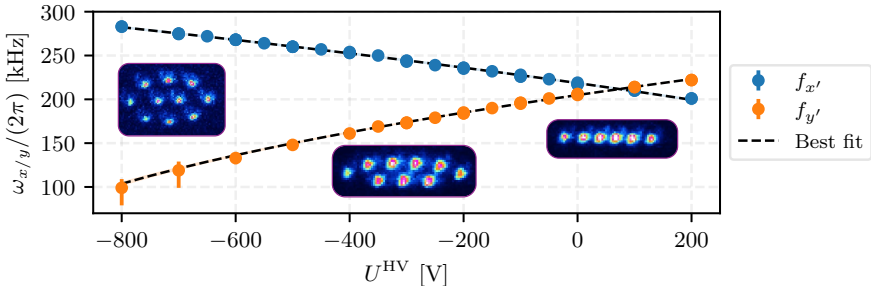


FIGURE 6.3: Measured trapping frequencies at various voltages U^{HV} applied to the HV electrodes. In the insets, associated crystal configurations (not to scale).

experimental defects in the trap which would lead to $\omega_{x'} \neq \omega_{y'}$ at $U^{HV} = 0$. In order to take this effect into account, we can introduce an additional voltage offset term U^{off} to Eq. (2.14) as :

$$a_{HV} = \frac{4e(U^{HV} - U^{off})\alpha_x^{HV}}{m\Omega_{RF}^2}. \quad (6.1)$$

In Fig. 6.3 are shown the trapping frequencies at different voltages U^{HV} applied to the HV electrodes. We fit Eq. (2.16) using the modified definition of a_{HV} to our data (dashed line in Fig. 6.3), finding $U^{off} = 73.3 \pm 2$ V and $\alpha_x^{HV} = 711 \pm 13$ m $^{-2}$ and $\alpha_y^{HV} = -695 \pm 8$ m $^{-2}$ in accordance to our initial assumption $\alpha_x^{HV} = -\alpha_y^{HV}$ and $\alpha_z^{HV} \approx 0$.

6.2.1 Axial trapping frequencies

In order to measure the axial trapping frequencies ω_z , we vary the voltage U^{DC} applied to the endcap electrodes (see Fig. 5.2) as shown in Fig. 6.4 a). Using Eq. (2.7) and assuming that $q_z \approx 0$ we find $\alpha_{z,z}^{DC} \approx 1 \times 10^4$ m $^{-2}$.

6.2.2 Control of the radial confinement

The radial trapping frequency $\omega_{x/y}$ can be controlled tuning the radio-frequency amplitude supplied to the trap. The trap drive generator provides a signal at $\Omega_{RF} = 2\pi \times 5.84$ MHz with amplitude -10 dB. This signal can be further tuned as shown in Fig. 5.4 by controlling a variable voltage attenuator

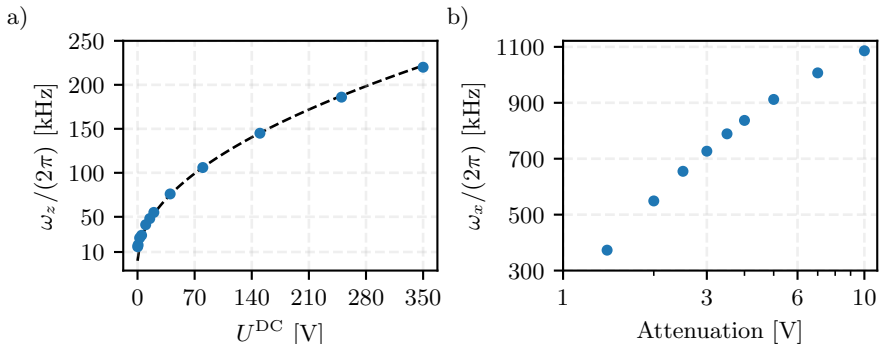


FIGURE 6.4: a) Axial trapping frequency ω_z at various endcaps voltages U^{DC} . b) Tunability of radial confinement ω_x at various attenuation levels of the VVA connected to the radio-frequency source.

(VVA). Fig 6.4 b) shows the radial trapping frequencies attainable in our Paul trap for various VVA voltages.

At 10 V the VVA provides little to no attenuation of the radio-frequency signal. Although our frequency generator and amplifier are able to source higher power, we noticed that due to heating of the metallic components that compose the Paul trap, trapping frequencies higher than 1.1 MHz are unattainable. This phenomenon is likely attributed to potential expansion of certain metal components within the trap, causing a shift in the total capacitance and altering the trap's impedance. Consequently, this effect reduces the effectiveness of our impedance matching done using an helical resonator, limiting its quality factor and, in turn, the total radio-frequency power circulating inside the trap.

Nonetheless, as previously emphasized in this thesis, our primary focus lies in exploring the interplay between the Paul trap and optical tweezers. Therefore, the trap is typically operated at a radial frequency of $\omega_x \sim 2\pi \times 500$ kHz.

6.3 MAGNIFICATION OF THE OPTICAL SYSTEM

To perform micromotion compensation in the radial direction and estimate the optical tweezers' shape, it is crucial to determine the total magnification of the optical system. By characterizing the trapping frequencies at different endcap voltages, we can accurately assess the axial equilibrium position of an ion chain. Knowing that the CCD camera³ used for imaging has a pixel

³ Andor iXon ultra 897

size of $L_{\text{px}} = 16 \mu\text{m}$ we can relate the distances between the ions' equilibrium positions measured on the camera with the expected theoretical ones.

For a linear chain composed of N ions, analytical expressions for equilibrium positions can be derived for $N = 2$ and $N = 3$, while higher values require numerical calculations [87]. The equilibrium position of a two- $^{174}\text{Yb}^+$ ion chain is reached when trapping force is equal to the Coulomb repulsion:

$$\frac{m_{174}\omega_z^2 d_2}{2} = \frac{e^2}{4\pi\epsilon_0 d_2^2}, \quad (6.2)$$

where ω_z represents the axial trapping frequency, and d denotes the inter-ion spacing.

We acquire the equilibrium position for a N -ions chain with $N = 2, 3, 5$ at $\omega_z = 2\pi \times 29.1 \pm 0.5 \text{ kHz}$. The expected ions distance in the case of a two-ions chain is $d_2 = 36.29 \pm 1.17 \mu\text{m}$. For $N = 3$ instead, we find $d_3 = 31.02 \pm 0.36 \mu\text{m}$. However, for $N > 3$ the inter-ion distance varies among the ions. In the case of $N = 5$ we obtain $\mathbf{d}_5 = [d_{1,2}, d_{2,3}, d_{3,4}, d_{4,5}] = [26.52 \pm 0.30, 23.67 \pm 0.27, 23.67 \pm 0.27, 26.52 \pm 0.30]$ with $d_{i,j}$ the distance between ions i and j .

After Doppler cooling, we capture images of $N = 2, 3, 5$ ion crystals and fit Gaussian functions to determine the equilibrium positions. The fitting yields $d_2^{\text{CCD}} = 19.00 \pm 0.10 \text{ px} \sim 304.2 \pm 1.6 \mu\text{m}$, $d_3^{\text{CCD}} = 16.20 \pm 0.10 \text{ px} = 258.9 \pm 1.6 \mu\text{m}$, and $\mathbf{d}_5^{\text{CCD}} = [13.7, 12.4, 12.3, 13.9] \pm 0.1 \text{ px} = [219.7, 198.5, 196.0, 221.9] \pm 1.6 \mu\text{m}$. Comparing these values with the theoretical ones gives us a magnification factor:

$$M = d_i^{\text{CCD}}/d_i = 8.3 \pm 0.1. \quad (6.3)$$

6.4 MICROMOTION COMPENSATION

Stray electric fields can shift the ions equilibrium position outside the radio-frequency null zone. This effect becomes particularly noticeable in the radial direction when trapping frequencies are low, as the relative strength of the stray electric fields compared to the trap confinement field becomes more significant.

To compensate for this effect, we track the ions' position when strongly confined at $\omega_x \approx 2\pi \times 1 \text{ MHz}$ and compare it with the equilibrium position at lower frequencies. With a magnification factor $M \approx 8.3$ and pixel size $L_{\text{px}} = 16 \mu\text{m}$ we can measure the shift in equilibrium position using the CCD camera with $\approx 2 \mu\text{m}$ precision. We observe a vertical displacement in the y' direction at low radial trapping frequencies, which we compensate for using the HV electrodes.

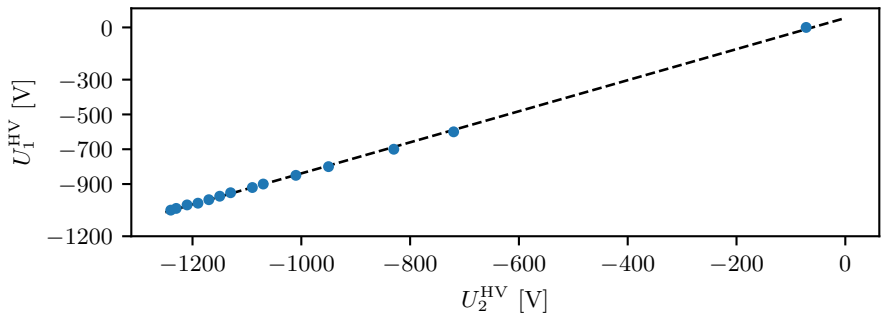


FIGURE 6.5: Voltage offset between the top (HV_1) and bottom (HV_2) pairs of HV electrodes necessary for compensation of radial micromotion. Here, we assumed one of the pairs to have the correct distance from the center $d_1^{\text{HV}} = 6 \text{ mm}$.

If the distance $d^{\text{HV}} = 6 \text{ mm}$ (see Fig.5.3) between both HV electrodes from the center of the trap were the same, the correction factor would be a global offset voltage V_{off} applied to both pairs of electrodes. However, to maintain the ions in the same position when varying U^{HV} , we must adjust this correction factor for each HV voltage combination. This effect can be explained by assuming that a pair of HV electrodes is positioned at a distance $d_{\text{HV}} \neq 6 \text{ mm}$. In Fig. 6.5 we present the combination of voltages U_1^{HV} and U_2^{HV} necessary for micromotion compensation. By imposing that the equilibrium position of the ions remains the same at all voltages, we can extrapolate the distance offset between the upper (1) and lower (2) HV electrodes as follows:

$$\frac{U_1^{\text{HV}}}{(d_1^{\text{HV}})^2} = \frac{U_2^{\text{HV}} + V_{\text{off}}}{(d_2^{\text{HV}})^2}. \quad (6.4)$$

The equation was fitted as shown in Fig.6.5 assuming $d_1^{\text{HV}} = 6 \text{ mm}$. From the fit we can extract the angular coefficient $(d_1^{\text{HV}})^2 / (d_2^{\text{HV}})^2$ from which we find $d_1^{\text{HV}} = 6.35 \pm 0.03 \text{ mm}$ and $V_{\text{off}} = 60.4(7) \text{ V}$. This indicates that the relative distance between the rods deviates by approximately $\approx 0.3 \text{ mm}$ from the ideal trap design.

6.5 SPATIAL LIGHT MODULATOR

In order to generate and control optical tweezers, we use an SLM⁴ having a resolution of $N_x \times N_y = 1272 \times 1024$ pixels and an effective area of

⁴ Hamamatsu LCOS-Spatial Light Modulator mod. X13138-02

$\Delta_x \times \Delta_y = 15.9 \times 12.8$ mm. The SLM offers a 98% light utilization efficiency and a phase quantization up to 8 bits.

The operational principle of SLMs is based on Fourier optics. An incident beam propagates through the LCD screen of the SLM. Depending on the alignment of the liquid crystals, it is possible to control the imprinted phase ϕ for each pixel of the SLM. This process is depicted in Fig. 6.6 where an incident Gaussian beam described by an electric field E_0 acquires a phase $\phi(x, y)$ depending on the position of incidence of the light on the SLM surface. The SLM acts as a rectangular aperture for the incident light. We can write the equation for the beam right after the reflection by the SLM as:

$$E_{\text{SLM}} = E_0(x, y) e^{i\phi(x, y)} \Pi \left[\frac{x}{\Delta_x}, \frac{y}{\Delta_y} \right], \quad (6.5)$$

where we introduced the two dimensional rectangle function Π to take in account the finite size of the SLM surface.

After reflection from the SLM the field propagates up to the first lens as shown in Fig. 6.6. Under the Fresnel approximation the field at the lens focus f is given by:

$$E(x', y') = \mathcal{F} \left[E_0(x, y) e^{i\phi(x, y)} \Pi \left[\frac{x}{\Delta_x}, \frac{y}{\Delta_y} \right] \right] \Big|_{\frac{x'}{\lambda f}, \frac{y'}{\lambda f}}, \quad (6.6)$$

where $\mathcal{F}|_{f_1, f_2}$ denotes the Fourier transform evaluated at frequencies f_1 and f_2 . The field intensity in the focal plane will then be $I(x', y') \propto |E(x', y')|^2$. The size of the reconstructed optical image at the focal plane $L_x \times L_y$ is given by:

$$L_{x/y} = N_{x/y} \frac{f\lambda}{\Delta_{x/y}}. \quad (6.7)$$

By properly controlling the phase ϕ of the SLM it is possible to generate arbitrary field intensities at the focus of the lens after the SLM. Finding the optimal phase pattern is not as trivial as doing an inverse fourier transform of the desired $E(x', y')$, in fact the Fourier transform is not unique giving arbitrary phases $\phi(x, y)$ and fields $E_0(x, y)$.

6.5.1 Searching for optimal phase patterns

Although we have full control of the phase ϕ we cannot easily change the initial field shape at the SLM. Consequently, the search for an optimal pattern is typically conducted using iterative processes that involve constraining the

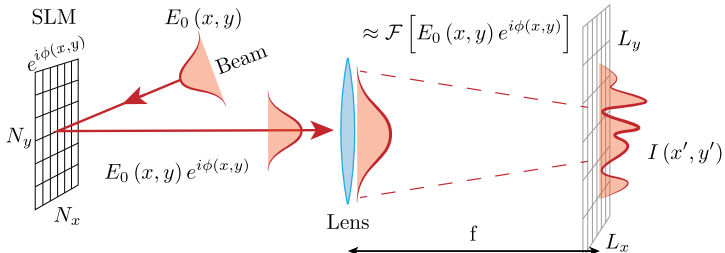


FIGURE 6.6: Schematic representation of an SLM system. An incident laser beam hits the SLM surface (left side) acquiring a phase modulation $e^{i\phi(x,y)}$ depending on the point of incidence. After propagation through a lens the desired intensity pattern is reconstructed at the focal plane.

field shape $E_0(x, y)$ at the SLM plane (Fourier plane) and the desired field $E(x', y')$ at the imaging plane.

The Gerchberg–Saxton (GS) [132] algorithm is the most commonly used method for this purpose. To generate uniform arrays of optical tweezers, the algorithm has been further enhanced with the weighted Gerchberg–Saxton (wGS) technique [133]. This algorithm accounts for effects caused by the finite phase resolution of SLMs by introducing a penalty for non uniform phase patterns in order to avoid the generation of intensity speckles. These speckles arise when adjacent pixels exhibit phase singularities at their interface or when the phase shift between two neighboring pixels is close to π . Since we lack control over the alignment of the nematic liquid crystal at the pixel's interface, the laser field must follow these discontinuities or phase shifts, leading to undesired dark spots in the final intensity distribution $I(x', y')$.

Another noteworthy algorithm is the Mixed-Region Amplitude Freedom (MRAF) algorithm [134]. This approach involves the use of two distinct intensity regions: a signal region and a noise region. The noise region, an unconstrained intensity zone, is essential for the algorithm to optimize the quality of the intensity pattern in the signal region. While the MRAF algorithm achieves remarkably accurate intensities, it comes at the cost of wasting some laser power in the noise region.

For the scope of this thesis we developed a software suite⁵ used for controlling a single tweezer necessary for first alignment to the ions position. In the future we plan to use the wGS or MRAF algorithm for the generation of multiple optical tweezers.

⁵ SLM controller

6.5.2 SLM efficiency

The phase $\phi(x, y)$ imposed by the Spatial Light Modulator (SLM) is subject to certain experimental constraints. Specifically, the phase is encoded as an 8-bit integer value in the range of [0, 255]. These values are represented as gray levels in an 8-bit image, where a black pixel corresponds to a phase of 0, and a white pixel corresponds to a phase of 255.

Depending on the laser wavelength, it is necessary to map this range to the interval [0, 2π], i.e., determine the integer value ϕ_N that corresponds to a phase shift of 2π . The value of ϕ_N can be obtained through phase shift calibration or be provided by the manufacturer in the form of a look-up table (LUT). In our case, the phase modulation correction for the SLM was provided by the manufacturer, as the SLM itself does not allow for fine adjustment of pixels voltages. The mapping between gray levels and phase shifts are depicted in Fig 6.7 a).

Moreover, it is evident that the phase range [0, 2π] is encoded with an 8-bit resolution. The effect of phase discretization can be characterized by using the SLM to impose a phase grating (or blazed grating) while varying its lines density. As the lines per millimeter (lp/mm) of the grating increase, the diffraction efficiency of the SLM decreases. This observation can be explained by considering that the number of pixels within a given spacing is finite, while the phase must vary by 2π between two ridges of the grating. In other words, the smaller the pitch of the grating, the fewer discrete phase levels are available within the range, resulting in a reduction in diffraction efficiency. The diffraction efficiency of the SLM utilized in our setup is illustrated in Fig 6.7 b).

The efficiency of Spatial Light Modulators (SLMs) is limited by a phenomenon known as the “0-th order” even when lower lp/mm values are used. This limitation arises due to the presence of dead zones between pixels on the SLM surface. These dead zones correspond to areas where the nematic liquid crystal cannot align in a defined direction because the electric field between adjacent pixels is not well defined. This results in the generation of a random and uncontrollable phase for a portion of the laser light reflected by the SLM. As a consequence, this scattered light behaves as background or stray light when interacting with a passive metallic surface.

In an optical system aligned with the center of the SLM, the intensity of the 0-th order light will appear on the optical axis. This means that, in our case, the light will be focused in close proximity to the location of the ions, necessitating the minimization of its effects on the ions. One option to address this issue is to impose a virtual Fresnel lens pattern on the SLM, thereby shifting the focus of the pattern generated by the SLM. By assuming

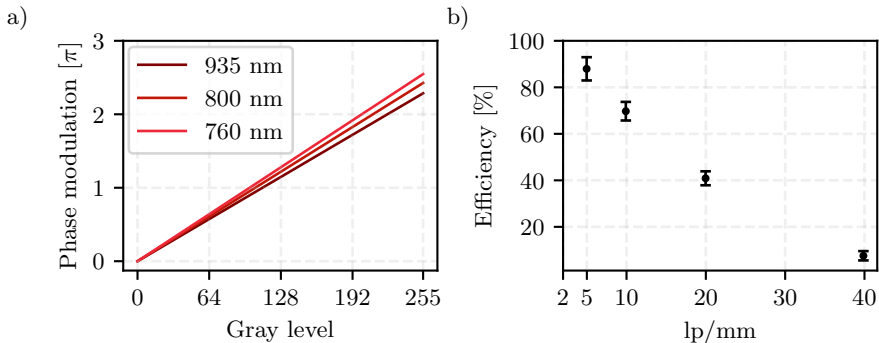


FIGURE 6.7: a) Phase calibration in units of π for 760 nm, 800 nm and 935 nm. The value for 935 nm has been extrapolated from the data provided by the manufacturer as the SLM is not rated to work in that wavelength range. b) SLM diffraction efficiency measured by generating a blazed grating in the x direction of the SLM the curve was measured using 800 nm light, figure adapted from [135].

that the pattern is in the focus of the real and virtual optical system at the location of the ions, the 0-th order light will manifest as a global background light. This approach can be viable when using laser light that is far detuned from any of the internal transitions in the ions.

However, a more conventional approach is to shift the intensity pattern by superimposing a global blazed grating on the surface of the SLM. This way, both the 0-th order light and the desired intensity pattern are shifted at the imaging plane. By carefully controlling the positioning of the ions and this pattern, it becomes possible to prevent the 0-th order light from impinging on any of the ions.

6.5.3 Correction of optical aberrations

As shown in Eq. (2.52) under the harmonic approximation, the trap frequency of optical tweezers is highly dependent on the size of the waist of the optical beam. Consequently, our goal is to design an optical system that can generate diffraction-limited optical tweezers. However, achieving this objective is not a straightforward task due to the potential introduction of imperfections by the optical elements preceding and following the SLM. These imperfections can result in optical aberrations at the focal point where the ions are positioned. Effectively compensating for these aberrations in practical terms presents a significant challenge. Nevertheless, it has been demonstrated [136] that it is

possible to discover the correct phase shift pattern using the SLM. In order to do so we aim to generate a phase pattern that can effectively cancel out the aberrations introduced by the physical optical elements.

The optimization procedure is depicted in Fig. 6.8. To initiate the optimization process, we partition the Spatial Light Modulator (SLM) into sub-zones, also known as super-pixels. We apply a phase grating to a designated reference zone (indicated as “ref.” in Fig. 6.8 b)), which effectively displaces the light (E_1) reflected from that particular zone away from the zero-th order component. Throughout the optimization process, the phase pattern of the reference zone remains fixed.

Next, we activate a second zone called the probe (indicated by “prob.” in Fig. 6.8 b)) zone by implementing a similar grating phase pattern but with a variable global offset. Under normal conditions without optical aberrations, the light scattered by both zones (E_1 and E_2) will exhibit phase coherence in the focal plane, leading to constructive interference at the first order location.

However, if optical aberrations are present, the intensity at the first-order location can be expressed as $I = E_1^2 + E_2^2 + 2E_1E_2 \cos(\Delta\phi)$, where $\Delta\phi$ represents the phase offset resulting from the aberrations within the system. In order to achieve constructive interference, we adjust the phase of the probe zone until the two optical paths coherently combine, yielding $\cos(\Delta\phi) = 1$. We record the phase correction required for the probe zone, deactivate it, and proceed with the same procedure for another probe zone.

By repeating this process iteratively for different probe zones, we can determine the phase corrections necessary to compensate for the aberrations introduced by the system. This approach allows us to progressively refine the phase patterns of the probe zones, improving the overall performance and coherence in the optical trapping system.

Figure 6.8 b) illustrates the outcome of the optimization process conducted on a second SLM⁶ using a third-party software⁷. This SLM is intended for future use in upgrading the experiment. Following the optimization procedure, the beam shape becomes more circular, significantly reducing the prominent optical aberrations present in the system. It is worth noting that the 0-th order component remains unaffected by the phase modulation introduced by the SLM.

To achieve the results depicted in Figure 6.8 b), we employed a CMOS camera⁸ to record the light intensity at the interference point. However, this same approach cannot be utilized for characterizing and compensating optical

⁶ Holoeye PLUTO-2.1-NIR-149, $\lambda = 1030$ nm

⁷ SLM suite

⁸ Sony IMX477R, Raspberry Pi High Quality Camera

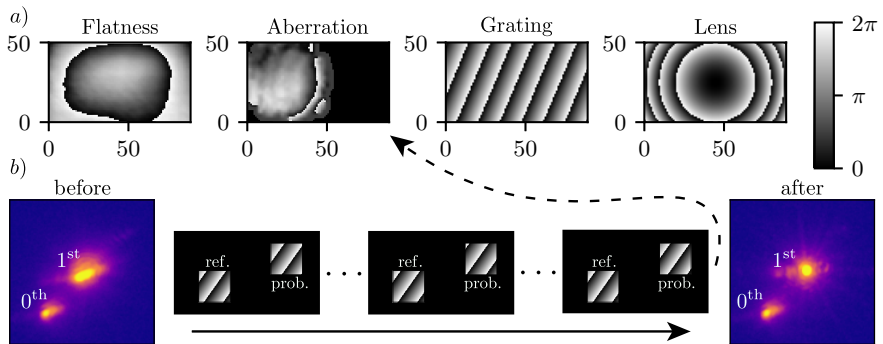


FIGURE 6.8: a) Various virtual optical elements that can be used to generate optical tweezers. The aberration correction pattern can be obtained by recording the interference between a reference zone and a probe zone at a specific point. b) The optimization algorithm is depicted schematically, showing the comparison between the appearance of the first-order spot before and after the correction has been applied.

aberrations in our setup due to the focal plane of the optical system being situated inside the vacuum chamber.

As a solution, we intend to employ a single ion as a probe to correct for optical aberrations. By measuring the AC-Stark shift induced on the internal levels of the ion [137] by the off-resonant light, we can obtain feedback on the intensity. The highly sensitive hyperfine qubit states in $^{171}\text{Yb}^+$ make them an ideal choice for this probing technique.

Since the complete characterization of the SLM surface necessitates around 800 probe zones, the entire procedure typically requires a few hours to be completed. However, this extended timeframe may introduce additional experimental challenges when probing the intensity of the optical tweezers using a single ion. To address this issue, we plan to implement a more efficient version of the correction algorithm [138] where the phase of various probe zones is varied simultaneously further speeding up the data acquisition process.

The combination of these techniques offers a promising pathway for optimizing the system, enabling faster characterization of the SLM surface and more efficient probing of the optical tweezers' intensity. This advancement brings us closer to realizing diffraction-limited optical tweezers and unlocking their full potential for various applications.

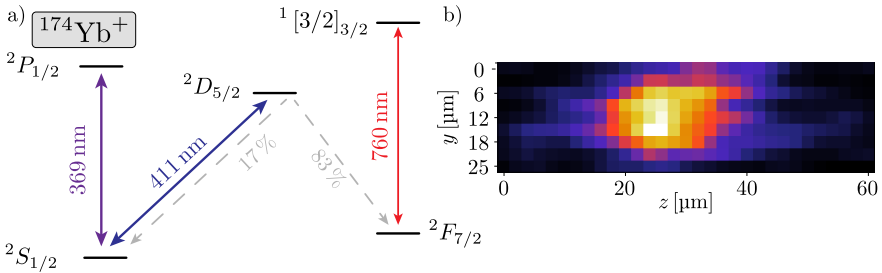


FIGURE 6.9: a) Relevant energy levels we consider when mapping the tweezer intensity shape with the ions. b) Tweezer intensity shape reconstructed by measuring the fluorescence intensity of one ion.

6.6 ALIGNMENT OF OPTICAL TWEEZERS

We perform a first alignment of optical tweezers on a single ion using 760 nm light. This wavelength, although different from the planned (800 nm) one is resonant with the internal $^2\text{F}_{7/2}$ to $^1[3/2]_{3/2}$ transition, simplifying the alignment procedure. We perform tweezers alignment using $^{174}\text{Yb}^+$ due to its simplified energy levels structure.

Fig 6.9 shows the relevant energy levels used for this procedure. We first pump the ion to the $^2\text{D}_{5/2}$ state by resonantly driving the 411 nm transition from the $^2\text{S}_{1/2}$ state. After ≈ 7.2 ms the ion will decay with 83 % probability to the $^2\text{F}_{7/2}$ state with a lifetime of ≈ 1.6 yrs. If the ion is illuminated by the 760 nm tweezers it will get excited to the $^1[3/2]_{3/2}$ state from which it can spontaneously decay to the $^2\text{S}_{1/2}$. Once in the $^2\text{S}_{1/2}$ ground state we can detect the ions through the cyclic $^2\text{S}_{1/2} \rightarrow ^2\text{P}_{1/2}$ transition. In this way, an ion not inside the tweezers region will remain trapped in the $^2\text{F}_{7/2}$ state appearing dark, while an ion in the presence of a tweezers will appear bright.

We perform a first rough alignment keeping both 411 nm and 760 nm lasers on. We trap a crystal of ~ 5 ions and move the optical tweezers using a combination of blazed grating and Fresnel lenses. Once the tweezer hits one (or more) ion, this will undergo quantum jumps between the $^2\text{F}_{7/2}$ and $^2\text{S}_{1/2}$ states. Initially, we observe most of the ions jumping during the alignment procedure. To refine the alignment, we adjust the focus of the tweezers beam by modifying the Fresnel lens pattern or by moving the last lens outside the vacuum chamber (refer to Fig. 5.19). Once the alignment reaches a stage where only one ion in the chain remains brightly fluorescing, we proceed to scan the intensity profile of the tweezers by either displacing the tweezer

location using a blazed grating or by axially moving the ions through voltage adjustments on one of the endcaps.

Fig 6.9 b) displays the intensity shape of a single tweezer, mapped using the fluorescence emitted by a single ion and captured by the imaging system. Based on our measurements, we estimate the beam waist to be approximately $10\text{ }\mu\text{m}$. Further optimizing the optical tweezer proves challenging due to the narrowness of the $^2F_{7/2} \rightarrow ^1[3/2]_{3/2}$ transition and the instability of the laser system. Additionally, accurately estimating the intensity of the 760 nm laser is not possible, given the unknown quadrupole transition element. Consequently, while this preliminary alignment serves as a good starting point for refining the alignment of the 800 nm laser, we recognize the need to conduct a more precise characterization of the tweezer. Therefore, we plan to utilize the 935 nm transition, which allows for faster detection and has a well-known dipole transition element.

6.7 DARK IONS

During the process of trapping $^{174}\text{Yb}^+$ crystals, we observed the presence of various crystal defects which we attributed to unidentified charged particles (see Fig. 6.10 a)). Interestingly, these defects became apparent only after the loading phase, suggesting that the dark ions present were not simply different isotopes mistakenly trapped.

We found that the rate of dark ion formation strongly depends on the vacuum quality within the chamber. Normally we observed the appearance of one dark ion approximately every $\approx 10\text{ min}$, but this frequency increased to one dark ion every $\approx 1\text{ min}$ with the degrading of vacuum conditions. Furthermore, we noticed a striking imbalance between the rate at which ions go dark and the rate at which they return to a bright state. The likelihood of a dark ion returning to a bright state is extremely low, suggesting dark ion lifetimes of $\gtrsim 10\text{ min}$.

The most common sources of dark ions are ions trapped in the $^2F_{7/2}$ long-lived state or the presence of YbH^+ molecular ions. To eliminate the first possibility, we employed resonant excitation using a 760 nm laser to drive the $^2F_{7/2}$ to $^1[3/2]_{3/2}$ transition. We assessed our ability to pump ions out of the $^2F_{7/2}$ state by trapping crystals consisting of a few $^{174}\text{Yb}^+$ ions and completely transferring their population to the F state using the 411 nm transition. After the crystal appeared entirely dark, we used the 760 nm laser to pump the ions back to the $^2S_{1/2}$ state. This process, when executed within a short period of time, achieved approximately $\sim 100\%$ efficiency, effectively restoring fluorescence to all ions.

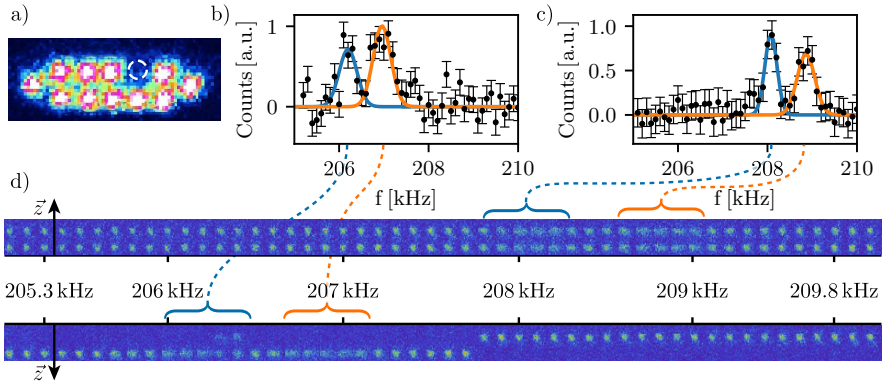


FIGURE 6.10: a) Two-dimensional crystal of $^{174}\text{Yb}^+$ showing a dark ion defect (dashed circle). b) Radio-frequency scan of resonant trap frequencies for a pure $^{174}\text{Yb}^+ - ^{174}\text{Yb}^+$ crystal and (c) for an irregular $^{174}\text{Yb}^+ - \text{YX}^{174}\text{Yb}^+$ crystal. For each applied RF signal we acquire an image of the two-ion crystal. The pure crystal shows two resonances (blue and orange squares) at $\sim 208.1\text{ kHz}$ and $\sim 208.9\text{ kHz}$ while the irregular crystal at $\sim 208.1\text{ kHz}$ and $\sim 208.9\text{ kHz}$. d) Stacked images of crystal dynamics at different RF frequencies. The two resonances of b) and c) appear visibly shifted.

YbH^+ molecular ions can undergo photodissociation when exposed to intense UV light with wavelengths $\lambda \sim 369\text{ nm}$ or $\lambda \sim 405\text{ nm}$ [139]. In an attempt to induce photodissociation in dark ions, we experimented with detuning the Doppler laser to 369.482 nm [139] and increasing its power. However, we did not observe any noticeable effect. We also made an attempt to induce photodissociation using a free-running diode laser operating at $\lambda = 405\text{ nm}$ [139] with power $P \sim 10\text{ mW}$, but this approach also yielded no significant results.

Given that the dark ions most likely did not correspond to YbH^+ , we proceeded to determine their mass through measurement. To do so, we loaded a two-ion crystal consisting of $^{174}\text{Yb}^+$ ions and compared the shift in the radial trapping frequency with a reference crystal comprising $^{174}\text{Yb}^+$ and $^{174}\text{YbX}^+$, where YX represents an unknown atomic species with mass Y . For a single $^{174}\text{Yb}^+$ ion, we denote the radial trapping frequency as $\omega_{x'/y'}$ and the axial trapping frequency as ω_z . The mixed-species two-ion crystal exhibits radial center-of-mass (COM) and stretch (STR) frequencies which can be determined using the following relation [140]:

$$\omega_{\text{COM},x'/y'} = \sqrt{-\frac{\mu + \mu^2 - \epsilon^2(1 + \mu^2) - a}{2\mu^2}}\omega_z, \quad (6.8)$$

$$\omega_{\text{STR},x'/y'} = \sqrt{-\frac{\mu + \mu^2 - \epsilon^2(1 + \mu^2) + a}{2\mu^2}}\omega_z, \quad (6.9)$$

with $\epsilon = \omega_{x'/y'}/\omega_z$, $\omega_{x'/y'}$, $\mu = (174 + Y)/174$ and:

$$a = \sqrt{\epsilon^4(\mu^2 - 1)^2 - 2\epsilon^2(\mu - 1)^2\mu(1 + \mu) + \mu^2(1 + \mu^2 - \mu)}. \quad (6.10)$$

To determine the resonant frequencies of the crystal we applied a 3 V_{pp} RF pulse for 500 ms to the HV electrodes. As the electric field cannot couple to the stretch mode, only the center-of-mass mode will be excited. We acquire the fluorescence signal using the camera and repeat the process 10 times for each frequency to mitigate errors through averaging. We start with a pure two- $^{174}\text{Yb}^+$ crystal. When the applied frequency is resonant with the center-of-mass mode the ions will appear blurred in the camera image as shown in Fig. 6.10 d).

To compare it with an impure crystal we maintain the 760 nm laser illuminating the ions while waiting for one of the ions to go dark. Remarkably, we observe that the center-of-mass mode of an impure crystal of $^{174}\text{Yb}^+ - \text{YX}^{174}\text{Yb}^+$, exhibits a lower resonant frequency compared to that of a pure $^{174}\text{Yb}^+ - ^{174}\text{Yb}^+$ crystal. To improve our ability to detect small changes and distinguish subtle differences, we gather the total number of fluorescence signals from the camera images taken outside the usual region where the ions are normally at rest. As the crystal undergoes oscillations, the fluorescence spreads beyond its usual boundaries, creating a noticeable peak in the count distribution (see Fig. 6.10 b) and c)). This allows us to capture a clearer and more pronounced signal of the crystal's behavior, increasing our sensitivity to detect even minor variations.

We determine the two resonant frequencies by analyzing and fitting the corresponding peaks. Our findings are presented in Fig. 6.11. We observe that the two center-of-mass frequencies exhibit a shift of approximately 2 kHz, transitioning from $\omega_{x'} = (208.9 \pm 0.2)$ kHz and $\omega_{y'} = (208.1 \pm 0.2)$ kHz to $\omega_{x'} = (207.0 \pm 0.2)$ kHz and $\omega_{y'} = (206.2 \pm 0.2)$ kHz. This frequency shift suggests the presence of a molecular ion with a total mass of $M \geq 174 + 8 \text{ a.m.u.}$, indicating a molecule that is heavier than anticipated.

Although our findings exclude the possibility of YbH^+ , precise determination of the molecular ion's mass remains elusive. More investigation on

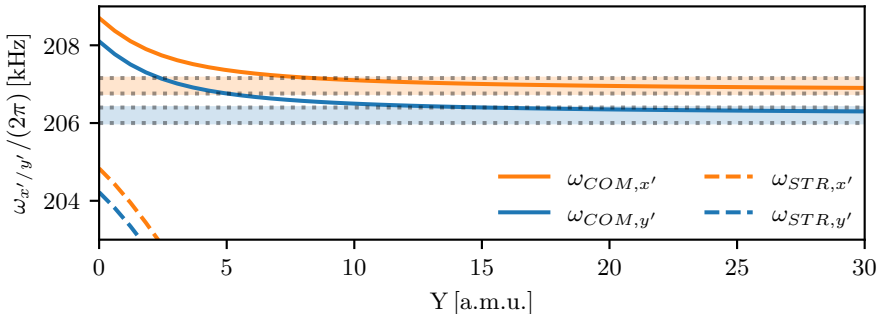


FIGURE 6.11: Radial modes frequency shift depending on the mass of the additional ${}^Y X$ element. The bands between dotted lines are obtained from the fit in Fig. 6.10 b) and c). The values obtained hint to $Y \geq 8$.

the nature of dark ions is still undergoing at the moment of writing. Enhancing our mass detection sensitivity can be achieved by increasing the axial confinement, further splitting apart the stretch and center-of-mass modes. Additionally, reducing the applied RF power can help minimizing the impact of power broadening enhancing our resonant frequency detection.

Nonetheless, the indication of an additional mass of at least 8 a.m.u. suggests a more complex molecular dynamics than previously anticipated, potentially involving the presence of heavier elements or more complicated molecular species within the vacuum chamber.

CONCLUSIONS AND OUTLOOK

In this thesis, we have extensively explored the challenges and advantages of combining optical tweezers with trapped ions. We provide a detailed account of the design and construction of our innovative setup for trapping one- and two-dimensional ion crystals. While the ultimate objective of controlling spin-spin interactions in trapped ions remains unattained within the scope of this thesis, we have successfully addressed the primary research questions outlined in section 1.4. The following conclusions can be drawn from our findings:

- Quantum computing and quantum simulations employing trapped ions stand to benefit significantly from the integration of optical tweezers. We have described how optical tweezers can exert mechanical forces on ions and, under specific conditions, achieve state-dependent optical forces. By employing far-detuned optical tweezers, it is possible to generate site-dependent trapping potentials, thus modifying the soundwave spectrum of the entire crystal. This effect, in combination with a global Raman beam, can enable the tuning of spin-spin interactions between ions, leading to a programmable quantum simulator.
- By leveraging the differential polarizability of specific states, we have shown how optical tweezers can be used to induce state-dependent forces on ions, opening up possibilities for engineering novel two-qubit gates in trapped ion systems. We propose two distinct types of such gates.

The first gate utilizes the combination of optical tweezers with oscillating electric fields. Not reliant on the Lamb-Dicke approximation, numerical simulations show that this gate could achieve high fidelity regardless of the number of trapped ions. Additionally, since the electric field exclusively couples to the center-of-mass mode, this quantum gate fidelity remains independent of the distance between the target ions.

The second quantum gate exploits the optical Magnus effect, observable in tightly focused laser beams, where strong field curvature at the beam focus induces polarization component splitting. We propose to utilize this effect to generate state-dependent forces orthogonal to the propagation direction of optical tweezers. This enables coupling to the axial confinement direction while addressing the ions from the radial

direction. This approach offers experimental advantages, as the radial direction typically provides greater optical access. Our simulations predict competitive gate fidelity while significantly simplifying the required optical setup. Unlike conventional state-of-the-art Mølmer-Sørensen gates that rely on interference between two different beam paths, the state-dependent forces in our proposed gates stem from properties inherent to the beam itself.

However, these new gates introduce additional experimental challenges. In particular, to achieve significant strength in state-dependent forces, optical tweezers must be focused close to the diffraction limit ($w_0 \approx 1 \mu\text{m}$). Furthermore, precise alignment ($\epsilon \leq 30 \text{ nm}$) of the optical tweezers is necessary.

- We present a novel experimental setup capable of generating two-dimensional ion crystals. By applying a DC electric field, we can tune the dimensionality of the crystal, surpassing the conventional one-dimensional ion chains and enabling the study of 1D-to-2D transitions in ion crystals. Optical tweezers provide the means to introduce slight perturbations to the trapping potential, thereby forcing the ions into specific configurations.
- We show our experimental progress in aligning an optical tweezer with a single trapped ion. This endeavor presents a significant challenge as the optical tweezer induces minimal perturbation to the strong trapping potential provided by the Paul trap, leaving the ion's position largely unaffected. Consequently, a precise optical alignment procedure had to be developed. We have successfully mapped the beam profile of the optical tweezer by correlating it with the collected fluorescence of a single ion. Furthermore, we have shown how optical aberrations in the system can be mitigated using iterative algorithms that maximize the interference of the beam in a specific position.

7.1 FUTURE UPGRADES

Future upgrades to our experimental setup are crucial for further advancements in this field. First and foremost, the lifetime of ion crystals in our current setup falls short of expectations due to suboptimal vacuum conditions, limiting long-term trapping. The primary factor affecting the crystal's lifetime is the rate at which ions transition to a dark state. We are actively working to understand the underlying molecular dynamics responsible for this phenomenon, but currently, we have only been able to establish a lower bound on the mass of the molecular ion present in our trap. Moreover, the

proportion of ions transitioning to a dark state is strongly influenced by the quality of the vacuum.

Only later in the experiment we identified a leaky valve as one of the primary causes for this issue. Nonetheless, the identification of the problem is a positive development. Upgrading the vacuum system holds the potential to enhance crystal lifetimes, thereby expediting the data acquisition process. This upgrade is deemed necessary before proceeding with further alignment of optical tweezers.

The following alignment step will involve compensating for optical aberrations using trapped ions to determine the optimal phase pattern for SLM compensation. Nevertheless this procedure will require a direct feedback from the ions. Achieving a reasonably well-aligned system is crucial for inducing a significant AC-Stark shift on the hyperfine qubits of $^{171}\text{Yb}^+$ and using this effect as a benchmark for further optimization. Our experiments have demonstrated the generation of a beam waist $w_0 \approx 10\text{ }\mu\text{m}$ using 760 nm light. To attain a higher tweezers frequency, we plan to incorporate a 1030 nm laser with a peak power of $\sim 40\text{ W}$. Consequently, upgrading the setup to incorporate safety measures for the high-power laser is necessary and underway at the moment of writing. Additionally, significant modifications will be made to the optical setup, as it was originally designed for a wavelength of 800 nm. Currently, the new optical setup is in the preparation phase, and the aberration correction procedure has been successfully demonstrated using a CMOS camera.

Additionally, in order to reach the required conditions for observing spin-spin interactions, it is necessary to attain sub-Doppler cooling of one- and two-dimensional ion crystals. This objective is expected to be accomplished in the near future, as the requisite laser system components have already been constructed [124]. Finally, a crucial step in this endeavor involves characterizing the Raman laser system. A significant milestone in this characterization process would be the realization of two-qubit gates on trapped ions.

Simultaneously, a second experimental setup is being developed, focusing primarily on the utilization of UV optical tweezers to experimentally implement the two proposed quantum gates in chapter 3 and 4 of this thesis. As the UV tweezers will operate closer to resonance compared to the IR tweezers, a key experimental challenge in the new setup will be generating Laguerre-Gaussian beams to suppress off-resonant scattering rates.

In conclusion, the expanding applications of optical tweezers have become evident in recent years. Having possible application to both the fields of quantum computing and quantum simulations. With the planned upgrades to our experimental setup, we anticipate that it will soon be feasible to demonstrate the shift in sound-wave spectra resulting from the presence of

optical tweezers. This achievement would represent a significant experimental breakthrough. Subsequently, by employing a global Raman beam, we expect to showcase the generation of spin-spin interactions among the initial few ions.

Additionally, the implementation of UV state-dependent optical tweezers holds the potential for novel architectures of two-qubit gates, addressing the existing challenge of multi-qubit fidelity in state-of-the-art quantum computers. Optical tweezers offer a promising solution to overcome these experimental difficulties and drive advancements in the field of quantum computing with trapped ions.

S U M M A R Y

In this thesis, we explore the integration of ion trapping technology with optical tweezers. We commence by providing an overview of ion trapping theory and the engineering of a Paul trap capable of confining two-dimensional ion crystals. Subsequently, we describe the engineering of effective spin-spin interactions in such a system through the utilization of a global Raman scheme. The strength of these interactions relies heavily on the collective motional vibrations of the ions within the crystal. By employing optical tweezers, we can generate localized trapping potentials on specific ions, thereby modifying the collective vibrational modes and altering the spin-spin interaction pattern among the ions. Additionally, we introduce the theory of polarizability and present an estimation method for evaluating the strength of the additional trapping potential introduced by optical tweezers.

Furthermore, we propose a novel approach to implementing a two-qubit gate in trapped ions by leveraging state-dependent optical tweezers combined with oscillating electric fields. Our proposal eliminates the reliance on the Lamb-Dicke regime and mitigates phase noise issues associated with laser beams, simplifying the experimental challenges compared to current state-of-the-art techniques. We characterize the performance of the two-qubit gate through numerical simulations and discuss the associated advantages and challenges.

Another promising application of optical tweezers in quantum computing involves exploiting the optical Magnus effect. By tightly focusing a laser beam, the field curvature induces a splitting of polarization components by 2λ . This effect allows us to generate spin-dependent forces on trapped ions. By modulating the intensity of the tweezers, we can excite the ions' motion in phase-space, effectively implementing a two-qubit gate. Notably, the force exerted by the tweezers is perpendicular to the direction of propagation. Through numerical simulations, we assess the performance of the proposed gate and identify key sources of infidelity.

Both theoretical proposals demonstrate the feasibility of achieving competitive two-qubit gate fidelities while mitigating experimental challenges, offering significant advancements in the field of quantum computing with trapped ions.

In terms of experimentation, we present the design and construction of a novel experimental setup that combines optical tweezers with trapped ions. We provide a detailed description of the Paul trap and the required laser systems utilized in the experiment. Furthermore, we thoroughly characterize

the setup and investigate the effects of experimental imperfections on the trap. Additionally, we showcase the initial alignment of an optical tweezer on a single trapped ion. This alignment is achieved using an optical tweezer resonant at 760 nm with one of the quadrupole transitions in $^{174}\text{Yb}^+$. By leveraging the benefits of resonant light, we map the beam shape using a single ion. However, further enhancements are required, as the optical tweezers exhibit aberrations and possess a waist of approximately $w_0 \approx 10 \mu\text{m}$. Therefore, we propose implementing an active correction of the tweezers' shape using an iterative process on a SLM.

Finally, in the conclusions and outlook section, we outline the subsequent steps necessary for optimizing the beam shape of the tweezers and discuss ongoing and planned upgrades to the experimental setup.

A

TENSOR CALCULUS

The tensor polarizability described in Chapter 2 is based on tensor algebra. This section will cover the basis tensor operations needed to obtain the equations defined in Sec. 2.3.1.

We start by defining the three orthogonal versors in the spherical basis as \hat{e}_q with $q = -1, 0, 1$. The matrix for a change of basis from Cartesian to spherical is:

$$\mathcal{T}_{\text{car} \rightarrow \text{spher}} = \begin{bmatrix} \frac{-1}{\sqrt{2}} & \frac{i}{\sqrt{2}} & 0 \\ 0 & 0 & 1 \\ \frac{1}{\sqrt{2}} & \frac{i}{\sqrt{2}} & 0 \end{bmatrix}. \quad (\text{A.1})$$

The usual scalar product between two vectors in a spherical basis is:

$$\mathbf{X} \cdot \mathbf{Y} = \sum_m X^m Y_m = \sum_m X_m Y^m = \sum_m (-1)^m X_m Y_{-m}, \quad (\text{A.2})$$

where $m = -1, 0, 1$. Notice that when using a spherical basis we have to keep in mind the clear distinction between covariant and contravariant vectors as the basis versors obey the following orthogonality relations:

$$\mathbf{e}_{m_1} \cdot \mathbf{e}^{m_2} = \mathbf{e}_{m_1} \cdot \mathbf{e}_{m_2}^* = \delta_{m_1, m_2}. \quad (\text{A.3})$$

Combining Eq. (A.2) with Eq. (A.3) for a general vector \mathbf{V} expressed in Cartesian coordinates $V_m = \hat{e}_m \cdot \mathbf{V}$ we obtain:

$$\mathbf{V} = \sum_m (-1)^m V_m \mathbf{e}_m = \sum_m V_m \mathbf{e}_m^*. \quad (\text{A.4})$$

The definitions obtained so can be extended to vector operators that can be expressed in spherical coordinates as shown in Eq. (A.4) with $V_m \rightarrow \hat{V}_m$.

A.1 TENSORS OPERATORS

So far we limited our treatment to one dimensional (vector) objects. We can extend these definitions to other dimensions greater than one known as spherical tensors.

A spherical tensor is a mathematical object used to describe physical quantities that exhibit rotational symmetry. It is a generalization of a tensor to the spherical coordinate system, which is suitable for describing phenomena that are invariant under rotations in three-dimensional space as, for example, the transition dipole elements involved in the polarizabilities calculations of Sec. 2.3.1.

It is often useful to express tensors in terms of their *irreducible representations*. Each rank-K irreducible tensor consists of $2K + 1$ components, corresponding to different orientations in space.

An irreducible tensor operator transforms under rotations of coordinate systems the same way as the eigenfunctions of the angular momentum would do:

$$\begin{aligned} \left[J_z, T_M^{(K)} \right] &= \hbar M T_M^{(K)} \\ \left[J_{\pm}, T_M^{(K)} \right] &= \sqrt{(K \pm M + 1)(K \mp M)} T_M^{(K)}, \end{aligned} \quad (\text{A.5})$$

where J_z, J_{\pm} are respectively the z-rotation operator and the ladder operators on the angular-momentum eigenstates.

Analogous to what we did for vectors we can define a scalar product between irreducible tensors of rank K as :

$$\begin{aligned} \left(R^{(K)} \cdot T^{(K)} \right) &= \sum_M R_M^{(K)} \left(T_M^{(K)} \right)^{\dagger} = \sum_M R_M^{(K)} T_{(K),M} \\ &= \sum_M (-1)^{-M} R_M^{(K)} T_{(K),-M}, \end{aligned} \quad (\text{A.6})$$

where the M index runs on the $-M < K < M$ components of the tensor and we have defined the covariant component of the tensor $T^{(K)}$ as $T_{(K),M}$ in analogy to the components of a vector operator. The phase in Eq. (A.6) was chosen such that it coincides with the usual one used for spherical harmonics.

Starting from two tensors $X^{(K_1)}$ and $X^{(K_2)}$ of rank K_1 and K_2 we can define an *irreducible tensor product* as:

$$T_M^{(K)} = \sum_{m_1, m_2} C_{K_1, m_1, K_2, m_2}^{K, M} X^{(K_1)} Y^{(K_2)}, \quad (\text{A.7})$$

where $C_{K_1, m_1, K_2, m_2}^{K, M}$ are the Clebsch–Gordan coefficients. The irreducible tensor product is often referred to as $T^{(K)} \equiv \{X^{(K_1)} \otimes Y^{(K_2)}\}_K$. The product of two irreducible tensors is generally not irreducible, we can however decompose the product as a sum of irreducible tensors $T^{(K)}$ as:

$$X_{m_1}^{(K_1)} Y_{m_2}^{(K_2)} = \sum_{K=|K_1-K_2|}^{K_1+K_2} C_{K_1, m_1, K_2, m_2}^{K, M} T_M^{(K)}. \quad (\text{A.8})$$

A.2 IRREDUCIBLE TENSORS IN SECOND ORDER PERTURBATION THEORY

Following the derivations of Chapter 2 in order to evaluate the second order AC Stark shift we have to compute the objects of the following form [72]:

$$\frac{\hat{H}_{\text{AC}}}{E_i - \hat{H}_0 \pm \omega} = (\boldsymbol{\epsilon} \cdot \mathbf{d})^* \frac{1}{E_i - \hat{H}_0 \pm \omega} (\boldsymbol{\epsilon} \cdot \mathbf{d}), \quad (\text{A.9})$$

Where $\boldsymbol{\epsilon}$ and \mathbf{d} are two rank-1 tensors. Expanding the dot product in a spherical basis we obtain:

$$\frac{\hat{H}_{\text{AC}}}{E_i - \hat{H}_0 \pm \omega} = \frac{1}{E_i - \hat{H}_0 \pm \omega} \sum_{m_1, m_2} \epsilon_{m_1}^* \epsilon_{m_2} d^{m_1} d^{m_2}, \quad (\text{A.10})$$

where we used the fact that $d_m^* = d_m$.

As explained in the previous section the product of two rank-1 tensors can be written as a sum of irreducible tensors of rank $K = 0, 1, 2$. The operator can then be expressed as:

$$\frac{\hat{H}_{\text{AC}}}{E_i - \hat{H}_0 \pm \omega} = \sum_{K=0,1,2} \{\boldsymbol{\epsilon}^* \otimes \boldsymbol{\epsilon}\}_K \cdot \left\{ \frac{\mathbf{d} \otimes \mathbf{d}}{E_i - \hat{H}_0 \pm \omega} \right\}_K. \quad (\text{A.11})$$

Making use of Eq. (A.7) we can expand the two terms on the r.h.s. as:

$$\{\boldsymbol{\epsilon} \otimes \boldsymbol{\epsilon}\}_K = \sum_{m_1, m_2} \mathcal{C}_{1, m_1, 1, m_2}^{K, M} \epsilon_{m_1}^* \epsilon_{m_2}, \quad (\text{A.12})$$

$$\left\{ \frac{\mathbf{d} \otimes \mathbf{d}}{E_i - \hat{H}_0 \pm \omega} \right\}_K = \frac{1}{E_i - \hat{H}_0 \pm \omega} \sum_{m'_1, m'_2} \mathcal{C}_{1, m'_1, 1, m'_2}^{K, M} d_{m'_1} d_{m'_2}. \quad (\text{A.13})$$

Making use of Eq. (A.6) we can expand the product of irreducible tensors components of Eq. (A.11):

$$\begin{aligned} \frac{\hat{H}_{\text{AC}}}{E_i - \hat{H}_0 \pm \omega} &= \sum_{K=0,1,2} \sum_M \sum_{m_1, m_2} \sum_{m'_1, m'_2} \mathcal{C}_{1, m_1, 1, m_2}^{K, M} \left(\mathcal{C}_{1, m'_1, 1, m'_2}^{K, M} \right)^* \times \\ &\quad \times \epsilon_{m_1}^* \epsilon_{m_2} \frac{1}{E_i - \hat{H}_0 \pm \omega} d^{m'_1} d^{m'_2}. \end{aligned} \quad (\text{A.14})$$

Using the orthogonality relation of the Clebsch-Gordan coefficients:

$$\begin{aligned} \sum_K \sum_M \mathcal{C}_{1, m_1, 1, m_2}^{K, M} \left(\mathcal{C}_{1, m'_1, 1, m'_2}^{K, M} \right)^* &= \sum_K \sum_M \langle KM | |11m_1 m_2\rangle \langle 11m'_1 m'_2 | |KM \rangle \\ &= \delta_{m_1, m'_1} \delta_{m_2, m'_2}, \end{aligned} \quad (\text{A.15})$$

Eq. (A.14) reduces to Eq. (A.10) as expected. Finally, if \mathbf{d} and ϵ are two operators, as in the case treated in Chapter 2 of this thesis, the proof holds as long as $[\mathbf{d}, \epsilon] = 0$.

A.3 \vec{E} TENSOR REPRESENTATION

In order to obtain an expression for the total polarization we have to express the electric field polarization tensor $\{\epsilon^* \otimes \epsilon\}_K$ in terms of its irreducible terms. To do that is, as usual, convenient to work in a spherical basis where the polarization vector can be expanded as $\epsilon_S = \epsilon_{-1}\hat{e}_{-1} + \epsilon_0\hat{e}_0 + \epsilon_1\hat{e}_1$ with:

$$\hat{e}_q = \mathcal{T}_{\text{car} \rightarrow \text{spher}} \cdot \hat{e}_k, \quad (\text{A.16})$$

where \hat{e}_k composes the usual Cartesian basis with $k = x, y, z$.

Notice that in this basis $\epsilon_S = \epsilon$ for a linearly polarized beam along the z -direction. As the z -axis is often chosen to be the quantization one can identify the three orthogonal component of $\hat{\epsilon}_S$ respectively as the usual σ_- , π and σ_+ transitions components.

In this basis we find the scalar, vector and tensor components to be, respectively:

$$\begin{aligned} \{\epsilon^* \otimes \epsilon\}_0^{(0)} &= \frac{1}{\sqrt{3}}, \\ \{\epsilon^* \otimes \epsilon\}_m^{(1)} &= -\frac{\sin(2\theta)}{\sqrt{2}}\delta_{m,0}, \\ \{\epsilon^* \otimes \epsilon\}_m^{(2)} &= -\frac{1}{\sqrt{6}}\delta_{m,0} + \frac{1}{2}\cos(2\theta)\delta_{m,\pm 2}, \end{aligned} \quad (\text{A.17})$$

where the angle θ refers to the degree of linear $l = \cos(2\theta)$ and circular $C = \sin(2\theta)$ polarization on the plane perpendicular to the direction of propagation of light. In case the quantization axis is chosen to be along the z -direction, as is convenient to do in the absence of a magnetic field the polarization is given by $\epsilon = \mathbf{e}_x \cos \theta + i\mathbf{e}_y \sin \theta$. For a more general choice of quantization axis one has to first project the polarization vector on the plane perpendicular to the magnetic \mathbf{B} field direction defined by θ_k . The remaining component of polarization in the direction parallel to \mathbf{B} will instead give rise to a π -polarized contribution.

B I B L I O G R A P H Y

1. R. Feynman. *Simulating physics with computers*. International Journal of Theoretical Physics **21**, 467 (1982).
2. D. Deutsch & R. Jozsa. *Rapid solution of problems by quantum computation*. Proceedings of the Royal Society of London. Series A: Mathematical and Physical Sciences **439**, 553 (1992).
3. D. R. Simon. *On the Power of Quantum Computation*. SIAM Journal on Computing **26**, 1474 (1997).
4. P. W. Shor. *Polynomial-Time Algorithms for Prime Factorization and Discrete Logarithms on a Quantum Computer*. SIAM Review **41**, 303 (1999).
5. I. Buluta & F. Nori. *Quantum simulators*. Science **326**, 108 (2009).
6. S. Leontica, F. Tennie & T. Farrow. *Simulating molecules on a cloud-based 5-qubit IBM-Q universal quantum computer*. Communications Physics **4**, 112 (2021).
7. M. Zinner, F. Dahlhausen, P. Boehme, J. Ehlers, L. Bieske & L. Fehring. *Quantum computing's potential for drug discovery: Early stage industry dynamics*. Drug Discovery Today **26**, 1680 (2021).
8. W. Pouse, L. Peeters, C. L. Hsueh, U. Gennser, A. Cavanna, M. A. Kastner, A. K. Mitchell & D. Goldhaber-Gordon. *Quantum simulation of an exotic quantum critical point in a two-site charge Kondo circuit*. Nature Physics **19**, 492 (2023).
9. V. von Burg, G. H. Low, T. Häner, D. S. Steiger, M. Reiher, M. Roetteler & M. Troyer. *Quantum computing enhanced computational catalysis*. Phys. Rev. Res. **3**, 033055 (2021).
10. A. Kandala, A. Mezzacapo, K. Temme, M. Takita, M. Brink, J. M. Chow & J. M. Gambetta. *Hardware-efficient variational quantum eigensolver for small molecules and quantum magnets*. Nature **549**, 242 (2017).
11. M. Reiher, N. Wiebe, K. M. Svore, D. Wecker & M. Troyer. *Elucidating reaction mechanisms on quantum computers*. Proceedings of the National Academy of Sciences **114**, 7555 (2017).
12. W. Zhao, Y.-B. Yang, Y. Jiang, Z. Mao, W. Guo, L. Qiu, G. Wang, L. Yao, L. He, Z. Zhou, et al. *Quantum simulation for topological Euler insulators*. Communications Physics **5**, 223 (2022).

13. M. Iqbal, N. Tantivasadakarn, R. Verresen, S. L. Campbell, J. M. Dreiling, C. Figgatt, J. P. Gaebler, J. Johansen, M. Mills, S. A. Moses, *et al.* *Creation of non-abelian topological order and anyons on a trapped-ion processor*. arXiv preprint arXiv:2305.03766 (2023).
14. A. H. Karamlou, J. Braumüller, Y. Yanay, A. Di Paolo, P. M. Harrington, B. Kannan, D. Kim, M. Kjaergaard, A. Melville, S. Muschinske, *et al.* *Quantum transport and localization in 1d and 2d tight-binding lattices*. npj Quantum Information **8**, 35 (2022).
15. R. Gerritsma, G. Kirchmair, F. Zähringer, E. Solano, R. Blatt & C. Roos. *Quantum simulation of the Dirac equation*. Nature **463**, 68 (2010).
16. C. M. Wilson, G. Johansson, A. Pourkabirian, M. Simoen, J. R. Johansson, T. Duty, F. Nori & P. Delsing. *Observation of the dynamical Casimir effect in a superconducting circuit*. Nature **479**, 376 (2011).
17. M. Gärttner, J. G. Bohnet, A. Safavi-Naini, M. L. Wall, J. J. Bollinger & A. M. Rey. *Measuring out-of-time-order correlations and multiple quantum spectra in a trapped-ion quantum magnet*. Nature Physics **13**, 781 (2017).
18. K. A. Landsman, C. Figgatt, T. Schuster, N. M. Linke, B. Yoshida, N. Y. Yao & C. Monroe. *Verified quantum information scrambling*. Nature **567**, 61 (2019).
19. J. Braumüller, A. H. Karamlou, Y. Yanay, B. Kannan, D. Kim, M. Kjaergaard, A. Melville, B. M. Niedzielski, Y. Sung, A. Vepsäläinen, *et al.* *Probing quantum information propagation with out-of-time-ordered correlators*. Nature Physics **18**, 172 (2022).
20. J. R. Johansson, G. Johansson, C. M. Wilson & F. Nori. *Dynamical Casimir effect in superconducting microwave circuits*. Phys. Rev. A **82**, 052509 (2010).
21. P. Lähteenmäki, G. Paraoanu, J. Hassel & P. J. Hakonen. *Dynamical Casimir effect in a Josephson metamaterial*. Proceedings of the National Academy of Sciences **110**, 4234 (2013).
22. J. Chiaverini & W. E. Lybarger. *Laserless trapped-ion quantum simulations without spontaneous scattering using microtrap arrays*. Phys. Rev. A **77**, 022324.
23. D. Porras & J. I. Cirac. *Quantum manipulation of trapped ions in two dimensional coulomb crystals*. Phys. Rev. Lett. **96**, 250501 (2006).
24. D. Barredo, S. De Léséleuc, V. Lienhard, T. Lahaye & A. Browaeys. *An atom-by-atom assembler of defect-free arbitrary two-dimensional atomic arrays*. Science **354**, 1021 (2016).

25. M. Endres, H. Bernien, A. Keesling, H. Levine, E. R. Anschuetz, A. Krajenbrink, C. Senko, V. Vuletic, M. Greiner & M. D. Lukin. *Atom-by-atom assembly of defect-free one-dimensional cold atom arrays*. *Science* **354**, 1024 (2016).
26. H. Levine, A. Keesling, G. Semeghini, A. Omran, T. T. Wang, S. Ebadi, H. Bernien, M. Greiner, V. Vuletić, H. Pichler & M. D. Lukin. *Parallel implementation of high-fidelity multiqubit gates with neutral atoms*. *Phys. Rev. Lett.* **123**, 170503 (2019).
27. M. Morgado & S. Whitlock. *Quantum simulation and computing with Rydberg-interacting qubits*. *AVS Quantum Science* **3** (2021).
28. T. Byrnes, N. Y. Kim, K. Kusudo & Y. Yamamoto. *Quantum simulation of Fermi-Hubbard models in semiconductor quantum-dot arrays*. *Phys. Rev. B* **78**, 075320 (2008).
29. D. Bluvstein, H. Levine, G. Semeghini, T. T. Wang, S. Ebadi, M. Kalinowski, A. Keesling, N. Maskara, H. Pichler, M. Greiner, *et al.* *A quantum processor based on coherent transport of entangled atom arrays*. *Nature* **604**, 451 (2022).
30. Y. Kim, A. Eddins, S. Anand, K. X. Wei, E. Van Den Berg, S. Rosenblatt, H. Nayfeh, Y. Wu, M. Zaletel, K. Temme, *et al.* *Evidence for the utility of quantum computing before fault tolerance*. *Nature* **618**, 500 (2023).
31. J. Wurtz, A. Bylinskii, B. Braverman, J. Amato-Grill, S. H. Cantu, F. Huber, A. Lukin, F. Liu, P. Weinberg, J. Long, *et al.* *Aquila: QuEra's 256-qubit neutral-atom quantum computer*. arXiv preprint arXiv:2306.11727 (2023).
32. S. Moses, C. Baldwin, M. Allman, R. Ancona, L. Ascarrunz, C. Barnes, J. Bartolotta, B. Bjork, P. Blanchard, M. Bohn, *et al.* *A race track trapped-ion quantum processor*. arXiv preprint arXiv:2305.03828 (2023).
33. W. Paul & H. Steinwedel. *Ein neues Massenspektrometer ohne Magnetfeld*. *Zeitschrift für Naturforschung A* **8**, 448 (1953).
34. G. Stafford. *Ion trap mass spectrometry: a personal perspective*. *Journal of the American Society for Mass Spectrometry* **13**, 589 (2002).
35. J. I. Cirac & P. Zoller. *Quantum computations with cold trapped ions*. *Phys. Rev. Lett.* **74**, 4091 (1995).
36. D. P. DiVincenzo. *The physical implementation of quantum computation*. *Fortschritte der Physik: Progress of Physics* **48**, 771 (2000).
37. H. Dehmelt. *Experiments with an isolated subatomic particle at rest*. *Rev. Mod. Phys.* **62**, 525 (1990).

38. H. G. Dehmelt. *Monoion oscillator as potential ultimate laser frequency standard*. IEEE Transactions on Instrumentation and Measurement **IM-31**, 83 (1982).
39. A. Ashkin. *Acceleration and trapping of particles by radiation pressure*. Phys. Rev. Lett. **24**, 156 (1970).
40. A. M. Kaufman, B. J. Lester, C. M. Reynolds, M. L. Wall, M. Foss-Feig, K. R. A. Hazzard, A. M. Rey & C. A. Regal. *Two-particle quantum interference in tunnel-coupled optical tweezers*. Science **345**, 306 (2014).
41. D. G. Grier. *A revolution in optical manipulation*. Nature **424**, 810 (2003).
42. A. Omran, H. Levine, A. Keesling, G. Semeghini, T. T. Wang, S. Ebadi, H. Bernien, A. S. Zibrov, H. Pichler, S. Choi, *et al.* *Generation and manipulation of Schrödinger cat states in Rydberg atom arrays*. Science **365**, 570 (2019).
43. T. M. Graham, M. Kwon, B. Grinkemeyer, Z. Marra, X. Jiang, M. T. Lichtman, Y. Sun, M. Ebert & M. Saffman. *Rydberg-mediated entanglement in a two-dimensional neutral atom qubit array*. Phys. Rev. Lett. **123**, 230501 (2019).
44. A. M. Kaufman & K.-K. Ni. *Quantum science with optical tweezer arrays of ultracold atoms and molecules*. Nature Physics **17**, 1324 (2021).
45. J. D. Arias Espinoza, M. Mazzanti, K. Fouka, R. X. Schüssler, Z. Wu, P. Corboz, R. Gerritsma & A. Safavi-Naini. *Engineering spin-spin interactions with optical tweezers in trapped ions*. Phys. Rev. A **104**, 013302 (2021).
46. P. Richerme, Z.-X. Gong, A. Lee, C. Senko, J. Smith, M. Foss-Feig, S. Michalakis, A. V. Gorshkov & C. Monroe. *Non-local propagation of correlations in quantum systems with long-range interactions*. Nature **511**, 198 (2014).
47. J. Smith, A. Lee, P. Richerme, B. Neyenhuis, P. W. Hess, P. Hauke, M. Heyl, D. A. Huse & C. Monroe. *Many-body localization in a quantum simulator with programmable random disorder*. Nature Physics **12**, 907 (2016).
48. F. D. M. Haldane & S. Raghu. *Possible realization of directional optical waveguides in photonic crystals with broken time-reversal symmetry*. Phys. Rev. Lett. **100**, 013904 (2008).

49. J. Struck, C. Ölschläger, R. Le Targat, P. Soltan-Panahi, A. Eckardt, M. Lewenstein, P. Windpassinger & K. Sengstock. *Quantum simulation of frustrated classical magnetism in triangular optical lattices*. Science **333**, 996 (2011).
50. J.-y. Choi, S. Hild, J. Zeiher, P. Schauß, A. Rubio-Abadal, T. Yefsah, V. Khemani, D. A. Huse, I. Bloch & C. Gross. *Exploring the many-body localization transition in two dimensions*. Science **352**, 1547 (2016).
51. Y. H. Teoh, M. Sajjan, Z. Sun, F. Rajabi & R. Islam. *Manipulating phonons of a trapped-ion system using optical tweezers*. Phys. Rev. A **104**, 022420 (2021).
52. R. J. Spreeuw. *Off-axis dipole forces in optical tweezers by an optical analog of the Magnus effect*. Phys. Rev. Lett. **125**, 233201 (2020).
53. M. Drechsler, S. Wolf, C. T. Schmiegelow & F. Schmidt-Kaler. *Optical superresolution sensing of a trapped ion's wave packet size*. Phys. Rev. Lett. **127**, 143602 (2021).
54. F. G. Major, V. N. Gheorghe & G. Werth. *Charged particle traps: physics and techniques of charged particle field confinement* (Springer Science & Business Media, 2005).
55. D. Berkeland, J. Miller, J. C. Bergquist, W. M. Itano & D. J. Wineland. *Minimization of ion micromotion in a Paul trap*. Journal of applied physics **83**, 5025 (1998).
56. L. D. Landau & E. M. Lifshitz. *Mechanics, (volume 1 of a course of theoretical physics)* Pergamon Press (Oxford, 1969).
57. L. Bond, L. Lenstra, R. Gerritsma & A. Safavi-Naini. *Effect of micro-motion and local stress in quantum simulations with trapped ions in optical tweezers*. Phys. Rev. A **106**, 042612 (2022).
58. H. Kaufmann, S. Ulm, G. Jacob, U. Poschinger, H. Landa, A. Retzker, M. B. Plenio & F. Schmidt-Kaler. *Precise experimental investigation of eigenmodes in a planar ion crystal*. Phys. Rev. Lett. **109**, 263003 (2012).
59. H. Landa, M. Drewsen, B. Reznik & A. Retzker. *Modes of oscillation in radiofrequency Paul traps*. New Journal of Physics **14**, 093023 (2012).
60. P. Wang, C.-Y. Luan, M. Qiao, M. Um, J. Zhang, Y. Wang, X. Yuan, M. Gu, J. Zhang & K. Kim. *Single ion qubit with estimated coherence time exceeding one hour*. Nature communications **12**, 233 (2021).

61. D. T. C. Allcock, W. C. Campbell, J. Chiaverini, I. L. Chuang, E. R. Hudson, I. D. Moore, A. Ransford, C. Roman, J. M. Sage & D. J. Wineland. *omg Blueprint for trapped ion quantum computing with metastable states*. Applied Physics Letters **119**, 214002 (2021).
62. I. D. Moore, W. C. Campbell, E. R. Hudson, M. J. Boguslawski, D. J. Wineland & D. T. C. Allcock. *Photon scattering errors during stimulated Raman transitions in trapped-ion qubits*. Phys. Rev. A **107**, 032413 (2023).
63. A. Friedenauer, H. Schmitz, J. T. Glueckert, D. Porras & T. Schätz. *Simulating a quantum magnet with trapped ions*. Nature Physics **4**, 757 (2008).
64. K. Kim, M.-S. Chang, S. Korenblit, R. Islam, E. E. Edwards, J. K. Freericks, G.-D. Lin, L.-M. Duan & C. Monroe. *Quantum simulation of frustrated Ising spins with trapped ions*. Nature **465**, 590 (2010).
65. R. Blatt & C. F. Roos. *Quantum simulations with trapped ions*. Nature Physics **8**, 277 (2012).
66. I. V. Inlek, C. Crocker, M. Lichtman, K. Sosnova & C. Monroe. *Multispecies trapped-ion node for quantum networking*. Phys. Rev. Lett. **118**, 250502 (2017).
67. E. Solano, R. L. de Matos Filho & N. Zagury. *Deterministic Bell states and measurement of the motional state of two trapped ions*. Phys. Rev. A **59**, R2539 (1999).
68. A. Sørensen & K. Mølmer. *Quantum computation with ions in thermal motion*. Phys. Rev. Lett. **82**, 1971 (1999).
69. G. Milburn, S. Schneider & D. James. *Ion trap quantum computing with warm ions*. Fortschritte der Physik: Progress of Physics **48**, 801 (2000).
70. D. Porras & J. I. Cirac. *Effective quantum spin systems with trapped ions*. Phys. Rev. Lett. **92**, 207901 (2004).
71. R. Grimm, M. Weidmüller & Y. B. Ovchinnikov. *Optical dipole traps for neutral atoms*. Adv. At., Mol., Opt. Phys. **42**, 95 (2000).
72. P. Rosenbusch, S. Ghezali, V. A. Dzuba, V. V. Flambaum, K. Beloy & A. Derevianko. *ac Stark shift of the Cs microwave atomic clock transitions*. Phys. Rev. A **79**, 013404 (2009).
73. D. A. Steck. *Quantum and atom optics* (2023).

74. J. W. Britton, B. C. Sawyer, A. C. Keith, C.-C. J. Wang, J. K. Freericks, H. Uys, M. J. Biercuk & J. J. Bollinger. *Engineered two-dimensional Ising interactions in a trapped-ion quantum simulator with hundreds of spins*. Nature **484**, 489 (2012).
75. Y. Shapira, R. Shani, T. Manovitz, N. Akerman, L. Peleg, L. Gazit, R. Ozeri & A. Stern. *Theory of robust multiqubit nonadiabatic gates for trapped ions*. Phys. Rev. A **101**, 032330 (2020).
76. Y. H. Teoh, M. Drygala, R. G. Melko & R. Islam. *Machine learning design of a trapped-ion quantum spin simulator*. Quantum Science and Technology **5**, 024001 (2020).
77. L. Lenstra. *Local stress induced by optical tweezers in a trapped ion quantum simulator*. Bachelor's thesis, University of Amsterdam (2021).
78. R. Nath, M. Dalmonte, A. W. Glaetzle, P. Zoller, F. Schmidt-Kaler & R. Gerritsma. *Hexagonal plaquette spin-spin interactions and quantum magnetism in a two-dimensional ion crystal*. New Journal of Physics **17**, 065018 (2015).
79. A. Bermudez, J. Almeida, F. Schmidt-Kaler, A. Retzker & M. B. Plenio. *Frustrated quantum spin models with cold coulomb crystals*. Phys. Rev. Lett. **107**, 207209 (2011).
80. R. Blatt & D. Wineland. *Entangled states of trapped atomic ions*. Nature **453**, 1008 (2008).
81. A. H. Myerson, D. J. Szwer, S. C. Webster, D. T. C. Allcock, M. J. Curtis, G. Imreh, J. A. Sherman, D. N. Stacey, A. M. Steane & D. M. Lucas. *High-fidelity readout of trapped-ion qubits*. Phys. Rev. Lett. **100**, 200502 (2008).
82. K. R. Brown, A. C. Wilson, Y. Colombe, C. Ospelkaus, A. M. Meier, E. Knill, D. Leibfried & D. J. Wineland. *Single-qubit-gate error below 10^{-4} in a trapped ion*. Phys. Rev. A **84**, 030303 (2011).
83. C. J. Ballance, T. P. Harty, N. M. Linke, M. A. Sepiol & D. M. Lucas. *High-fidelity quantum logic gates using trapped-ion hyperfine qubits*. Phys. Rev. Lett. **117**, 060504 (2016).
84. J. P. Gaebler, T. R. Tan, Y. Lin, Y. Wan, R. Bowler, A. C. Keith, S. Glancy, K. Coakley, E. Knill, D. Leibfried & D. J. Wineland. *High-fidelity universal gate set for ${}^9\text{Be}^+$ ion qubits*. Phys. Rev. Lett. **117**, 060505 (2016).
85. K. Kim, M.-S. Chang, R. Islam, S. Korenblit, L.-M. Duan & C. Monroe. *Entanglement and tunable spin-spin couplings between trapped Ions using multiple transverse modes*. Phys. Rev. Lett. **103**, 120502 (2009).

86. T. Olsacher, L. Postler, P. Schindler, T. Monz, P. Zoller & L. M. Sieberer. *Scalable and parallel tweezer gates for quantum computing with long ion strings.* PRX Quantum **1**, 020316 (2020).
87. D. F. V. James. *Quantum dynamics of cold trapped ions with application to quantum computation.* Appl. Phys. B **66**, 181 (1998).
88. I. G. Lang & Y. A. Firsov. *Calculation of the activation probability for a jump of a small-radius polaron.* J. Exp. Theor. Phys. 3 **27**, 443 (1968).
89. D. Leibfried, B. DeMarco, V. Meyer, D. Lucas, M. Barrett, J. Britton, W. M. Itano, B. Jelenković, C. Langer, T. Rosenband, *et al.* *Experimental demonstration of a robust, high-fidelity geometric two ion-qubit phase gate.* Nature **422**, 412 (2003).
90. M. A. Nielsen. *A simple formula for the average gate fidelity of a quantum dynamical operation.* Physics Letters A **303**, 249 (2002).
91. M. Kaur, S. Singh, B. Sahoo & B. Arora. *Tune-out and magic wavelengths, and electric quadrupole transition properties of the singly charged alkaline-earth metal ions.* Atomic Data and Nuclear Data Tables **140**, 101422 (2021).
92. C. T. Schmiegelow, J. Schulz, H. Kaufmann, T. Ruster, U. G. Poschinger & F. Schmidt-Kaler. *Transfer of optical orbital angular momentum to a bound electron.* Nat. Com. **7**, 12998 (2016).
93. P. Schindler, D. Nigg, T. Monz, J. T. Barreiro, E. Martinez, S. X. Wang, S. Quint, M. F. Brandl, V. Nebendahl & C. F. Roos. *A quantum information processor with trapped ions.* New J. Phys. **15**, 123012 (2013).
94. P. J. Lee, K.-A. Brickman, L. Deslauriers, P. C. Haljan, L.-M. Duan & C. Monroe. *Phase control of trapped ion quantum gates.* Journal of Optics B: Quantum and Semiclassical Optics **7**, S371 (2005).
95. H. Häffner, S. Gulde, M. Riebe, G. Lancaster, C. Becher, J. Eschner, F. Schmidt-Kaler & R. Blatt. *Precision measurement and compensation of optical stark shifts for an ion-trap quantum processor.* Phys. Rev. Lett. **90**, 143602 (2003).
96. L. Aolita, K. Kim, J. Benhelm, C. F. Roos & H. Häffner. *High-fidelity ion-trap quantum computing with hyperfine clock states.* Phys. Rev. A **76**, 040303 (2007).
97. *NIST Atomic Spectra Database.* <http://physics.nist.gov/PhysRefData/ASD/>

98. J. Vogel, W. Li, A. Mokhberi, I. Lesanovsky & F. Schmidt-Kaler. *Shuttling of Rydberg ions for fast entangling operations*. Phys. Rev. Lett. **123**, 153603 (2019).
99. M. A. Norcia, A. W. Young & A. M. Kaufman. *Microscopic control and detection of ultracold strontium in optical-tweezer arrays*. Phys. Rev. X **8**, 041054 (2018).
100. A. Browaeys & T. Lahaye. *Many-body physics with individually controlled Rydberg atoms*. Nature Physics **16**, 132 (2020).
101. M. Mazzanti, R. X. Schüssler, J. D. Arias Espinoza, Z. Wu, R. Gerritsma & A. Safavi-Naini. *Trapped ion quantum computing using optical tweezers and electric fields*. Phys. Rev. Lett. **127**, 260502 (2021).
102. J. I. Cirac & P. Zoller. *A scalable quantum computer with ions in an array of microtraps*. Nature **404**, 579 (2000).
103. M. Šašura & A. M. Steane. *Fast quantum logic by selective displacement of hot trapped ions*. Phys. Rev. A **67**, 062318 (2003).
104. T. Calarco, J. I. Cirac & P. Zoller. *Entangling ions in arrays of microscopic traps*. Phys. Rev. A **63**, 062304 (2001).
105. K.-P. Wang, J. Zhuang, X.-D. He, R.-J. Guo, C. Sheng, P. Xu, M. Liu, J. Wang & M.-S. Zhan. *High-fidelity manipulation of the quantized motion of a single atom via Stern-Gerlach splitting*. Chinese Phys. Lett. **37**, 044209 (2020).
106. R. J. C. Spreeuw. *Spiraling light: from donut modes to a Magnus effect analogy*. Nanophotonics **11**, 633 (2022).
107. K. Mølmer & A. Sørensen. *Multiparticle entanglement of hot trapped ions*. Phys. Rev. Lett. **82**, 1835 (1999).
108. S. Olmschenk, K. C. Younge, D. L. Moehring, D. N. Matsukevich, P. Maunz & C. Monroe. *Manipulation and detection of a trapped Yb^+ hyperfine qubit*. Phys. Rev. A **76**, 052314 (2007).
109. F. Stopp, M. Verde, M. Katz, M. Drechsler, C. T. Schmiegelow & F. Schmidt-Kaler. *Coherent transfer of transverse optical momentum to the motion of a single trapped ion*. Phys. Rev. Lett. **129**, 263603 (2022).
110. M. D. Hughes, B. Lekitsch, J. A. Broersma & W. K. Hensinger. *Microfabricated ion traps*. Contemporary Physics **52**, 505 (2011).
111. J. K. Joger. *Cold $Li-Yb^+$ mixtures in a hybrid trap setup*. Ph. D. Universiteit van Amsterdam, 2018.

112. A. S. Bell, P. Gill, H. A. Klein, A. P. Levick, C. Tamm & D. Schnier. *Laser cooling of trapped ytterbium ions using a four-level optical-excitation scheme*. Phys. Rev. A **44**, R20 (1991).
113. R. Berends, E. Pinnington, B. Guo & Q. Ji. *Beam-laser lifetime measurements for four resonance levels of Yb II*. Journal of Physics B: Atomic, Molecular and Optical Physics **26**, L701 (1993).
114. P. Taylor, M. Roberts, S. V. Gateva-Kostova, R. B. M. Clarke, G. P. Barwood, W. R. C. Rowley & P. Gill. *Investigation of the $^2S_{1/2}-^2D_{5/2}$ clock transition in a single ytterbium ion*. Phys. Rev. A **56**, 2699 (1997).
115. E. H. Pinnington, G. Rieger & J. A. Kernahan. *Beam-laser measurements of the lifetimes of the 6p levels in Yb II*. Phys. Rev. A **56**, 2421 (1997).
116. N. Yu & L. Maleki. *Lifetime measurements of the $4f^{14}5d$ metastable states in single ytterbium ions*. Phys. Rev. A **61**, 022507 (2000).
117. S. Olmschenk, D. Hayes, D. N. Matsukevich, P. Maunz, D. L. Moehring, K. C. Younge & C. Monroe. *Measurement of the lifetime of the 6p $^2P_{1/2}^o$ level of Yb^+* . Phys. Rev. A **80**, 022502 (2009).
118. T. Feldker, H. Fürst, N. V. Ewald, J. Joger & R. Gerritsma. *Spectroscopy of the $^2S_{1/2} \rightarrow ^2P_{3/2}$ transition in Yb II: Isotope shifts, hyperfine splitting, and branching ratios*. Phys. Rev. A **97**, 032511 (2018).
119. R. Lange, A. A. Peshkov, N. Huntemann, C. Tamm, A. Surzhykov & E. Peik. *Lifetime of the $^2F_{7/2}$ level in Yb^+ for spontaneous emission of electric octupole radiation*. Phys. Rev. Lett. **127**, 213001 (2021).
120. S. Botsi. *Design and construction of two external-cavity diode lasers for Rydberg excitation of Rb atoms*. Bachelor's thesis, University of Amsterdam (2014).
121. Z. Wu. *Towards quantum simulation with two-dimensional trapped ion crystals*. Master Thesis, University of Amsterdam (2021).
122. S. Ejtemaei & P. C. Haljan. *3D Sisyphus cooling of trapped ions*. Phys. Rev. Lett. **119**, 043001 (2017).
123. M. Qiao, Y. Wang, Z. Cai, B. Du, P. Wang, C. Luan, W. Chen, H.-R. Noh & K. Kim. *Double-electromagnetically-induced-transparency ground-state cooling of stationary two-dimensional ion crystals*. Phys. Rev. Lett. **126**, 023604 (2021).
124. Z. E. D. Ackerman. *Towards measuring the sound wave spectrum of a trapped-ion crystal manipulated by optical tweezers*. Master Thesis, University of Amsterdam (2022).

125. T. Preuschoff, M. Schlosser & G. Birk. *Digital laser frequency and intensity stabilization based on the STEMlab platform (originally Red Pitaya)*. Review of Scientific Instruments **91**, 083001 (2020).
126. R. W. Drever, J. L. Hall, F. V. Kowalski, J. Hough, G. Ford, A. Munley & H. Ward. *Laser phase and frequency stabilization using an optical resonator*. Applied Physics B **31**, 97 (1983).
127. M. A. Luda, M. Drechsler, C. T. Schmiegelow & J. Codnia. *Compact embedded device for lock-in measurements and experiment active control*. Review of Scientific Instruments **90**, 023106 (2019).
128. H. A. Fürst. *Trapped ions in a bath of ultracold atoms*. Ph. D. Universiteit van Amsterdam, 2019.
129. P. Langevin. *A fundamental formula of kinetic theory*. Ann Chim Phys **5**, 245 (1905).
130. J. a. Mitroy, M. S. Safronova & C. W. Clark. *Theory and applications of atomic and ionic polarizabilities*. Journal of Physics B: Atomic, Molecular and Optical Physics **43**, 202001 (2010).
131. D. Spelsberg & W. Meyer. *Static dipole polarizabilities of N_2 , O_2 , F_2 , and H_2O* . The Journal of chemical physics **101**, 1282 (1994).
132. R. W. Gerchberg. *A practical algorithm for the determination of phase from image and diffraction plane pictures*. Optik **35**, 237 (1972).
133. R. Di Leonardo, F. Ianni & G. Ruocco. *Computer generation of optimal holograms for optical trap arrays*. Optics Express **15**, 1913 (2007).
134. M. Pasinski & B. DeMarco. *A high-accuracy algorithm for designing arbitrary holographic atom traps*. Optics express **16**, 2176 (2008).
135. K. Fouka. *Controlling spin-spin interactions between trapped ions using optical tweezers*. Master Thesis, University of Amsterdam (2021).
136. T. Čižmár, M. Mazilu & K. Dholakia. *In situ wavefront correction and its application to micromanipulation*. Nature Photonics **4**, 388 (2010).
137. H. Hirzler, T. Feldker, H. Fürst, N. V. Ewald, E. Trimby, R. S. Lous, J. D. Arias Espinoza, M. Mazzanti, J. Joger & R. Gerritsma. *Experimental setup for studying an ultracold mixture of trapped Yb^+ - ${}^{6}Li$* . Phys. Rev. A **102**, 033109 (2020).
138. D. Armstrong, A. Stilgoe, T. Nieminen & H. Rubinsztein-Dunlop. *Improved two-photon photopolymerisation and optical trapping with aberration-corrected structured light*. Frontiers in Nanotechnology **4**, 998656 (2022).
139. T. M. Hoang, Y.-Y. Jau, R. Overstreet & P. D. D. Schwindt. *YbH^+ formation in an ytterbium ion trap*. Phys. Rev. A **101**, 022705 (2020).

140. J. B. Wübbena, S. Amairi, O. Mandel & P. O. Schmidt. *Sympathetic cooling of mixed-species two-ion crystals for precision spectroscopy*. Phys. Rev. A **85**, 043412 (2012).